Integration of Ferroelectric Thin Films on Silicon for Electro-Optic Devices

Integratie van ferro-elektrische dunne lagen op silicium voor toepassing in elektro-optische componenten

John Puthenparampil George

Promotoren: prof. dr. ir. J. Beeckman, prof. dr. ir. D. Van Thourhout
Proefschrift ingediend tot het behalen van de graad van
Doctor in de Ingenieurswetenschappen: Elektrotechniek

Vakgroep Elektronica en Informatiesystemen
Voorzitter: prof. dr. ir. R. Van de Walle

Vakgroep Informatietechnologie
Voorzitter: prof. dr. ir. D. De Zutter

Faculteit Ingenieurswetenschappen en Architectuur
Academiejaar 2015 - 2016

ISBN 978-90-8578-894-2
NUR 959
Wettelijk depot: D/2016/10.500/26

Promoters:

Prof. Dr. Jeroen Beeckman	Ghent University, ELIS
Prof. Dr. Dries Van Thourhout	Ghent University, INTEC

Other Members of the Examination Committee:

Prof. Dr. Rik Van de Walle (Chairman)	Ghent University, ELIS
Prof. Dr. Kristiaan Neyts	Ghent University, ELIS
Prof. Dr. Wim Bogaerts	Ghent University, INTEC
Prof. Dr. Dirk Poelman	Ghent University, Department of Solid-state Physics
Dr. Sebastien Lardenois	Caliopa, Belgium
Prof. Dr. Jean-françois Blach	Université d`Artois, France

Universiteit Gent
Faculteit Ingenieurswetenschappen en Architectuur
Vakgroep Elektronica en Informatiesystemen
Vakgroep Informatietechnologie
Sint-Pietersnieuwstraat 41
B-9000 Gent
België
T: (+32) (0)9 264 6665
F: (+32) (0)9 264 3594

Acknowledgements

I would like to express my deep sense of gratitude and sincere thanks to my promoters Prof. Jeroen Beeckman and Prof. Dries Van Thourhout for giving me the opportunity to work under their guidance. I sincerely acknowledge their support during all sorts of hurdles in the execution of my thesis work as well as the personal difficulties.

I would like to thank the jury members, Prof. Dirk Poelman, Dr. Sebastien Lardenois, Prof. Wim Bogaerts, Prof. Jean-françois Blach, and Prof. Kristiaan Neyts for their useful thoughts and comments, I believe it really helped me to improve my thesis.

Being far away from home for such a long period is never easy unless you have many good people around to guide you through all the do's and don'ts. I was indeed blessed with so many nice people from both my research groups, ELIS and INTEC. Thanks to Prof. Kristiaan Neyts and Prof. Patrick De Visschere, who have been father figures to me and I find very inspiring people. Many thanks to prof. Mark Burgelman and Prof. Alex De Vos, for all their support. I wish to thank to my officemates, whom I shared the room with, Lieven, Inge, Michiel, Mohammad and Wouter, for the fun filled 4 years. Special thanks to Wouter, who helped me to kickstart my PhD with all the fancy materials and I really enjoyed spending time with Jeff, Julie and John. Many thanks to Samira and Aimi, for the chocolates, dinner, movies, games and all funny things, we did. I would like to thank Filip Bunis, Filip Strubbe, Toon (thanks for the clean-room help), Stijn (thanks for the COMSOL help), Masoumeh, Oksana, and Casper for all the fruitful conversations. Thanks to all the liquid crystal buddies, Oliver (thanks for all the help with the software's and for the nice food), Tom, Yie and Glenn.

My sincere thanks to all the professors from INTEC, Prof. Roel Baets, Prof. Gunther Roelkens, Prof. Geert Morthier, Prof. Nicolas Le Thomas, Prof. Bart Kuyken and Prof. Peter Bienstman. I wish to thank Pijush, Alfonso, Shibnath, Sarvagya and Shankar, for helping me out with measurements at

various stages of my PhD. I would like to thank Leila for her help with the design of the mask. Thanks to all the PhD's, post doc's and technical staff (an infinite list) from the photonics research group, you all were a great support.

My gratitude to the people from Lumi Lab. My special thanks Prof. Philippe Smet, for guiding me through the initial struggles with the materials and helped me a lot with all the material characterizations. Thanks to Olivier Janssens, Vitally Bliznuk and Jonas Botterman for the XRD and TEM measurements. Thanks to Geert for helping me with the ellipsometer measurements and for your useful insights to improve processing.

Thanks to my friends and colleagues from INTEC and CMST, whom I worked with in the cleanroom. I would like to thank Liesbet for all the SEM measurements and TEM sample preparation. My sincere thanks to Steven for teaching and helping me with the processing. Special thanks to Dieter Cuypers for his help with the evaporation system and all the assistance to make new connections to the system. I would also like to thank Sanjeev, Sandeep, Pankaj, David, Rik, Jelle, Tom, Philip, Filip, Nuria, kamal and Ahmed for all their help and support.

Thanks to all my friends in India, Praveen, Shijo, Aldo, Alma, Sindhu, Pramod, Pradeep, Deepa and Rajan. I would like to thank Thomas specifically for his great friendship, you have been a wonderful friend. I would like to thanks all my friends from KU Leuven, Deepak, Joice, Sree, Shambu for all the fun times. I would like to thank my family members and cousins (Deepthi, Pradeep, Deepa, Tijo, Melvin, Merin, Akhil, Geethu, Jobin, Diana and Jannet), you were my motivation.

I wish to thank my parents and my brother, for the support and love they gave me over the years. Even though being away for more than 12 years, you have been my strength.

Finally, I would like to thank my better half Joice Maria, for being by my side and coping with all my tensions. You are a constant support on all my tough times and my sunshine to move forward.

Gent, May 11, 2016

John P George

Table of contents

Acknowledgements iii

Table of contents v

Summary xi

Samenvatting xv

List of figures xix

List of tables xxix

List of Publications xxxi

List of symbols xxxiv

List of abbreviations xxxvii

Chapter 1 3

1.1 Introduction 3

1.2 Context and objective of this research 5

1.3 Properties of ferroelectric thin films 6

1.4 Ferro-electric thin films -- fabrication methods and challenges 10

1.5 Si based modulator technology 13

1.6 Photonic devices- based on ferroelectric thin films 15

1.6.1 Piezo-electrically tuned optical waveguides 16

1.6.2 Electro-optic tuning optical waveguides 20

1.7 Thesis structure 24
1.8 References 26
Chapter 2 33
2.1 Deposition of the PZT thin films - Current deposition methods and challenges 34
2.2 Chemical solution deposition 35
2.3 Preparation and deposition of intermediate layers 36
2.4 PZT and PLZT preparation 38
2.5 Deposition procedure – ferroelectric thin films 40
2.6 Structural characterization 42
2.6.1 Texture analysis- X-ray pole figure measurement 42
2.6.2 X-ray diffraction measurements-PZT thin films 44
2.6.2.1 PZT deposition on SiO_2, ITO and $PbTiO_3$ Intermediate layers 44
2.6.2.2 PZT deposition on lanthanide (Ln) based intermediate layers 47
2.6.2.3 Effect of buffer layer treatments 48
2.6.2.4 Effect of intermediate layer thickness 50
2.6.2.5 Deposition on non-planar substrates 52
2.6.2.6 Influence of annealing temperature 53
2.6.2.7 Deposition on different substrates 55
2.6.2.8 Deposition of PLZT thin films 56
2.6.3 SEM analysis of PZT 57
2.6.4 TEM analysis of PZT 59
2.6.5 AFM analysis of PZT 61
2.7 $BaTiO_3$ and $BaZrTiO_3$ thin film preparation and deposition 61
2.8 X-ray diffraction measurements-$BaTiO_3$ thin films 63
2.9 SEM analysis 68

2.10 AFM analysis 702.11
XRD- BZT thin films 70
2.12 $LiNbO_3$ thin films 72
2.13 Overview of ferroelectric thin film deposition 73
2.14 Conclusion 74
2.15 References 75
Chapter 3 81
3.1 Introduction 81
3.2 Sample Preparation 82
3.3 Electrical characterization 83
3.3.1 Dielectric constant and dielectric loss measurements- PZT thin films 83
3.3.2 P-E hysteresis measurements-PZT thin films 87
3.3.3 I-V measurements -PZT thin films 91
3.4 Electrical measurements - BTO and BZT thin films 92
3.5 Electro-optic characterization of PZT thin films 94
3.6 Conclusions 107
3.7 References 108
Chapter 4 111
4.1 Background on current Si_3N_4 based waveguide active tuning devices 112
4.2 Modulator configurations 113
4.2.1 Embedded electrode configuration 114
4.2.2 Co-planar electrode configuration 116
4.3 Simulation of PZT/Si_3N_4 electro optic modulators 118
4.3.1 Calculation of the Confinement factor 121
4.3.2 Electrode Absorption Loss 123
4.3.3 Transition Mode Loss 126

4.3.4 Bend waveguide loss 129
4.3.5 Electro-optic simulations and evaluation of the voltage-length ($V_\pi L_\pi$) Product 130
4.4 Conclusions 134
4.5 References 135
5.1 Fabrication of Si_3N_4/PZT electro-optic devices 138
5.1.1 Need for planarization 138
5.1.2 Sample cleaning 139
5.1.3 Ferroelectric thin film preparation 139
5.1.4 Lithography 141
5.1.5 Etching of PZT thin film 142
5.1.6 Metal contact and oxide etching 144
5.2 Characterization of Si_3N_4/PZT electro-optic devices 145
5.2.1 Electro-optic characterization 147
5.3 Conclusion 152
5.4 References 153
Chapter 6 155
6.1 Conclusions 155
6.2 Outlook and future work 157
6.2.1 Improvement of the thin film processing 158
6.2.2 Improvement of modulators using other materials and/or electrode configurations 158
6.2.3 Modulators using TM polarized light 159
6.2.4 Modulators on Si platform 159
6.2.5 Waveguide tuning based on the piezoelectric effect 159
6.2.6 Optical nonlinearities 160
Appendix A 161
Simulation of Si/PZT based electro-optic devices 161

A1: Embedded electrode configuration 161
A2: Co-planar electrode configuration 163

Summary

The deposition of high quality ferroelectric thin films has been studied extensively over the past few decades, because of their excellent piezo-electric, pyro-electric, ferroelectric and/or electro-optic (EO) properties. The presence of functional properties in many ferroelectric materials has motivated the heterogeneous integration of crystalline thin films directly on crystalline (Si, MgO, Nd:$SrTiO_3$) and amorphous substrates (Si_3N_4, SiO_2) for the realization of a variety of novel devices. Among the known ferroelectric thin film oxides, lead zirconate titanate (PZT) and barium titanate ($BaTiO_3$) exhibit a large dielectric constant, piezo-electric coefficient, and electro-optic coefficient. These excellent properties already resulted in applications of the materials in ferroelectric thin film capacitors, piezo-electric actuators, and electro-optic modulators. Recent advances in the thin film technology show nano-grained PZT films with excellent ferroelectric properties. Novel devices with PZT nano-fibers have been demonstrated for mechanical energy harvesting.

Although the ferroelectric thin films are explored mostly for electronic applications, the ever increasing demand for higher bandwidth meanwhile putting constraints on power consumption, has resulted in an increasing interest towards the use of the films in the optical domain for e.g. telecommunication. To realize optical data transmission e.g. for chip-to-chip interconnects, integrated optical devices which are compatible with the electrical systems are indispensable. The well-established ferroelectric oxide based technologies propelled the development of high-speed electro-optic devices on different material platforms such as $LiNbO_3$. However, the existing photonics technologies (Si or Si_3N_4) do not yet exploit the strong linear electro-optic properties of PZT thin films. The current state-of-the-art

high-speed optical devices are based on $LiNbO_3$ single crystals or integrated into the InP photonics platform. Replacing them with ferroelectric thin film oxides such as PZT, along with the compact silicon photonic platform, could be an alternative to realize smaller, functional and power efficient devices without the need for large amounts of rare elements such as In or Nb.

A variety of methods can be used to deposit ferroelectric thin films: chemical solution deposition (CSD), RF magnetron sputtering, metal organic chemical vapour deposition (MOCVD) and pulsed laser deposition (PLD). However, the direct deposition of PZT on silicon still remains a challenge. It is reported that there is inter-diffusion between the Si substrate and the PZT thin film at a high annealing temperature, which makes it hard to form the perovskite PZT phase. Different methods have been proposed and demonstrated to use either a seed or a barrier layer to promote the thin film growth. The nucleation of the PZT thin films strongly depends on the underlying substrate and the interface properties.

In our work, a novel type of intermediate layer is demonstrated that allows depositing highly textured ferroelectric thin films on different platforms. The ultra-thin lanthanide-based layer with a thickness ranging from 5 to 15 nm is used as intermediate layer for the ferroelectric thin film growth. All the intermediate layers as well as ferroelectric thin films reported in this work are deposited following a chemical solution deposition procedure. The state-of-the-art micro and nano scale EO devices developed on different waveguide platforms are based on complex and costly layer bonding approaches and with more sophisticated epitaxially grown ferroelectric oxides. Our novel deposition method on the other hand offers a low cost and simple method to produce good quality, strong electro-optic PZT thin films on crystalline (Si) and amorphous (glass, glass+ITO, Al_2O_3, SiO_2 and Si_3N_4) substrates for a variety of integrated photonic and electronic applications. A number of well-known ferroelectric thin films such as PZT, PLZT, BTO have been tested in this work. A variety of structural characterization techniques such as XRD, X-ray pole figures, SEM, TEM and AFM are used to confirm the quality and properties of these thin films. Regardless the growth conditions, the films have a strong columnar structure with a high degree of orientation (> 99.8%) on all the intermediate layers. The SEM and AFM measurements confirm smooth, well packed, crack free thin films. The TEM measurements show the presence of an ultra-thin crystalline intermediate layer with good lattice match with the subsequently deposited

ferroelectric thin films. The EDX measurement proves the lanthanide based intermediate layer as an efficient barrier to prevent lead diffusion.

The thin films are electrical characterized by C-V, C-F, and I-V measurements to analyse the quality of the deposited films. The films exhibit very good dielectric properties, low dielectric loss and good dielectric breakdown strength. The dielectric constant measurement of the films shows a large dielectric constant of ~ 600 for PZT thin films, 260 for BTO and 350 for BZT thin films. The P-E hysteresis measurement shows low coercive field and strong remnant polarization. The electro-optic properties of the bulk PZT thin films have been measured with an ellipsometric technique. An electric field is applied along the (100) crystallographic direction and the variations observed in the ellipsometry angles are used to extract the EO coefficients. The PZT films annealed at 630ºC and 560ºC on La, Pr and Nd based buffer layers exhibit a high linear effective pockels coefficient of 240 pm/V, 215 pm/V, 200 pm/V and 115 pm/V, 96 pm/V, 89 pm/V, respectively, at a wavelength of 630 nm. These results are comparable to values measured on single crystalline PZT thin films, showing that our PZT film is an ideal candidate for silicon nano-photonic EO modulators.

In the second part of the work, we propose a novel design to develop compact electro-optic modulators on the Si_3N_4 platform with ferroelectric thin films. Here, a thin PZT layer with a thickness of 100 to 150 nm is used as a cladding layer over the Si_3N_4 waveguide. Since the refractive index of PZT is larger than the refractive index of Si_3N_4, the PZT layer needs to be sufficiently thin in order to avoid light leakage. The thickness of the PZT layer is optimized to improve the light confinement in the PZT layer while minimizing the transition mode loss and bend loss. The high field concentration within the PZT cladding leads to good overlap between the modulating electric fields and the propagating light. Different electrode configurations are proposed, which show the possibilities of using our PZT films on different waveguide materials. Since the light absorption from the contact electrodes are one of the main loss mechanisms for waveguides with co-planar electrodes, the electrode spacing is optimized to reduce the mode absorption loss and to improve the $V_\pi L_\pi$ product. Following our simulation results, the length of the modulator can be reduced by increasing the thickness of the PZT layer and by reducing the thickness of the waveguide. With our design, modulators with $V_\pi L_\pi$ less than 1 V.cm are possible for devices with Si_3N_4 waveguides with a width of less than 1 μm, a Si_3N_4

thickness of 300 nm, a PZT thickness of 150 nm and an electrode spacing of 6 μm.

We used Si_3N_4 waveguides planarized with SiO_2 to a thickness of 50 to 100 nm over the top of the waveguide, to allow the uniform deposition of the ferroelectric thin film. The electrodes are designed and fabricated in a co-planar fashion with UV lithography, lift-off and e-gun evaporation methods. An etching process based on SF_6 gas is developed to efficiently pattern the PZT films. The fabricated devices are DC characterized to understand the electro-optic properties. The $V_\pi L_\pi$ product for these devices is measured as 1.68V.cm, 2.16V.cm and 2.94 V.cm, for waveguides with a width of 540 nm, 1540 nm and 1940 nm respectively. The results are to the best of our knowledge the best ones reported on waveguides based on the Si_3N_4 platform, with an order of magnitude improvement in the $V_\pi L_\pi$ product compared to previously reported devices based on piezoelectric effects. The high speed characterization of the films requires further optimization of the fabrication process and electrode design.

Samenvatting

De depositie van ferro-elektrische dunne lagen met hoge kwaliteit is een onderwerp dat intensief bestudeerd is gedurende de laatste decades. De reden hiervoor is dat deze materialen uitstekende piëzo-elektrische, pyro-elektrische, ferro-elektrisch en elektro-optische (EO) eigenschappen hebben. De mogelijkheid om verschillende van hun fysische effecten te gebruiken heeft mensen gemotiveerd om de heterogene integratie van deze kristallijne dunne lagen te onderzoeken op kristallijne (Si, MgO, Nd:$SrTiO_3$) en amorfe substraten (Si_3N_4, SiO_2) voor het gebruik in een breed scala aan nieuwe componenten. Van de gekende ferro-elektrische dunne oxidelagen hebben lood zirconaat titanaat (PZT) en barium titanaat (BTO) de grootste diëlektrische constante, piëzo-elektrische coëfficiënt en elektro-optische coëfficiënt. Hun uitstekende eigenschappen hebben al geleid tot verschillende toepassingen van deze materialen in ferro-elektrische condensatoren, piëzo-elektrische actuatoren en EO modulatoren. Recente ontwikkelingen in de dunne-laag technologie hebben geleid tot nano-korrel PZT-lagen met uitstekende ferro-elektrische eigenschappen. Nieuwe componenten met PZT-nanovezels hebben o.a. hun potentie bewezen voor mechanische energie-opwekking.

Hoewel de ferro-elektrische dunne lagen hoofdzakelijk onderzocht worden voor elektronische toepassingen, heeft de immer stijgende vraag naar hogere bandbreedte (met alsmaar lager energieverbruik) geresulteerd in een sterke interesse naar het gebruik ervan in optische toepassingen voor o.a. telecommunicatie. Data transmissie in chip-naar-chip interconnecties bijvoorbeeld heeft nood aan geïntegreerde optische componenten die compatibel zijn met de elektrische componenten. De goed ontwikkelde

technologie gebaseerd op ferro-elektrische oxides heeft geleid tot elektri-optische componenten met hoge snelheid zoals de elektro-optische modulatoren gebaseerd op $LiNbO_3$. Enkele belangrijke bestaande fotonische platformen (Si of Si_3N_4) hebben nog niet het volle potentieel van de sterke lineaire EO eigenschappen van bvb. dunne PZT-lagen kunnen benutten. De huidige state-of-the-art hoge-snelheidsmodulatoren zijn gebaseerd op monokristallijne $LiNbO_3$-substraten of zijn geïntegreerd in het InP fotonische platform. Het vervangen door ferro-elektrische oxide-gebaseerde dunne lagen (zoals PZT) op een compact platform zoals het silicium fotonische platform kan een interessant alternatief zijn om kleine en energie-efficiënte componenten te realiseren die kunnen werken aan hoge snelheden. Bovendien vervalt de nood aan grote hoeveelheden van zeldzame materialen zoals In of Nb.

Er bestaan verschillende methoden om ferro-elektrische dunne lagen te deponeren: sol-gel depositie (*Chemical Solution Deposition*, CSD), RF magnetron sputteren, metaal-organische chemische gasfase depositie (*metal organic chemical vapor deposition* , MOCVD) en gepulste laser depositie (*Pulsed Laser Deposition*, PLD). Ondanks de geavanceerde depositiemethoden blijft de directe depositie van PZT op silicium een grote uitdaging. De interdiffusie van elementen tussen het silicium substraat en de PZT dunne film bij hoge uitgloeitemperaturen voorkomt de vorming van de gewenste perovskiet PZT fase. Verschillende methoden werden reeds voorgesteld en gedemonstreerd op basis van een nucleatie- of bufferlaag om de dunne-laag-groei te bevorderen. De nucleatie van de dunne PZTlaag hangt sterk af van het onderliggende substraat en van de interface-eigenschappen.

In dit werk wordt een nieuw type intermediaire laag gedemonstreerd die toelaat om sterk georiënteerde ferro-elektrische dunne lagen te deponeren op verschillende materiaalplatformen. De ultradunne lanthanide gebaseerde laag met een dikte van 5 tot 15 nm wordt gebruikt als intermediaire laag voor de dunne-laag groei. Zowel de intermediaire lagen als de PZT-laag zelf worden gedeponeerd via CSD. De state-of-the-art micro- en nanoschaal elektro-optische componenten die werden ontwikkeld op verschillende golfgeleiderplatformen zijn typisch gebaseerd op complexe en dure laag-bind-technieken of zeer geavanceerde epitaxiaal gegroeide ferro-elektrische oxides. Onze nieuwe depositiemethode heeft het voordeel dat het een simpele en goedkope methode is die lagen van goede kwaliteit oplevert met sterke elektro-optische eigenschappen op zowel kristallijne (Si) als op

amorfe substraten (glas, glas+ITO, Al_2O_3, SiO_2 en Si_3N_4) voor een verscheidenheid aan geïntegreerde fotonische en elektronische toepassingen. Heel wat gekende ferro-elektrische materialen werden in dit werk getest op hun dunne-laag depositie zoals PZT, PLZT en BTO. Een verscheidenheid aan structurele karakterisatietechnieken werd gebruikt om de kwaliteit en de eigenschappen van deze lagen te onderzoeken, zoals XRD, X-straal poolfiguren, SEM, TEM en AFM. Onafhankelijk van de groeicondities en de intermediaire laag hebben de dunne lagen een sterke columnaire structuur met een grote orde qua oriëntatie (> 99.8%). De SEM- en AFM-metingen bevestigen dat de dunne lagen glad, dicht gepakt en zonder barsten zijn gegroeid. De TEM-metingen tonen de aanwezigheid van de ultradunne kristallijne intermediaire laag aan die een goede match vertoont van de roosterconstante met de ferro-elektrische dunne laag. De EDX-metingen tonen aan dat de lanthanide gebaseerde intermediaire laag een efficiënte buffer is die o.a. de diffusie van lood tegenhoudt.

De dunne lagen werden vervolgens elektrisch gekarakteriseerd met C-V, C-F en I-V metingen om de kwaliteit van de lagen aan te tonen. De lagen vertonen zeer goede diëlektrische constanten, lage diëlektrische verliezen en een hoge doorslag elektrische veldsterkte. De diëlektrische constanten van onze lagen zijn ongeveer 600 voor PZT, 260 voor BTO en 350 voor BZT. De P-E hysteresemeting resulteert in een lage waarde van het coërcitief veld en een sterke remanente polarisatie. De elektro-optische eigenschappen van de vlakke PZT dunne lagen werden gemeten met een ellipsometrische techniek. Een elektrisch veld werd aangelegd langs de (100) kristallografische richting en de variaties in de ellipsometrische hoeken werden gebruikt om de elektro-optische coëfficiënten te extraheren. De PZT-lagen die uitgegloeid werden op 360°C en 560°C op La-, Pr- en Nd-gebaseerde bufferlagen vertonen een hoge lineaire effectieve pockels coëfficiënt van respectievelijk 240 pm/V, 215 pm/V, 200 pm/V en 115 pm/V, 96 pm/V, 89 pm/V voor een golflengte van 630 nm. Deze waarden zijn vergelijkbaar met de waarden van monokristallijne PZT-lagen. Dit toont aan dat onze PZT-film een ideale kandidaat is voor silicium nanofotonische elektro-optische modulatoren.

In het tweede deel van dit werk wordt een nieuw ontwerp voorgesteld van een compacte elektro-optische modulator op het Si_3N_4 golfgeleiderplatform met behulp van de ontwikkelde PZT dunne lagen. Een PZT-laag met een dikte van 100 tot 150 nm wordt gebruikt als deklaag voor een Si_3N_4 golfgeleider. Aangezien de brekingsindex van PZT groter is dan die van

Si_3N_4 moet de PZT-laag voldoende dun zijn om het lekken van licht in de PZT laag te vermijden. De dikte van de PZT laag is geoptimaliseerd om de hoeveelheid licht in de PZT-laag te maximaliseren met de restrictie dat de mode-transitieverliezen en de bochtenverliezen aanvaardbaar moeten zijn. De hoeveelheid licht in de PZT-deklaag zorgt ervoor dat er een goede overlap is tussen de aangelegde elektrische velden (via een spanning over de elektrodes) en het propagerende licht. Verschillende elektrodeconfiguraties werden voorgesteld die de mogelijkheden illustreren van PZT op verschillende golfgeleidermaterialen. Aangezien het lichtverlies hoofdzakelijk komt van de absorptie aan de co-planaire elektrodes is deze afstand geoptimaliseerd zodat de verliezen beperkt zijn maar het $V_\pi L_\pi$ product toch voldoende laag is. Op basis van de simulaties kunnen we besluiten dat de lengte van de modulator kan verminderd worden door de dikte van de PZT-laag te vergroten en door de dikte van de golfgeleider te verkleinen. Dankzij het geoptimaliseerde ontwerp behaalden onze testcomponenten een $V_\pi L_\pi$ van minder dan 1 V.cm. Deze waarde geldt voor Si_3N_4-golfgeleiders van minder dan 1 µm breedte, een dikte van 300 nm, een PZT-dikte van 150 nm en een afstand tussen de elektrodes van 6 µm.

De gebruikte Si_3N_4-golfgeleiders zijn geplanariseerd met SiO_2 met een dikte van 50 tot 100 nm bovenop de golfgeleider, om de depositie van een uniforme ferro-elektrische film mogelijk te maken. De co-planaire elektrodes zijn gemaakt met een combinatie van UV-lithografie, lift-off en e-gun opdamping. Een etsproces gebaseerd op SF_6-gas is ontwikkeld om efficiënt patronen te vormen in PZT lagen. De gefabriceerde componenten werden gekarakteriseerd met statisch aangelegde spanningen om de elektro-optische eigenschappen te weten te komen. Het $V_\pi L_\pi$ -product dat gemeten werd voor deze componenten is 1.68V.cm, 2.16V.cm en 2.94 V.cm voor golfgeleiders met 540 nm, 1540 nm en 1940 nm respectievelijk. Deze waarden zijn voor zover ik weet de beste die gerapporteerd werden op golfgeleiders gebaseerd op het Si_3N_4-platform. De waarden zijn een (grootte)orde beter dan componenten die werken op basis van piëzo-elektrische effecten.

De karakterisatie van de lagen bij hoge snelheid vereist verdere optimalisatie van zowel het elektrodeontwerp als het fabricageproces.

List of figures

Figure1.1: Packaged $LiNbO_3$ modulator (source: https://www.thorlabs.com/) 4
Figure 1.2 : Applications of the ferroelectric thin films. 6
Figure 1.3 : Schematic of a tetragonal unit cell with a perovskite structure. The The yellow circle shows the position of the cation in a cubic perovskite 7
Figure 1.4 : Polarization-electric field hysteresis measurement. 9
Figure 1.5 : SEM image of the Si waveguide with a PZT capacitor on the top [51]. (b) Microscope top image (c) Schematic cross-section, of a Si ring resonator with top patterned gold electrode[52] 17
Figure 1.6 : Geometry of a C-axis oriented $BaTiO_3$ based electro optic modulator on MgO single crystalline substrate [64]. (b) BaTiO3 based Si slot waveguide modulator [65]. 20
Figure 2.1 : Flow chart representing the intermediate layer deposition. 37
Figure 2.2 : Flow chart of PZT/PLZT thin film deposition. 39
Figure 2.3 : Deposition procedure: ferroelectric thin films. 40
Figure 2.4 : AFM image of a La-based intermediate layer of thickness 10 nm and heat treated at 500°C 42

Figure 2.5 : XRD measurement of the La-based intermediate layer (thickness ~ 80 nm) at different tilt angles and the PZT layer deposited on the intermediate layer.............................. 43

Figure 2.6 : X-ray pole figure measurement of the PZT films (annealed at 630 °C, thickness ~ 300 nm) deposited on a La-based intermediate layer of 80 nm.................................. 43

Figure 2.7 : XRD patterns of PZT films annealed at 630°C, (a) thermally grown SiO_2 layers of different thickness (b) on ITO (30 nm) and PbTiO3 (50 nm) 46

Figure 2.8 : XRD pattern of the PZT thin films (annealed at 600°C), on intermediate layers of La, Pr and Nd, which are heat treated at 500°C, 450°C and 440°C, respectively. 47

Figure 2.9 : XRD patterns of the PZT films on silicon substrates annealed at 630 °C (a) On Nd and (b) La based intermediate layers of 10 nm, which has been heat treated at different temperatures. 49

Figure 2.10 : XRD patterns of the PZT films annealed at 600°C on a silicon substrate coated with La-based intermediate layers of different thickness (heat treated at 500°C)............. 50

Figure 2.11 : SEM top view image of the PZT films (annealed at 630°C) over a La-based intermediate layer of 15 nm, deposited (a) on a Si-slot waveguide of step height ~ 120 nm (b) on a Si-rib waveguide of step height ~ 70 nm. 53

Figure 2.12 : XRD pattern of the PZT film deposited on Si substrate coated with (a) La-based intermediate layer (heat treated at 500°C) (b) on Pr-based intermediate layer (475°C) of thickness 10 nm and annealed at different temperatures........ 54

Figure 2.13 : XRD patterns of PZT thin films annealed at 600°C, on different substrates coated with La-based intermediate layers (thickness ~ 10 nm, heat treated at 500ºC)................. 56
Figure 2.14 : XRD pattern of the PLZT thin film annealed at 600°C on La-based intermediate layers of 10 nm, which are heat treated at different temperatures. 57
Figure 2.15 : (a) SEM top view of the PZT thin film (thickness ~200 nm, annealed at 630 °C) deposited on silicon substrate, coated with a Nd- based intermediate layer (thickness ~10 nm, heat treated at 440 °C), (b) La- based intermediate layer (thickness ~10 nm, heat treated at 500 °C). (c) Cross-section image of PZT thin film (thickness ~200 nm) annealed at 630 °C (d) annealed at 560 °C, on a silicon substrate, coated with a La- based intermediate layer (thickness ~10 nm, heat treated at 500°C). (e), (f) TEM cross-section view of PLZT films deposited on La-based intermediate layer (heat treated at 500°C) and annealed at 600°C. 58
Figure 2.16 : (a) STEM image of the cross section of the PZT thin film (annealed at 630°C) on top of the $La_2O_2CO_3$ intermediate layer (heat treated at 500°C). The overlay shows the relative EDX signal intensity measured along the line marked by the two white arrows. For these intensities, only the elements La, Pb and Si were taken into account. (b) HRTEM image of the same cross-section, with indication of the (110) plane spacing in $La_2O_2CO_3$. The inset shows the FFT power spectrum for the PZT layer. 60

Figure 2.17 : AFM images of the PZT films deposited on Si substrates and annealed at 630˚C on (a) Nd (b) Sm (c) La (d) La-based intermediate layers. 61
Figure 2.18 : Flow chart representing the $BaTiO_3$/ $Ba(Zr,Ti)O_3$ preparation 62
Figure 2.19 : XRD patterns obtained for the BTO thin films: (a) BTO annealed at 700°C, with intermediate layers of different thickness (b) BTO annealed at different temperatures, with a 8.9 nm intermediate layer (c) BTO annealed at 700°C, with a 8.9 nm intermediate layer, heat treated at 450°C and 600°C 65
Figure 2.20 : XRD patterns obtained for BTO thin films deposited on an intermediate layer of thickness 8.9 nm and a BTO seed layer of 30 nm (a) annealing after each 30 nm BTO layer deposition, at different temperatures (b) annealing at 700°C after each 30 nm BTO layer deposition, or after four 30 nm BTO depositions (120 nm).......................... 67
Figure 2.21 : SEM top view of BTO thin films annealed at 700°C, with intermediate layer of (a) 6 nm (b) 7.2 nm. Cross section image of the BTO film deposited at 700°C (c) prepared with layer-by-layer annealing for each 30 nm layer, with a intermediate layer of 8.9 nm (d) deposited with an intermediate layer of 6 nm, as shown in Figure 2.21(a).The SEM cross-section images as shown in Figure 2.21(c) and Figure 2.21(d) are prepared by cleaving the silicon sample. 69

Figure 2.22 : AFM images of the BTO thin films deposited at 700°C, for different thicknesses of the intermediate layers (a) 6 nm (b) 7.2 nm. 70
Figure 2.23 : XRD measurements of the BZT thin films annealed at 700°C, on intermediate layers of La and Nd (thickness ~ 10 nm), which are heat treated at 500°C and 450°C, respectively. 71
Figure 2.24 : X-ray pole figure of $Ba(Zr,Ti)O_3$ thin film deposited on Si substrate coated with La-based intermediate layer of thickness ~ 10 nm and heat treated at 500°C. 72
Figure 2.25 : XRD measurements of the LiNbO3 thin films annealed at 700°C, on Si substrate coated with $La_2O_2CO_3$ intermediate layers of different thicknesses. 73
Figure 3.1 : Small-signal (Vac = 0.1V, f = 10 kHz) relative dielectric constant of the PZT(52/48) thin films (annealed at 630°C, thickness ~ 600 nm), on different template layers, as a function of applied electric field. 84
Figure 3.2 : Small-signal (Vac = 0.1V, f = 10 kHz) relative dielectric constant of the PZT thin films (annealed at 630°C, thickness ~ 600 nm) deposited on Pr-based template layer (heat treated at 500°C) for different Zr,Ti ratios. 85
Figure 3.3 : Small-signal (Vac = 0.1V) relative dielectric constant and dielectric loss of the PZT (52/48) thin films (annealed at 630°C, thickness ~ 600 nm), on different template layers, as a function of frequency (Edc = 0V). 86
Figure 3.4 : Sawyer-tower circuit to measure the P-E hysteresis of a ferroelectric capacitor. 87

Figure 3.5 : P-E hysteresis loop at different applied electric field for a PZT (52/48) thin film (annealed at 630°C, thickness ~ 600 nm) on a Si substrate coated with Nd-based intermediate layers (heat treated at 450°C, thickness ~ 10 nm). 88
Figure 3.6 : (a) P-E Hysteresis measurements of the PZT thin films (thickness ~ 600 nm, annealed at 630°C) (a) deposited on La based intermediate layer annealed at different temperature (b) deposited on different buffer layers and annealed at 630°C (c) deposited on Pr–based intermediate layer for different Zr:Ti ratios. The measurements are performed at 10 kHz. 90
Figure 3.7 : Leakage current measurements of the PZT films deposited on platinized Si substrates, coated with different intermediate layers and annealed at two different temperatures (electrode area- 3.14 mm2) 91
Figure 3.8 : AC dielectric constant as a function of the DC electric field bias for a BTO thin film (~ 200 nm) annealed at 700 °C with a 7.2 nm thick intermediate layer (b) P-E hysteresis loop measured at 1 KHz with an ac voltage swing of 10 V-PP , for the BTO films annealed at 700 °C with intermediate layers of different thickness. 93
Figure 3.9 : Schematic of the sample stack used for the electro-optic measurements 96
Figure 3.10 : Leakage current as a function of applied voltage for PZT films annealed at 630°C on a glass/ITO substrate coated with La-based intermediate layer (heat treated at 500°C). The leakage current is measured for an

electrode area of ~ 0.75 cm2 as used for the EO measurements. 97

Figure 3.11 : (a) Observed variation in Δ, as a function of the applied voltage (b) Change observed in Δ(V,λ)- Δ (0,λ) at 0V (Noise level) 5V, 10V, and 15V. 99

Figure 3.12 : Noise level extracted from the measurements using Δ(0,λ)- Δ1(0,λ).. 100

Figure 3.13 : (a) Δ angle at 0 V (b) The observed variations in the Δ angle at an applied voltage V = 15 V, calculated by Δ (15,λ)- Δ (0,λ). (c) $\partial\Delta(0,\lambda) / \partial\lambda$ 102

Figure 3.14 : Refractive index change and the effective electro-optic coefficients of the PZT thin film (thickness ~ 800 nm) annealed at (a) 630°C (b) 560°C, on different lanthanide based template layers (c) 630°C on La-based intermediate layers, with different Zr:Ti ratios.................... 104

Figure 3.15 : Refractive index change and the effective electro-optic coefficients of the PZT thin film (thickness ~ 800 nm) annealed at 590°C, on two different samples. 105

Figure 4.1 : Schematic cross section of a PZT/$BaTiO_3$ based modulator with an embedded electrode configuration......... 114

Figure 4.2 : Schematic cross section of a PZT/$BaTiO_3$ based modulator (TE polarization) with a co-planar electrode configuration... 116

Figure 4.3 : Schematic cross section of the heterogeneously integrated PZT/Si3N4 modulator with a co-planar electrode configuration... 118

Figure 4.4 : Simulation flow for the design of a PZT/Si_3N_4 waveguide modulator. 119
Figure 4.5 : TE Guided mode profiles of a Si_3N_4/ PZT (thickness= 100 nm) heterostructure (wavelength- 1310 nm), for a top oxide thickness of 50 nm and waveguide width of (a) 600 nm (b) 1600 nm. 121
Figure 4.6 : PZT confinement factor as a function of waveguide width (for TE polarization, wavelength= 1310 nm) for Si_3N_4/PZT hetero structures planarized with SiO_2 of (a) 100 nm (b) 50 nm, respectively. 122
Figure 4.7 : Electrode absorption loss as a function of waveguide width and electrode spacing for Si_3N_4/ PZT heterostructure (TE polarization) with a top oxide thickness of 50 nm and PZT thickness of (a) 100 nm (b) 150 nm, at λ= 1310 nm. 124
Figure 4.8 : Electrode absorption loss as a function of waveguide width and electrode spacing for Si_3N_4/ PZT heterostructure (TE polarization) with a top oxide thickness of 50 nm and PZT thickness of (a) 100 nm (b) 150 nm, at λ= 1310 nm. 125
Figure 4.9 : TE Guided mode profiles (wavelength- 1310 nm) of a (a) Si_3N_4 waveguide with no active PZT layer and (b) Si_3N_4/ PZT (thickness= 100 nm) heterostructure, for a top oxide thickness of 50 nm and waveguide width of 600 nm. 127
Figure 4.10 : Calculation of the transition mode-mismatch loss (for a single transition) Si_3N_4/ PZT hetero-structure (TE

polarization) as a function of waveguide width, PZT layer thickness and top oxide thickness, at λ= 1310 nm...... 128

Figure 4.11 : Simulated bend loss (wavelength- 1310 nm, TE polarization)for a Si_3N_4/ PZT hetero structure as a function of bending radius and waveguide width, for a top oxide of 50 nm and PZT thickness of 100 nm.............. 130

Figure 4.12 : Calculation of the voltage-Length product (VπLπ) for PZT on Si_3N_4 TE modulator structures with coplanar electrode configuration, with a top oxide thickness of 50 nm, at λ= 1310 nm.. 131

Figure 4.13 : Calculation of the voltage-Length product (VπLπ) as a function of waveguide width and PZT thickness for PZT/ Si_3N_4 TE modulator structure with a coplanar electrode configuration, with a top oxide thickness of 100 nm, at λ= 1310 nm.. 132

Figure 5.1 : (a) Example from literature: PZT films coated on a pattered SiO_2 film. The SiO_2 fil was formed on a Si substrate by wet oxidation and patterned to a 1 μm step by wet etching (source: [1]) (b) Our deposition: planarized Si waveguide with intermediate layer and PZT layer on top.. 138

Figure 5.2 : Fabrication procedure for PZT/ Si_3N_4 electro-optic devices 140

Figure 5.3 : (a) SEM image of the Si_3N_4/PZT waveguide patterned by RIE with a CF4 based chemistry. (b) Microscope image of the patterned Si_3N_4/PZT spiral waveguide used for loss measurements... 144

Figure 5.4 : Microscope image of the Si_3N_4/PZT structure (a) with first layer metal pattern (b) after final metallization 145
Figure 5.5 : (a) Loss extraction using spiral waveguides. Charateristics of MZI phaseshifter for a waveguide width of 640 nm and PZT thickness of 130 nm (b) before PZT deposition (c) after PZT deposition without pattering (d) after PZT patterning 146
Figure 5.6 : (a) Schematic of the MZI waveguide used for the electro-optic measurements. (b) Measurement set-up for electro-optic characterization. TL- Tunable laser, PC- Polarization controller, DUT- Device under test, PM- Power meter. 147
Figure 5.7 : MZI characteristics of a Si_3N_4/PZT waveguide of width 1.9 µm, electrode seperation of 5 µm and electrode length of 700 µm, under poled and unpoled condition. 148
Figure 5.8 : Electro-optic characterization of Si_3N_4/PZT MZI for an electrode length of 700 µm, electrode seperation of 5 µm and waveguide width of (a) 540 nm (b) 1.5 µm (c) 1.5 µm (from -50V to 50 V).. 151

List of tables

Table 1.1 : Tunable waveguide devices based on the piezo-electric properties of the ferroelectric thin film. 18

Table 1.2 : Electro-optic effects of ferroelectric thin films deposited by different fabrication techniques. 18

Table 1.3 : Electro-optic ferroelectric thin film based waveguide devices. 22

Table 2.1 : Comparison of different oxide based intermediate layers and thickness used for state-of-the-art PZT thin film growth 51

Table 2.2 : A comparison of different intermediate layers and thickness used for state-of-the-art $BaTiO_3$ thin film growth. 67

Table 2.3 : Overview of ferroelectric thin film depositions carried out over Ln-based intermediate layer 74

Table 3.1 : Comparison of dielectric properties between different PZT layers 86

Table 3.2 : Electrical measurement of ferroelectric thin films on different intermediate layers 94

Table 3.3 : different ferroelectric thin films and electro-optic characterisation techniques 95

Table 3.4 : Comparison of electro-optic properties between bulk and thin film materials. 106

Table 4.1 : Waveguide specifications for simulation of PZT/Si_3N_4 modulator Structures. 120

Table 5.1 : PZT dry etching with CHF_3/Ar plasma 143

List of Publications

Patents:

1. **John Puthenparampil George**, J.Beeckman and K. Neyts, "Preferentially Oriented Perovskite-related thin film," WO2014083195 A1, published on Nov 30, 2012

Journal Publications:

1. **John Puthenparampil George**, Jeroen Beeckman, Wouter Woestenborghs, P.F Smet, W. Bogaerts, K. Neyts., "Preferentially oriented BaTiO3 thin films deposited on silicon with thin intermediate buffer layers," Nano-scale research letters, 2013, 8, 1-7.

2. **John Puthenparampil George**, P. F. Smet, Jonas Botterman, Vitaly Bliznuk, Wouter Woestenborghs, D. Van Thouurhout, K. Neyts and Jeroen Beeckman., "Lanthanide-Assisted Deposition of Strongly Electro-optic PZT Thin Films on Silicon: Toward Integrated Active Nanophotonic Devices. ACS Applied. Materials and Interfaces 2015, 7 (24), 13350-13359.

3. Yufei Xing, Thomas Ako, **John Puthenparampil George**, Dietmar Korn, Hui Yu, Peter Verheyen, Marianna Pantouvaki, Guy Lepage, Philippe Absil, Alfonso Ruocco, Christian Koos, Juerg Leuthold, Kristiaan Neyts, Jeroen Beeckman and Wim Bogaerts,“ Digitally controlled phase shifter using an SOI slot waveguide with

liquid crystal infiltration," IEEE Photonics Technology Letters, 27. 2015. 1269-1272.

4. Oliver Willekens, **John Puthenparampil George**, K. Neyts and J. beeckman,"Ferroelectric Thin Films with Liquid Crystal for Gradient Index Applications," Light: Science & Applications, (submitted)

Conference Publications:

1. Yufei Xing, Thomas Akko, **John Puthenparampil George**, Dietmar Korn, Hui Yu, Peter Verheyen, Marianna Pantouvaki, Guy Lepage, Philippe Absil, Alfonso Ruocco, Christian Koos, Juerg Leuthold, Kristiaan Neyts, Jeroen Beeckman and Wim Bogaerts., Digitally controlled phase shifter using an SOI slot waveguide with liquid crystal infiltration," 11 th international conference on Group for IV photonics, 2014,,Paris, France

2. J. beeckman , **John Puthenparampil George**, K. Neyts and D. Van Thourhout., Ferroelectric thin films on silicon and glass for optical applications, Action ICI 1208 meeting, Prague, Czech Republic, 2014.

3. **John Puthenparampil George**, P. F. Smet, Wouter Woestenborghs, D. Van Thouurhout, K. Neyts and Jeroen Beeckman., Chemical solution deposition of PZt thin films on silicon substrates with thin intermediate layers, Joint UFFC," EFTF, and PFM symposium, 2013, Prague, Czech republic.

4. **John Puthenparampil George**, P. F. Smet, Wouter Woestenborghs, D. Van Thouurhout, K. Neyts and Jeroen Beeckman., Structural, electric and electro-optic properties of PZT thin films on ultr-thin lanthanide based Intermediate layers,"EMRS fall meeting, 2014, warsaw, poland.

5. **John Puthenparampil George**, Jeroen Beeckman, Wouter Woestenborghs, P.F Smet, W. Bogaerts, K. Neyts., Preferentially oriented BaTiO3 thin films deposited on silicon with thin intermediate layers," EMRS Spring meeting, 2013, Strasbourg, France.

6. **John Puthenparampil George**, P. F. Smet, Wouter Woestenborghs, D. Van Thouurhout, K. Neyts and Jeroen Beeckman., Ferro-electric

thin films for nano photonic devices, 4th annual world congress of advanced materials, 2015, China. (Invited talk)

7. Oliver Willekens, **John Puthenparampil George**, K. Neyts and J. beeckman, “PZT-based transmissive liquid crystal lens approach,” Eurodisplay, 2015, Gent, Belgium).

8. Oliver Willekens, **John Puthenparampil George**, K. Neyts and J. beeckman, “Liquid crystal devices with continuous phase variation based on high permittivity dielectrics,” SPIE Photonics West, February, 2016, San Francisco, CA (accepted).

9. Jeroen Beeckman, **John Puthenparampil George,** Dries Van Thourhout and Kristiaan Neyts,” PZT electro-optic modulators on the silicon nitride waveguide platform ,” EMRS, 2016, Lille (submitted)

10. D.Van thourhout, Z.Wang, B.Tian, Y.Hu, **John. Puthenparampil George**, J. Beeckman, M. Pantouvaki, C. Merckling, I. Asselberghs, S. Brems, P. Absil, J, Van Compenhout., New materials and devices for optical interconnect, OECC, 2015, Canada.

List of symbols

Symbols	*Description*
ε_0	Permittivity of Freespace
ε_r	Relative Permittivity
f	Frequency
k	Wave Vector
r_{eff}	Effective Electro-optic Coefficient
λ	Wavelength
Γ	Electro-optic Overlap Integral
V	Voltage
E	Electric Field
g	Spacing Between the Electrodes
n_{eff}	Effective Refractive Index
Δ	Phase Reflectance Ratio
Ψ	Amplitude Reflectance Ratio
n_e	Extra-ordinary Refractive Index
n_o	ordinary Refractive Index
P	*Polarization*

P_r	Remnant Polarization
P_r	Saturation Polarization
E_c	Coercive Electric Field
Pt	Platinum
Au	Gold
Cr	Chromium
Å	Angstroms
μm	Micrometer
pm	Picometer
t	time
Hz	Hertz
D	Electric Flux Density
T	Mechanical Stress
S	Mechanical Strain

List of abbreviations

Abbreviations	*Description*
AC	Alternating Current
AD	Aerosol Deposition
AFM	Atomic Force Microscope
ALD	Atomic Layer Deposition
BTO	Barium Titanate
BZT	Barium Zirconate Titanate
CMOS	Complementary Metal Oxide Semiconductor
DC	Direct Current
EO	Electro-Optic
FEM	Finite Element Method
FIB	Focussed Ion Beam
FRAM	Ferroelectric Random Access Memory
IMEC	Interuniversity Microelectronics Center
IPA	Isopropyl Alcohol
ITO	Indium Tin Oxide
IR	Infra-Red
LC	Liquid Crystal
MBE	Molecular Beam Epitaxy
MMI	Multi-mode Interference Coupler
MOCVD	Metal Organic Chemical Vapour Deposition

MZI	Mach-Zehnder Interferometer
PLD	Pulsed Laser Deposition
PLZT	Lead Lanthanum Zirconate Titanate
PVP	Polyvinylpyrrolidone
PML	Perfectly Matched Layer
PZT	Lead Zirconate Titanate
R	Reflection
RF	Radio Frequency
RIE	Reactive Ion Etching
SEM	Scanning Electron Microscope
SOI	Silicon on Insulator
T	Transmission
TE	Transverse Electric
TEM	Transmission Electron Microscope
TM	Transverse Magnetic
UV	Ultra Violet
XRD	X-Ray Diffraction
XRF	X-Ray Fluorescence

Chapter 1

Introduction

This chapter provides an introduction to the research carried out throughout the course of this study. First, a brief explanation on the context and objectives is given. Secondly, a description of the properties of ferroelectric thin films and their applications are given. Thirdly, a brief review of the state-of-the-art technology to integrate ferroelectric thin film materials on different substrates is presented. The following section provides a detailed literature review of state-of-the-art devices based on ferroelectric thin films for electro-optic applications. Finally, the structure of the thesis is presented, briefly addressing the content of each individual chapter.

1.1 Introduction

Ferroelectric thin films have been studied extensively over the past few decades because of the good piezo-electric [1], pyro-electric [2], ferro-electric [3] and electro-optic [4] properties. PZT thin films are used in applications such as ferro-electric thin film capacitors [5], piezo-electric actuators [6], electro-optic modulators [7], etc. Recent advances in thin film technology show nano-grained PZT films with excellent ferroelectric properties [8]. Novel devices with PZT nano-fibers have been demonstrated for mechanical energy harvesting [9]. Other interesting properties of the films such as the electron emission characteristics are also explored with nano-grained PZT structures, and a low turn on electric field is reported [10]. Although the ferroelectric thin films are explored mostly for electronic

applications, the ever increasing demand for higher bandwidth and lower power consumption in telecom and datacom applications has resulted in an increasing interest towards the use of electro-optically active films in the optical domain. To realize optical data transmission e.g. for chip to chip interconnects, integrated optical devices which are compatible with electrical systems are indispensable.

Ferroelectric oxides have long been used for signal processing in optical communication systems because of their excellent nonlinear optical properties. They are especially utilized in optical modulators because of their strong electro-optic effect. Ferroelectric $LiNbO_3$ is currently the material of choice for high-bandwidth electro-optic modulators used in optical communication systems [11]. A packaged $LiNbO_3$ modulator is shown in Figure 1.1.

Figure 1.1 Packaged $LiNbO_3$ modulator (source: https://www.thorlabs.com/)

The main advantage of using an external electro-optic modulator instead of directly modulating the semiconductor laser is the lack of chirp or wavelength variation. Other advantages include higher speed; data rates in excess of 40 Gb/s have been reported for $LiNbO_3$ modulators. Although high-bandwidth $LiNbO_3$ modulators have been demonstrated, there are other ferroelectrics with even larger electro-optic coefficients that potentially promise higher bandwidth and lower voltage operation.

Other ferroelectrics such as $LiTaO_3$, $KNbO_3$, $(Ba,Sr)TiO_3$, $BaTiO_3$, and PLZT have been considered for such applications. However, difficulties in the growth of large bulk single crystals have severely limited their utilization in practical devices. Furthermore, because they are used as bulk single crystals, they are not suitable for applications in integrated photonic circuits or optical interconnects.

1.2 Context and objective of this research

This PhD work is carried out in the framework of NB photonics, at Ghent University, Belgium. Part of this work is supported by an interuniversity attraction poles program of the Belgium science policy office, under grant IAP P7-35 (photonics@be). The PhD work is divided in 2 parts. The first half of the work is carried out within the liquid crystals and photonics group (LCP) of the department of electronics and information systems (ELIS). Here, we developed a method for depositing electro-optic materials on many standard substrates, with the goal of developing ultra-fast, compact, low power devices. The structural characterization of the films is carried with the help of lumi lab of the department of solid state physics, Ghent University. The second part of the work is carried out within the photonics research group (PRG), of the department of information technology, Ghent University. The design, fabrication, and characterization of the final devices are done within the cleanroom and characterization facilitates of PRG.

The detailed objectives of the work are:

- Develop a simple technique to deposit and grow ferroelectric thin films on Si, Si_3N_4 and other related waveguide platforms as an alternative to expensive and complex bonding processes. Compatibility with different substrate materials should allow possible use in future photonics devices on any type of material platform.
- The direct deposition of ferroelectric thin films on Si or Si_3N_4 substrates is still a challenge. The conventional metallic or conductive oxide based intermediate layers result in large optical absorption in the telecommunication wavelength regime (around 1300 nm or 1550 nm). The first half of the research is dedicated to investigating different possible dielectric thin films as intermediate layers for ferro-electric thin film deposition.
- Study the structural, electrical and electro-optic properties of the ferro-electric thin films, to understand the properties of the films for electro-optic modulators.
- Design of novel ferroelectric thin film based modulator structures on the well-developed Si and Si_3N_4 based waveguide platforms. The designs are intended to maximize the overlap of the electrical and optical signal in order to utilize the strong electro-optic coefficients of the ferro-electric thin films and to minimize the losses.

- To develop a standard procedure for the fabrication and characterization of the modulators. Techniques need to be developed to pattern the ferroelectric films using wet or dry etching without harming the underlying photonic circuits.

1.3 Properties of ferroelectric thin films

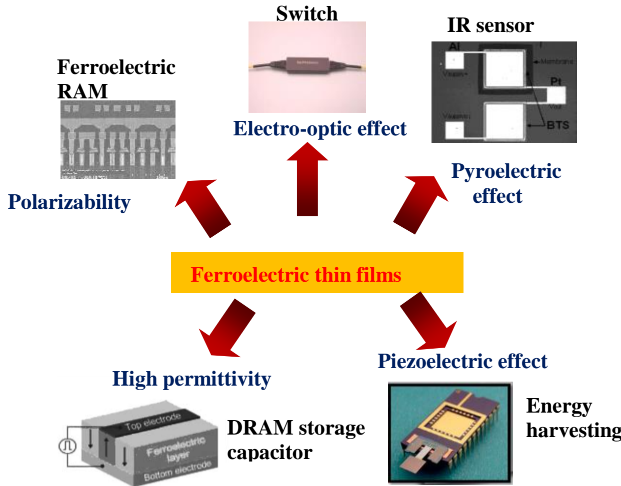

Figure 1.2: Applications of the ferroelectric thin films.

Figure 1.2 represents some of the applications of ferroelectric thin film based devices. Perovskite based thin films are used for a wide variety of applications based on their piezoelectric, ferroelectric, pyroelectric and electro-optic properties. A perovskite is any material with the same type of crystal structure as in $CaTiO_3$. Figure 1.3 shows the crystal structure of a perovskite material.

In general, the chemical formula of a perovskite is ABX_3, with oxygen at the face centers. A and B are cations with different sizes and X is the anion that bounds to both. The A atoms are larger than B atoms. For PZT and $BaTiO_3$, the A and B cations are Pb^{2+}/Ba^{2+} and Ti^{4+}/Zr^{4+}. The displacement of the Ti^{4+}/Zr^{4+} center results in the change of the cubic unit cell to a tetragonal one and causes a spontaneous polarization below the curie temperature. This section briefly reviews the properties of the ferroelectric thin films and their applications.

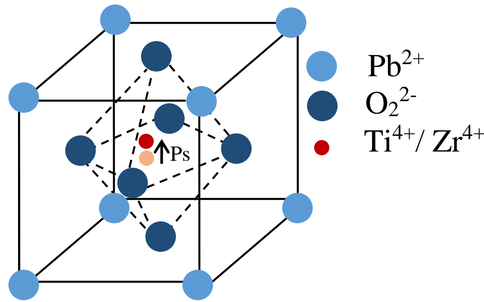

Figure 1.3: Schematic of a tetragonal unit cell with a perovskite structure. The The yellow circle shows the position of the cation in a cubic perovskite.

Piezoelectric properties: Piezoelectricity is a coupling between the mechanical and electrical behaviour of a material. When ferroelectric thin films are subjected to tensile or compressive forces, it results in a strain of the material. This strain in turn generates an electrical charge inside the materials. The phenomenon is the direct piezoelectric effect [12]. Conversely when an electrical field is applied, strain is created together with resulting stress. This is called the converse piezoelectric effect. In crystals that possess piezoelectric properties, the electrical properties such as electric field, polarization and mechanical properties such as stress and strain are interrelated. The basic relationships between the electrical and elastic properties can be represented as follows:

$$D = d * T + \varepsilon^T * E$$

$$S = s^E * \mathrm{T} + \mathrm{d} * \mathrm{E}$$

Where D, T, E, S, d, ε^T, s^E represents the electric flux density, mechanical stress, electric field, mechanical strain, piezoelectric charge coefficient, permittivity (for T= constant), compliance or elasticity coefficient (for E= constant). Ferroelectric materials such as PZT (52/48), and PZT's doped with La and Sr exhibit the strongest piezoelectric effects [13]. The piezoelectric properties of PZT films are used for a wide spectrum of applications. The typical values for the d_{33} piezoelectric coefficient of the PZT films is in the order of 200- 600 pm/V [14].

In spite of the complex fabrication, piezoelectric film based devices are gaining attention. A wide variety of devices are fabricated, tested and analysed for a rather comprehensive evaluation of their potential and

limitations. This includes ultrasonic micromotors[15], micropumps[15] and microvalves accelerometers[16] and gyroscopes[17], acoustic sensors[18], sensing and actuating elements in atomic force microscope AFM cantilevers[19], rf and optical switches and ultrasonic transducers [20]for medical and sonar applications. The advantages of using piezoelectric materials for MEMS based devices (actuators, and transducers) are the high generated force and good actuating range, a wide frequency range of operation and a low power consumption.

Ferroelectric properties: ferroelectricity means that a material has a spontaneous dipole moment that leads to a macroscopic polarization. In most materials the dipole moments are averaged leading to zero polarization when no fields are applied. The polarization in ferroelectric materials can be re-oriented with an applied electric field. The ferroelectric properties of the films are measured with polarization-electric field hysteresis loop. The electrical hysteresis of the films originates from the electrical switching of the ferroelectric domains. The electrical hysteresis of the films can be used for example in realizing ferroelectric random access memory (FRAM). Texas instruments, Inc. USA, has demonstrated the MSP430FR series of micro controllers based on the FRAM technology (http://www.ti.com/lsds/ti). This FRAM's writes data 100 times faster while consuming half the energy compared to conventional flash based micro controllers.

The principle of non-volatile ferroelectric random access memories or FRAMs is based on the polarization reversal by an external applied electric field of metal-ferroelectric-metal capacitors. The computational "0" and "1" are represented by the non-volatile storage of the negative or positive remnant polarization state, respectively. The destructive readout operation is performed via the displacement current. FRAMs show attractive electronic properties, for example, write and read cycle times in the sub-100 ns range and low power consumption, which are in most cases superior to the performance of other non-volatile technologies.

In Figure 1.4, the polarization at zero electric field ($E = 0$) is referred to as remnant polarization P_r. The minimum field required to switch the polarization direction ($P = 0$) is referred to as the coercive field E_C. Typical values for the remnant polarization and coercive field for a PZT (52/48) composition lie between of 10- 60 μC/cm^2 and 50-150 kV/cm [21].

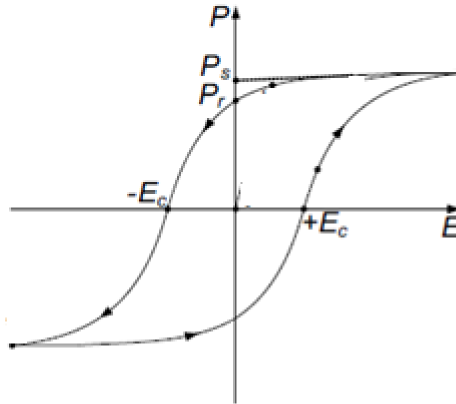

Figure 1.4: Polarization-electric field hysteresis measurement.

Pyroelectric-properties: Out of the twenty crystal classes that exhibit the piezoelectric effect, ten of them exhibit a unique polar axis. The appearance of pyroelectricity solely depends on the crystal structure). All polar materials are pyroelectric and they possess a spontaneous polarization. Pyroelectricity means that a material's polarization is changed as a result of temperature changes of the material [22]. When the material is heated the dipole moments inside the material change, which leads to a polarization change. This change in polarization leads to the creation of an electrical potential difference. Although a material does not need to be ferroelectric to exhibit pyroelectric properties, the best pyroelectric materials are all ferroelectric. The phenomenon of pyroelectricity is frequently used to detect IR radiation using ferroelectric crystals. The pyroelectric effect is utilized in thin film pyroelectric IR detector arrays for the thermal detection of objects and persons [23]. Lead oxide based perovskites such as $PbTiO_3$, PZT and PLZT are preferred for this application because of their high pyroelectric coefficient, low dielectric loss, high resistivity and high curie temperature. Pyroelectric coefficient may be represented as the change in the spontaneous polarization vector ($P_{s,i}$) as a function of temperature.

$$p_i = \partial P_{s,i} / \partial T$$

Where p_i is the vector for the pyroelectric coefficient. Typical values for the pyroelectric coefficient are in the order of 10- 50 nC/cm^2 K^{-1}.

Electro-optic properties: Generally, when an external electric field is applied to a material a refractive index change is produced (or a

birefringence is induced). This electro-optic response of ferroelectric perovskite oxides has important implications for optical devices as it permits the modification of the phase velocity of electromagnetic waves in the material by the application of an electric field [11]. The propagation of the electromagnetic wave in a dielectric medium can be described in terms of the impermeability tensor $\eta = \varepsilon_0 \varepsilon^{-1}$. The elements η_{ij} are altered with the application of an external electric field E and become a function of *E*. The impermeability tensor can be expanded in a taylor series about $E = 0$.

$$\eta_{ij}(E) = \eta_{ij}^0 + \sum_k r_{ijk} E_k + \sum_{kl} S_{ijkl} E_{kl} \qquad I, j, k, l = 1, 2, 3$$

Where r_{ijk} and S_{ijkl} represent the linear (pockels) and quadratic (kerr) electro-optic coefficient respectively. The details of the ferroelectric electro-optical thin film properties and the devices based on these are described in detail in section 1.6.

1.4 Ferro-electric thin films -- fabrication methods and challenges

The integration of ferroelectric thin films with active microelectronic components for electro-optic devices has been made possible through the advancements in the fabrication technology for complex multicomponent oxides. A variety of methods has been used to deposit high quality ferroelectric thin films: chemical solution deposition (CSD) [24], RF magnetron sputtering [25], metal organic chemical vapour deposition (MOCVD) [26], pulsed laser deposition (PLD) [27] and molecular beam epitaxy (MBE) [28]. All techniques have inherent advantages and disadvantages and the choice of the deposition technique used depends on the application. One of the biggest concerns for electro-optic devices based on the ferroelectric thin film is to minimize the scattering loss and to obtain a high electro-optic coefficient. In order to achieve this, it is required to have single crystalline thin films or highly oriented polycrystalline thin films, which can only be obtained by the hetero-epitaxial thin film growth or by the deposition over a lattice matched highly oriented intermediate layers.

Good piezoelectric and electro-optic properties of the films have been obtained for annealing temperatures above 550°C and 650°C. Such temperatures are problematic if direct integration of PZT thin films onto integrated circuits is the goal. The Al metallization hardly survives post

processing temperatures above 500°C. Therefore, the metallization step with Al has to be carried out after the ferroelectric thin film processing. For CMOS compatibility is it expected that annealing needs to occur at temperatures lower than 500°C. Other metals, such as Pt, can withstand the high annealing temperatures.

Among the many possible deposition techniques, the chemical solution deposition technique is widely used because of the precise composition control, simplicity in processing and cost-effectiveness. Solution derived films are either deposited by spin-coating or dip-coating. The ferroelectric films are subject to a two-step heating process: one at lower temperature smaller than 350°C to pyrolyze the organic content and a second one at high temperature of more than 550°C to crystallize the film. The main drawback for optical applications of this film is the typical polycrystallinity and the possibility of residual porosity, both of which increase the scattering loss [29]. With the recent improvements in solution based processing, the CSD method demonstrated both thin as well as thick (> 10 µm) highly oriented, dense, polycrystalline thin films deposited on a lattice matched MgO substrate which exhibit the strongest electro-optic pockels effect, with reasonably low propagation loss of about 4 dB/cm [7].

The most important physical deposition techniques used for ferroelectric thin films are sputtering (RF and DC magnetron) and pulsed laser deposition (PLD). In PLD, a short wavelength, high-power laser such as an excimer laser is used to evaporate a ceramic target. The vaporized material is condensed onto the substrate, which is typically heated up to a certain temperature. The advantage of this physical evaporation technique is that it allows the deposition of the material on a layer-by-layer basis. These techniques are typically used to produce ferroelectric films of LiNbO3 [30], PLZT [31], PZT [32], PSZT [33], $BaTiO_3$ [1], and BST [34]. The disadvantages of this technique to fabricate multicomponent materials is that the sputtering yield and sticking coefficients of different components are not equal, therefore it requires very precise control of the sputtering rate, the ambient conditions, the heating rate and the partial pressure to have stoichiometric films with good quality.

Other methods such as metal organic chemical vapour deposition (MOCVD) and atomic layer deposition (ALD) are known for producing optical quality ferroelectric thin films. Volatile metallic-organic precursors are vaporized and transported to a reaction chamber where they react and deposit onto the heated substrate. In-situ deposition of high quality, epitaxial $BaTiO_3$ thin

films are reported before based on both MOCVD [35] and ALD [36] techniques. The advantage of these techniques is that the films are conformal and the methods suited for a manufacturing environment. The disadvantage is that stable, volatile precursors of some cationic species such as Zr are not readily available.

The fabrication technologies for PZT based ferroelectric materials are studied more than any other ferroelectric material. One of the main issues associated with PZT and PLZT material is the volatility of the lead oxide. This problem is usually solved by fabricating a lead rich film to compensate for the lead loss associated with the high temperature firing process. Typically 10 % to 20 % excess lead is added to the Pb precursors. The same problem can also be observed in all other Pb based ferroelectric material such as PSZT, $Pb(Mg,Nb)O_3$ and $Pb(Sc,Ta)O_3$ and also for other materials such as $KNbO_3$ that contain the volatile species potassium. Chemical compatibility of the ferroelectric thin films with the substrate material at the annealing temperature is another issue with the ferroelectric thin film growth. The large lattice mismatch and difference in the thermal expansion coefficients also prevents the epitaxial growth of these films on such substrates. The film shows cracks even at a low annealing temperature (< 500°C) and produces intermediate fluorite/silicate phases rather than pure perovskite phase. This will deteriorate the thin film properties. In the case of crystalline materials such as Si, GaAs and amorphous materials such as SiO_2 or Si_3N_4 an intermediate buffer layer is required to promote the film growth. The buffer layers typically act as a diffusion barrier (especially for Pb containing ferroelectric materials), seed layer (for ferroelectric thin film growth) and also to release the thermal stress developed on ferroelectric films during the high temperature firing process. Furthermore, to obtain epitaxial films an epitaxially grown buffer layer is required. So, for optical applications ferroelectric thin deposition was thus far limited to single crystalline lattice matched substrates, such as MgO [1], $SrTiO_3$, Nb:$SrTiO_3$ [2] and sapphire [37]. Recent investigations show advancements towards the growth of ferroelectric thin films on Si substrates using the complex molecular beam epitaxy (MBE) technique. A thin film (~ 8 - 10 nm) epitaxially grown $SrTiO_3$ template layer is grown initially as a template layer to promote the epitaxial growth of the subsequently deposited $BaTiO_3$ layer [28]. Also techniques are demonstrated to grow highly c-axis textured epitaxial PZT films on both GaAs and Si substrates by growing highly c-axis textured MgO intermediate thin films.

1.5 Si based modulator technology

Optical technology is poised to revolutionise short reach interconnects. The leading candidate technology is silicon photonics and the workhorse of such interconnect is the optical modulator. While the demand for the optical interconnect is significant, minimising the performance metrics such as the energy per bit and device footprint, whilst maximising bandwidth and modulation depth are non-trivial demands. All of this must be achieved preferably using CMOS compatible fabrication processes with acceptable thermal tolerance and optical spectral width.

An integrated optical modulator is a device that modulates light beams propagating inside an optical waveguide in the sense than one or more fundamental characteristics of the light beam is varied. Modulator can be classified as amplitude, phase or polarization modulators. In addition, modulators can also be classified based on their underlying physical mechanism being either electro-absorption or electro-refraction.. The primary electric field effects that are traditionally useful in semiconductor materials for causing either electro-absorption or electro-refraction are the Pockels effect, the Kerr effect and the Franz-Keldysh effect. However, these effects are weak in Si at telecommunication wavelengths. Due to the centrosymmetric crystal structure of Si, it does not exhibit a linear electro-optic (Pockels) effect. The kerr effect ($\Delta n \sim 10^{-5}$, for an electric field of 10^5 kV/cm) and franz-keldysh effect ($\Delta n \sim 10^{-8}$, for an electric field of 10^5 kV/cm) have very low efficiencies in Si. Alternative techniques are therefore required to achieve modulation in Si platform. One method to induce refractive index variations is thermal modulation in Si, thereby exploiting the large thermo-optic coefficient of Si.This method is rather slow Modulators working up to 1 MHz are demonstrated with these method [38]. Higher frequencies are required for the modern telecommunication applications.

The most common technique used in silicon devices for modulators to date is the plasma dispersion effect, in which the concentration of free carriers in silicon changes the real and imaginary part of the refractive index. Electrical manipulation of the charge density interacting with the propagating light is achievable through mechanisms such as carrier injection, accumulation or depletion. The change in the refractive index observed is necessarily accompanied by a detrimental change in the absorption via free carriers. Most of the carrier injection based devices are p-i-n (p-type/intrinsic/n-type

layers) diode structures that are formed around a waveguide to electrically control the injection of electrons and holes into the path of the propagating light. To avoid excessive optical loss, the waveguides are positioned in the intrinsic region of the diode. Thedoped regions are positioned such that the modal overlap is sufficiently low. Carrier injection based devices operating up to 18 Gbits s^{-1} have been reported [39]. In devices based on carrier accumulation free carriers are accumulating on either side of a dielectric layer inside a micrometer-sized waveguide (much like in a capacitor) rather than by carrier injection. Carrier accumulation modulators (on-chip loss of 10 dB) with data rates of 10 Gbits s^{-1} and an extinction ratio of 3.8 dB have reported [40]. The speed of the carrier injection based devices is limited by the minority carrier life time in silicon, whereas carrier accumulation based modulators are limited by the RC time constant.

Carrier depletion is another technique that manipulates free-carrier densities in a modulator. Devices based on carrier depletion operate by allowing the propagating light to interact with the junction region of a p–n diode operated at reverse bias. The diode’s depletion width, and therefore the free-carrier density in the waveguide, varies with the applied reverse bias. Carrier depletion modulators (4 dB on-chip loss including 1.8 dB phase shifter loss) working in excess of 40 Gbits s^{-1} is reported [41]. A high modulation efficiency is possible using a carrier injection based device, but at the expense of modulation speed. The opposite is true for depletion devices, in which modulation speeds in excess of 30 GHz (phase shifter loss of 3.6dB±0.4dB) can be reached [42], but at reduced efficiency.

Over the past few years there have been attempts to investigate alternative modulation mechanisms in materials that are compatible with Si technology, to achieve more efficient modulation. The Franz-keldysh effect and the quantum-confined Stark effect (QCSE) both introduce electric-field-induced changes in the optical absorption. The CMOS compatible Ge or SiGe material system exhibits strong electro-absorption. SiGe electro-absorption based modulators with a 3-dB bandwidth of 40.7GHz and an operating wavelength range of 35 nm near 1550 nm is reported [43]. Graphene is another material which generates interest because of its high carrier mobility and broadband absorption. It is a promising material for making fast, broad band electro-absorption modulators [44, 45]. Broadband 10 Gbits s^{-1} graphene electro-absorption modulators are reported on Si [46]. Devices operating at 30GHz bandwidth with a state-of-the-art modulation efficiency

of 15 dB for 10 V is also reported with graphene on Si_3N_4 waveguide modulators [47].

Another approach for optical modulation is to employ ferroelectric or organic materials and integrate them together with Si photonic devices. Hybrid integration of organic and ferroelectric thin films on Si for modulators has been demonstrated in recent years [48, 49]. Unlike Si, some other materials such as $LiNbO_3$ exhibit strong pockels effect, which makes them suitable candidates for optical modulation application [11]. Moreover, the electro-optic modulators do not suffer from carrier induced speed limitations. Organic materials have the advantage of strong, ultrafast nonlinear responses, broad spectral tunability and lower refractive index (1.4 to 2.5 typically). Combining the organic materials with a Si slot waveguide structure (where the optical intensity is maximum in the low index slot regions), modulators with a 3-dB bandwidth in excess of 100 GHz are reported with a voltage length product of 1.1 V.cm [49]. The use of organic material with stronger pockels coefficients (up to 230 pm/V) reduces the voltage-length product down to 0.5 V.mm.

Ferroelectric thin film based electro-optic materials exhibit a larger pockels coefficient (745 pm/V for PLZT films) compared to the organic materials [50]. In our work we focussed on the integration of ferroelectric films on Si or Si_3N_4 based waveguide platforms to develop electro-optic modulators. A discussion on state-of-the-art ferroelectric thin film based devices is provided in the following sections.

1.6 Photonic devices- based on ferroelectric thin films

Ferroelectric oxides have long been used for signal processing in optical communication systems because of their excellent nonlinear optical properties. They are especially utilized in optical modulators because of their strong electro-optic effect. For example, ferroelectric $LiNbO_3$ is currently the material of choice for high-bandwidth electro-optic modulators used in optical communication systems [11].

Most of the optical devices reported till date, are based on single crystalline perovskite substrates or single crystalline perovskite thin films epitaxially grown on lattice matched MgO or $SrTiO_3$ substrates. Examples of some reported structures are mentioned in the following sections. In order to utilize the advantage of the well-developed CMOS photonics platform, it is essential to deposit the ferroelectric thin directly on Si or Si_3N_4 waveguides.

The state-of-art tunable photonic devices based on these platforms are based on two different approaches. It uses either the piezo-electric or electro-optic properties of the ferroelectric thin films. To use the piezo-electric properties for tuning, a ferroelectric capacitor is formed over the Si waveguide. By applying a voltage across the ferroelectric thin film, it expands or contracts, which introduce strain in the Si. It breaks the centro-symmetry of the Si to introduce the electro-optic effects. On the second approach, epitaxial PZT/$BaTiO_3$ films are deposited on directly over Si, as a cladding layer or forming a slot waveguide structure using complex molecular beam epitaxy (MBE) technique.

1.6.1 Piezo-electrically tuned optical waveguides

Piezoelectrically induced thickness changes of the PZT films can be converted to an effective change in the refractive index of the optical waveguides by the photoelastic effect [51]. In order to efficiently convert the piezoelectric effects to a refractive index change, a PZT capacitor is formed over the waveguide structures. Either the PZT layers or the gold electrodes over the PZT are designed and patterned carefully to transfer the strain generated from the PZT layer effectively to the bottom Si/Si_3N_4 waveguides. The bottom electrode of the capacitor is a Ti/Pt metal combination. Here, the Pt metal is used both as an intermediate layer to promote PZT nucleation as well as to serve as a bottom electrode for the capacitor. Since the Pt layers are deposited directly over the top of the waveguides, it results in strong absorption of the propagating optical mode. To overcome this problem, a sufficiently thick SiO_2 layer needs to be deposited over the waveguide prior to capacitor formation.

Advantages:

- The deposition of the ferroelectric thin films is fairly easy, as the capacitors are formed using a well-studied Pt intermediate layer

- The capacitors on Pt based intermediate layers can be used regardless of the waveguide substrates. It means that the method is useful on all waveguide platforms.

Disadvantages:

- Thick oxide layers are required to avoid electrode absorption losses

- The thick oxide layers reduce the efficiency of the strain transfer, thus the refractive index changes observed are rather low (See Table 1.1).

- Only low speed devices are demonstrated. The piezoelectric effect is intrinsically limited in speed.

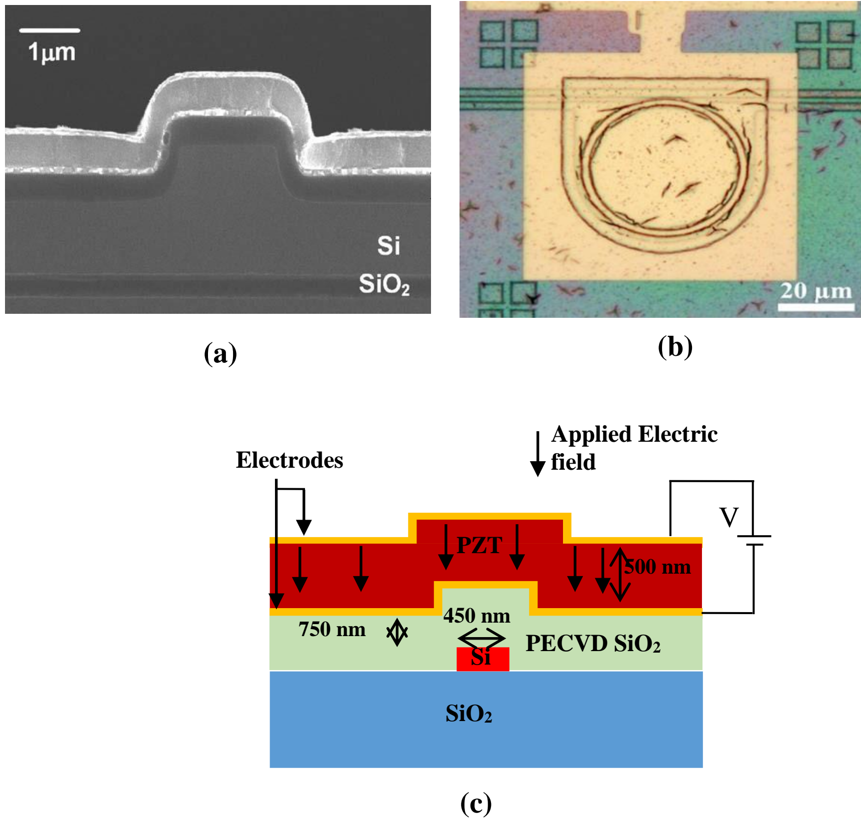

Figure 1.5: SEM image of the Si waveguide with a PZT capacitor on the top [51]. (b) Microscope top image (c) Schematic cross-section, of a Si ring resonator with top patterned gold electrode[52]

The details of tunable waveguide devices based on the piezoelectric effect demonstrated in literature are given in Table 1.1.

Table 1.1: Tunable waveguide devices based on the piezo-electric properties of the ferroelectric thin film.

Waveguide Platform	**Growth Technique**	**Type of Films**	**Intermediate Layer**	**Δn_{eff} (Experimental)**
Si [53]	chemical solution deposition (CSD)	$Pb(Zr_{0.52}Ti_{0.48})O_3$	Ti/Pt	3.5e-5 (5V)
Si [54]	chemical solution deposition (CSD)	$Pb(Zr_{0.52}Ti_{0.48})O_3$	Ti/Pt	1.6e-4 (6V)
Si_3N_4 [55]	pulsed laser deposition (PLD)	$Pb(Zr_{0.52}Ti_{0.48})O_3$	Ti/Pt	5.1e-6 (16V)

Table 1.2: Electro-optic effects of ferroelectric thin films deposited by different fabrication techniques.

Substrate	Growth Technique	Type of Films	Pockels Coefficients
LSAT [58]	pulsed laser deposition (PLD)	$Ba_{0.7}Sr_{0.3}TiO_3$	125 pm/V
Si/$SrTiO_3$ [59]	aerosol deposition (AD)	$Pb(Zr_{0.52}Ti_{0.48})O_3$	102 pm/V
$MgAl_2O_4$ [55]	MOCVD	$KNbO_3$	470 pm/V
Nb:$SrTiO_3$ [2]	RF sputtering	$Pb(Zr_{0.52}Ti_{0.48})O_3$	135 pm/V
Nb:$SrTiO_3$ [60]	sol-gel	PLZT (8/65/35)	390 pm/V
SrRuO3/YSZ/Si [61]	sol-gel	$Pb(Zr_{0.52}Ti_{0.48})O_3$	60 pm/V

Substrate	**Growth Technique**	**Type of Films**	**Pockels Coefficients**
r-sapphire [62]	RF sputtering	PLZT(8/65/35)	326 pm/V
Si [63]	sputtering	$LiNbO_3$	18 pm/V
Si/$SrTiO_3$[28]	MBE	$BaTiO_3$	148 pm/V
Si [59]	aerosol deposition	PLZT (9/65/35)	44 pm/V
$LaAlO_3$ [58]	PLD	BST	230 pm/V
Glass [4]	RF sputtering	$Pb(Zr_{0.52}Ti_{0.48})O_3$	109 pm/V

Where n is the refractive index, r is the linear electro-optic coefficient and E is the applied electric field component. A number of ferroelectric oxide thin films have been deposited and their electro-optic properties characterized (see Table 1.2). Different techniques such as the lock-in detection[36], interferometry techniques [56], prism coupling [57] and spectroscopic ellipsomtery [2] are used to characterize the electro-optic properties of the ferroelectric thin film. The electro-optic pockels coefficient of a variety of ferroelectric thin films reported previously are provided in Table 1.2.

It is clear from Table 1.2 that a number of thin films exhibit pockels coefficients in excess of 100 pm/V. However, work carried out on conventional Si or Si_3N_4 platforms is very limited. The epitaxial growth of $BaTiO_3$ on Si is reported recently. An effective pockels coefficient of 148 pm/V[28] is obtained, when measured a lock-in detection technique. The deposition require more sophisticated MBE technique for both the intermediate $SrTiO_3$ and $BaTiO_3$ layers and it is limited to crystalline Si substrate. Most of the previous work on Si use thick (~ 100 nm) intermediate layers for thin film growth and electro-optic properties of these films are not measured [33]. When these films are used as a cladding on Si waveguides, the evanescent field interacting with the active ferroelectric thin film is much smaller. This will reduce the effective pockels coefficient of the films on Si/Si_3N_4 waveguide based devices.

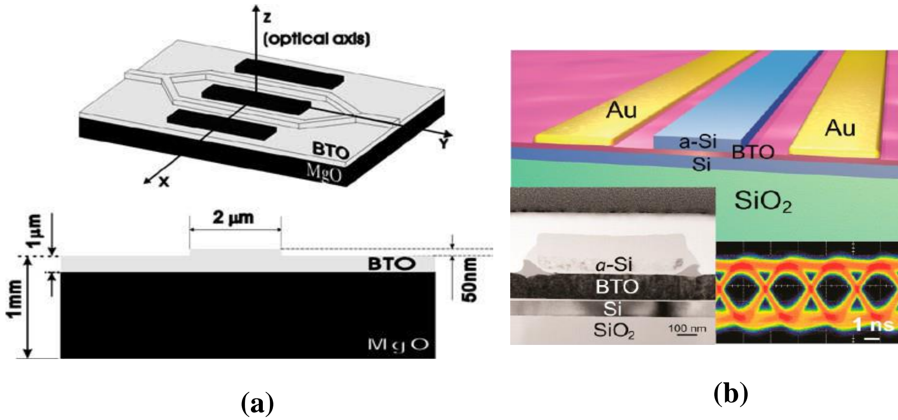

(a) (b)

Figure 1.6: Geometry of a C-axis oriented $BaTiO_3$ based electro optic modulator on MgO single crystalline substrate [64]. (b) $BaTiO_3$ based Si slot waveguide modulator [65].

1.6.2 Electro-optic tuning optical waveguides

The two main electro-optic effects in ferroelectric materials are the linear electro-optic (pockels) effect and the quadratic electro-optic effect. For the pockels effect the refractive index of the material varies linearly as a function of the applied electric field according to a relation of the form,

$$\Delta n(\mathrm{E}) = -\frac{n^3 rE}{2}$$

A wide range of modulators and electro-optic switches have been demonstrated with ferroelectric thin films. Figure1.6 represents some examples of electro optical modulators already demonstrated on MgO and Si. Figure 3(a) represents the design of a realized $BaTiO_3$ modulator with ridge type waveguides fabricated with ion beam etching [64]. Both C-axis (out of plane spontaneous polarization) and A-axis modulators (in plane spontaneous polarization) were demonstrated. Electrodes of 3 mm length are used for the EO measurements of these devices. For C-axis devices a half wave voltage $V_\pi = 6.3$ V ($V_\pi L_\pi = 1.89$ V.cm) at 632 nm wavelength and $V_\pi = 9.5$V ($V_\pi L_\pi = 2.85$ V.cm) at 1550 nm wavelength are obtained. For the a-axis

samples V_π= 8V ($V_\pi L_\pi$ = 2.4 V.cm) at 632 nm wavelength and V_π = 15V ($V_\pi L_\pi$ = 4.5 V.cm) at 1550 nm are obtained [64].

Even though there are a number of attempts to fabricate high speed electro-optic devices based on ferroelectric thin films, the first high speed operation was reported with epitaxial $BaTiO_3$ films deposited on MgO in 2004 [66]. The epitaxial $BaTiO_3$ thin film on the MgO substrate forms a composite structure with a low effective dielectric constant of 20.8 at 40 GHz. A 3.9 V half-wave voltage with a 3.7 GHz 3-dB bandwidth and a 150 pm/V effective electro-optic coefficient is obtained for the 3.2 mm-long modulator at 1.55 µm [67]. Further improvements in the thin film technology showed ferroelectric films with pockels coefficients close to the bulk values. With modified fabrication procedures and controlled ambient high temperature annealing, epitaxial PLZT (8/65/35) and polycrystalline $BaTiO_3$ thin films with pockels coefficients of 490 pm/V and 300 pm/V respectively are reported [68]. Ferroelectric epitaxial PLZT thin-film based mach-zehnder-type waveguide modulators with 2.5 mm long travelling wave electrodes are also demonstrated with this method. The use of a composite structure with a low dielectric coefficient substrate and a buffer layer enabled a PLZT thin-film waveguide modulator with 40-Gb/s operation [68]. A $V_\pi L_\pi$ product of 1.85 V.cm is obtained for these PLZT modulators.

Even though most of the devices are demonstrated on epitaxial ferroelectric thin films, good quality polycrystalline $BaTiO_3$ films developed on MgO substrates are also reported for electro-optic devices [7]. The deposition parameters are optimized to achieve optical-quality films with an attenuation coefficient of 4 dB/cm at 633 nm wavelength. Thin-film electro-optic mach-zehnder modulators were fabricated with standard lithography and ion-beam etching [7]. The waveguides patterned by lithography are ridge type and they ensure single-mode propagation in the wavelength range of 633-1550 nm. A Cr-Au electrode of 3 mm is used for EO measurements. An electro-optic coefficient of 22 pm/V and $V_\pi L_\pi$ of 4.5 V.cm is obtained for the polycrystalline $BaTiO_3$ waveguides.

The polycrystalline PLZT films are also reported for fabricating optical modulators. For this work, the PLZT thin films (randomly oriented) are deposited by aerosol deposition method [69],[69]. The Si is only used as a substrate in this work, where the waveguides are fabricated on the PLZT thin films. These devices are fabricated with an embedded electrode configuration with the PLZT layers sandwiched between upper and lower electrode. The waveguides are formed in a reverse ridge configuration by

etching a thick SiO_2 layer deposited over the bottom electrode layer. The etched SiO_2 layer provide the lateral confinement of the propagating mode. The PLZT core and the cladding layers (for vertical confinement) are subsequently deposited over the etched SiO_2 film to form a waveguide with reverse ridge structure. Here, the PLZT core layer is formed by PLZT (5/70/30) layer of refractive index 2.4 and the top and bottom cladding layers by a perovskite oxide layer of refractive index 2.05. For electro-optic characterisations, the voltages are applied perpendicular to the PLZT layers. The optical characterization measurements show a 2 GHz optical signal produced by the modulator. The loss associated with the device is rather high (about 40 dB/cm), possibly due to the absorption of the optical signal by the top and bottom electrodes.

Recent research demonstrated the first Si based slot waveguide modulator structure incorporating epitaxially deposited $BaTiO_3$ as active medium [65]. Figure 1.6(b) show the $BaTiO_3$ slot waveguide modulator on Si with epitaxial $SrTiO_3$ buffer layers. The waveguide structure is formed by depositing a thin layer of amorphous Si over the epitaxial $BaTiO_3$ thin film. The a-Si layer is further patterned to form the optimized slot waveguide structure. The gold electrodes are deposited on $BaTiO_3$ with a planar distribution. Using the on-chip photonic interferometers an effective electro-optic co-efficient of 213±49 pm/V, a value six times larger than that typically obtained for $LiNbO_3$ modulators is reported. The monolithically integrated optical ring modulators show a modulation bandwidth of 4.9 GHz, which is promising for broadband applications. A list of different electro-optic devices reported based on ferroelectric thin films is given in Table 1.3. The high electro-optic coefficients of these films also attracted interest to make electro-optic devices commercially as an alternative to $LiNbO_3$ based technology. Epi-photonic, inc. demonstrated the first commercial PLZT based devices. They reported arrayed waveguide grating (AWG) based electro-optic switches with a switching time of 15 ns, fabricated with epitaxially grown PLZT thin films on Nb:$SrTiO_3$ substrate (www.epiphotonics.com/technology.html).

Table 1.3: Electro-optic ferroelectric thin film based waveguide devices.

Thin film material	**Substrate**	**Growth technique**	**FOM**	**Measurement method**
$BaTiO_3$ [64]	MgO	PLD	V_π- 8.9V (at 1550 nm)	MZI

Thin film material	**Substrate**	**Growth technique**	**FOM**	**Measurement method**
PLZT [70]	Si	aerosol deposition	V_π- 20 V (2 GHz)	MZI
PZT [71]	$SrTiO_3$	solid phase epitaxy	r_{eff}- 46 pm/V	MZI
BST [72]	MgO	PLD	r_{eff}- 27 pm/V	MZI
PLZT [73]	Nb:$SrTiO_3$	PLD	r_{eff}- 710 pm/V (at 1550 nm)	MZI
$BaTiO_3$ [65]	Si	MBE	r_{eff}- 213±49 pm/V	MZI and Ring resonators
$BaTiO_3$ [7]	MgO	MOCVD	r_{eff}- 22 pm/V (at 1550 nm)	MZI
$BaTiO_3$ [67]	MgO	MOCVD	r_{eff}- 150 pm/V (at 1550 nm)	MZI

<u>Advantages:</u>

- Due to the strong pockels coefficient of ferroelectric thin films, devices with very low voltage-length product can be designed.

- High speed modulators are possible

<u>Disadvantages:</u>

- The deposition of ferroelectric thin films on Si or Si_3N_4 waveguide platforms is very challenging.

- Currently the deposition of high quality ferro-electric thin films on Si substrate is limited to the use of the complex and expensive MBE technique.

- The MBE methods can be only used when the substrates are crystalline. It limits the application on other waveguide platforms.

1.7 Thesis structure

This thesis is organized in a step-by-step approach that leads to the final modulator device. Apart from the first chapter, which addresses motivations, context, objectives and challenges of this work, the main contents of the thesis is structured as follow:

Chapter 2 gives an overview of the preparation of the ferro-electric thin films on crystalline and amorphous substrates. Different issues related to the choice of substrate materials and intermediate layers for thin film growth are addressed. The influence of different intermediate layers on the structural, crystallization, and electrical properties of the ferro-electric thin film are studied. The details of the chemical solution deposition (CSD) technique developed and followed in this work are presented. The importance of the intermediate layers to grow oriented ferroelectric thin films on different substrates is studied in detail. The choice of the intermediate layers and role of the phase transitions on the subsequent deposited ferroelectric thin films are presented. A novel technique developed during the course of this research to grow ferro-electric PZT/BTO/LNB thin films on silicon and glass substrates is presented in detail. The detailed optimization of the films in terms of the annealing temperature, the pyrolysis temperature, the buffer layer heat treatments and the thickness of the intermediate layers is presented. The influence of the processing parameters on the micro-structure of the ferro-electric thin films has been studied in detail. SEM, AFM and TEM analysis has been used to study the micro-structure, roughness and lattice parameters of the thin films. X-Ray diffraction and the pole figure measurements are used to study the crystallization and orientation of the films on many different substrates. TEM studies confirm the epitaxial growth of the films on thin intermediate buffer layers. The SEM and AFM measurements confirm the PZT growth with smooth, well packed polygonal crystal grains, which are suitable for photonic applications.

Chapter 3 introduces electrical and electro-optic characterization of the PZT thin films. All the thin films are electrically characterized for their dielectric properties, ferroelectric properties and leakage current characteristics. These measurements demonstrate well saturated hysteresis loops, large dielectric constants and low leakage currents. An ellipsometry based method has been

followed to extract the electro-optic properties of the thin films. Our measurements based on different annealing conditions and various intermediate layers are explained in detail. The measurements prove the strong electro-optical nature of the films and demonstrate that they are ideal for heterogeneously integrated photonic devices on the Si and Si_3N_4 waveguide platform. The structurally characterized thin films are used to further measure the electrical properties.

Chapter 4 is divided in three different sections. The first section deals with the simulations of the modulator structures. The design of Si_3N_4 based modulator structures with PZT claddings are presented here. Different electrode configurations (embedded and co-planar) are proposed for the modulators to explore the strongest tensor components. Firstly, the simulations of the Si_3N_4/PZT structures are carried out. Since the PZT films possess a high refractive index compared to Si_3N_4, a novel modulator structure is proposed with very thin layers (100 to 150 nm) of PZT as cladding. This structure is further optimized for a better confinement inside the PZT active layer, maximum overlap between the electrical and optical signal, low electrode absorption losses, low transition mode-mismatch loss and low bend losses. The simulation results confirm that the structures exhibit a low $V_\pi L_\pi$ comparable to state-of-the-art modulator devices.

In Chapter 5 the fabrication and characterization of Si_3N_4 /PZT modulators is explained in detail. The PZT thin films are deposited on a SiO_2 planarized Si_3N_4 waveguide. The PZT films are patterned using an ICP Reactive ion etching system and the etching process is explained in detail. The electrodes are fabricated on a co-planar configuration, using a conventional UV lithography process. In the third section, the characterization of the devices is explained. The modulators are characterized in detail for their DC characteristics. Waveguides of different widths are characterized to estimate the $V_\pi L_\pi$ product. We show that the devices performance is comparable to the state-of-the-art devices.

Finally, a summary of the results from this research work and some potential future research directions in the development of a high speed electro-optic modulators are presented in Chapter 6.

1.8 References

1. Kobayashi, T., et al., Microelectromechanical systems-based electrostatic field sensor using Pb(Zr,Ti)O-3 thin films. Japanese Journal of Applied Physics, 2008. 47: p. 7533.
2. Kang, T.D., et al., Large electro-optic effect in single-crystal Pb(Zr, Ti)O(3) (001) measured by spectroscopic ellipsometry. Journal of Applied Physics, 2008. 104(9).
3. Lei, X.Y., et al., Dielectric, ferroelectric and piezoelectric properties of 100-oriented Pb0.4Sr0.6TiO3 thin film sputtered on LaNiO3 electrode. Journal of Crystal Growth, 2012. 347: p. 15.
4. Zhu, M.M., Z.H. Du, and J. Ma, Influence of crystal phase and transparent substrates on electro-optic properties of lead zirconate titanate films. Journal of Applied Physics, 2010. 108: p. 113119.
5. Amit, Y., et al., Semiconductor nanorod layers aligned through mechanical rubbing. Physica Status Solidi a-Applications and Materials Science, 2012. 209(2): p. 235-242.
6. Luo, C., G.Z. Cao, and I.Y. Shen, Development of a lead-zirconate-titanate (PZT) thin-film microactuator probe for intracochlear applications. Sensors and Actuators a-Physical, 2013. 201: p. 1-9.
7. Petraru, A., et al., Integrated optical Mach-Zehnder modulator based on polycrystalline BaTiO3. Optics Letters, 2003. 28(24): p. 2527-2529.
8. Datta, A., et al., Hierarchically Ordered Nano-Heterostructured PZT Thin Films with Enhanced Ferroelectric Properties. Advanced Functional Materials, 2014. 24(18): p. 2638-2647.
9. Bakhoum, E.G. and M.H.M. Cheng, Novel Capacitive Pressure Sensor. Journal of Microelectromechanical Systems. 19(3): p. 443-450.
10. Datta, A., et al., Controlled Ti Seed Layer Assisted Growth and Field Emission Properties of Pb(Zr0.52Ti0.48)O-3 Nanowire Arrays. Acs Applied Materials & Interfaces, 2013. 5(13): p. 6261-6267.
11. Wooten, E.L., et al., A review of lithium niobate modulators for fiber-optic communications systems. Ieee Journal of Selected Topics in Quantum Electronics, 2000. 6(1): p. 69-82.
12. Panda, P.K. and B. Sahoo, PZT to Lead Free Piezo Ceramics: A Review. Ferroelectrics, 2015. 474(1): p. 128-143.
13. Sriram, S., et al., Measurement of high piezoelectric response of strontium-doped lead zirconate titanate thin films using a nanoindenter. Journal of Applied Physics, 2007. 101(10).

14. Sriram, S., et al., Thin film piezoelectric response characterisation using atomic force microscopy with standard contact mode imaging. Micron, 2009. 40: p. 109.
15. Izyumskaya, N., et al., Processing, structure, properties, and applications of PZT thin films. Critical Reviews in Solid State and Materials Sciences, 2007. 32(3-4): p. 111-202.
16. Wang, L.P., et al., Design, fabrication, and measurement of high-sensitivity piezoelectric microelectromechanical systems accelerometers. Journal of Microelectromechanical Systems, 2003. 12(4): p. 433-439.
17. Parent, A., et al., Design and Performance of a PZT Coriolis Vibrating Gyro (CVG), in 2006 15th IEEE International Symposium on Applications of Ferroelectrics. 2007, Ieee: New York. p. 219-222.
18. Wang, Z.Y., C. Wang, and L.T. Liu, Design and analysis of a PZT-based micromachined acoustic sensor with increased sensitivity. Ieee Transactions on Ultrasonics Ferroelectrics and Frequency Control, 2005. 52(10): p. 1840-1850.
19. Watanabe, S. and T. Fujiu, PZT thin film actuator/sensor for atomic force microscope. Isaf '96 - Proceedings of the Tenth Ieee International Symposium on Applications of Ferroelectrics, Vols 1 and 2, ed. B.M. Kulwicki, A. Amin, and A. Safari. 1996, New York: I E E E. 199-204.
20. Li, J.H., et al., Micromachined ultrasonic transducers based on lead zirconate titanate (PZT) films. Microsystem Technologies-Micro- and Nanosystems-Information Storage and Processing Systems, 2013. 19(2): p. 211-218.
21. Pandey, S.K., et al., Electrical properties of PZT thin films grown by sol-gel and PLD using a seed layer. Materials Science and Engineering B-Solid State Materials for Advanced Technology, 2004. 112(1): p. 96-100.
22. Bowen, C.R., et al., Pyroelectric materials and devices for energy harvesting applications. Energy & Environmental Science, 2014. 7(12): p. 3836-3856.
23. Bruchhaus, R., et al., Optimized PZT thin films for pyroelectric IR detector arrays. Journal of Electroceramics, 1999. 3(2): p. 151-162.
24. Cooney, T.G. and L.F. Francis, Processing of sol-gel derived PZT coatings on non-planar substrates. Journal of Micromechanics and Microengineering, 1996. 6: p. 291-300.
25. Frunza, R., et al., Preparation and characterisation of PZT films by RF-magnetron sputtering. Journal of Alloys and Compounds, 2011. 509: p. 6242-6246.

26. Menou, N. and H. Funakubo, (111)-oriented Pb(Zr,Ti)O(3) films deposited on SrRuO(3)/Pt electrodes: Reproducible preparation by metal organic chemical vapor deposition, top electrode influence, and reliability. Journal of Applied Physics, 2007. 102: p. 114105.
27. Borowiak, A.S., et al., Pulsed laser deposition of epitaxial ferroelectric Pb(Zr,Ti)O-3 films on silicon substrates. Thin Solid Films, 2012. 520: p. 4604-4607.
28. Abel, S., et al., A strong electro-optically active lead-free ferroelectric integrated on silicon. Nature Communications, 2013. 4: p. 1-6.
29. Xu, Z.M., et al., Monolithically integrated optical modulator based on polycrystalline Ba0.7Sr0.3TiO3 thin films. Applied Physics Letters, 2006. 88(16).
30. Sumets, M., et al., Sputtering condition effect on structure and properties of LiNbO3 films. Journal of Materials Science-Materials in Electronics, 2015. 26(6): p. 4250-4256.
31. Bin, C., et al., Tunable photovoltaic effects in transparent Pb(Zr 0.53,Ti 0.47)O 3 capacitors. Applied Physics Letters, 2012. 100: p. 173903
32. Chirila, C., et al., Comparison between the ferroelectric/electric properties of the PbZr0.52Ti0.48O3 films grown on Si (100) and on STO (100) substrates. Journal of Materials Science, 2015. 50(11): p. 3883-3894.
33. Sriram, S., et al., Nanocolumnar Preferentially Oriented PSZT Thin Films Deposited on Thermally Grown Silicon Dioxide. Nanoscale Research Letters, 2009. 4(1): p. 29-33.
34. Hongtao, X., N.K. Pervez, and R.A. York, Tunable microwave integrated circuits BST thin film capacitors with device structure optimization. Integrated Ferroelectrics, 2005. 77: p. 27-3535.
35. Kim, D.S. and C.H. Lee, Preparation of Barium Titanate Thin Films by MOCVD Using Ultrasonic Nebulization. Ferroelectrics, 2010. 406: p. 130-136.
36. Abel, S., et al., A strong electro-optically active lead-free ferroelectric integrated on silicon. Nature Communications, 2014. 4: p. 1-6.
37. Braun, W., et al., EPITAXIAL LEAD-ZIRCONATE-TITANATE THIN-FILMS ON SAPPHIRE. Applied Physics Letters, 1993. 63(4): p. 467-469.
38. Cocorullo, G., et al., SILICON THERMOOPTIC MICROMODULATOR WITH 700-KHZ - 3-DB BANDWIDTH. Ieee Photonics Technology Letters, 1995. 7(4): p. 363-365.

39. Manipatruni, S., et al., High speed carrier injection 18 Gb/s silicon micro-ring electro-optic modulator, in 2007 Ieee Leos Annual Meeting Conference Proceedings, Vols 1 and 2. 2007, Ieee: New York. p. 537-538.
40. Liao, L., et al., High speed silicon Mach-Zehnder modulator. Optics Express, 2005. 13(8): p. 3129-3135.
41. Liao, L., et al., 40 Gbit/s silicon optical modulator for highspeed applications. Electronics Letters, 2007. 43(22): p. 1196-1197.
42. Ding, R., et al., Design and characterization of a 30-GHz bandwidth low-power silicon traveling-wave modulator. Optics Communications, 2014. 321: p. 124-133.
43. Feng, D.Z., et al., High speed GeSi electro-absorption modulator at 1550 nm wavelength on SOI waveguide. Optics Express, 2012. 20(20): p. 22224-22232.
44. Bolotin, K.I., et al., Ultrahigh electron mobility in suspended graphene. Solid State Communications, 2008. 146(9-10): p. 351-355.
45. Mak, K.F., et al., Measurement of the Optical Conductivity of Graphene. Physical Review Letters, 2008. 101(19).
46. Hu, Y.T., et al., Broadband 10Gb/s Graphene Electro-Absorption Modulator on Silicon for Chip-Level Optical Interconnects. 2014 Ieee International Electron Devices Meeting (Iedm), 2014.
47. Phare, C.T., et al., Graphene electro-optic modulator with 30 GHz bandwidth. Nature Photonics, 2015. 9(8): p. 511-+.
48. Xiong, C., et al., Active Silicon Integrated Nanophotonics: Ferroelectric BaTiO3 Devices. Nano Letters, 2014. 14: p. 1419-1425.
49. Alloatti, L., et al., 100 GHz silicon-organic hybrid modulator. Light-Science & Applications, 2014. 3.
50. Masuda, S., et al., Mach-Zehnder Interferometer-Type Photonic Switches Based on Epitaxially Grown Lanthanum-Modified Lead Zirconate Titanate Films. Journal of Lightwave Technology, 2011. 29: p. 209-214.
51. Tsia, K.K., S. Fathpour, and B. Jalalia, Electrical tuning of birefringence in silicon waveguides. Applied Physics Letters, 2008. 92: p. 061109.
52. Sebbag, Y., et al., Bistability in silicon microring resonator based on strain induced by a piezoelectric lead zirconate titanate thin film. Applied Physics Letters, 2012. 100: p. 141107.
53. Tsia, K.K., S. Fathpour, and B. Jalalia, Electrical tuning of birefringence in silicon waveguides. Applied Physics Letters, 2008. 92(6).

54. Sebbag, Y., et al., Bistability in silicon microring resonator based on strain induced by a piezoelectric lead zirconate titanate thin film. Applied Physics Letters, 2012. 100(14).
55. Hosseini, N., et al., Stress-optic modulator in TriPleX platform using a ezoelectric lead zirconate titanate (PZT) thin film. Optics Express, 2015. 23(11): p. 14018-14026.
56. Spirin, V.V., C.H. Lee, and K.S. No, Measurement of the Pockels coefficient of lead zirconate titanate thin films by a two-beam polarization interferometer with a reflection configuration. Journal of the Optical Society of America B-Optical Physics, 1998. 15: p. 1940-1946.
57. Boudrioua, A., et al., Electro-optic characterization of (Pb, La)TiO3 thin films using prism-coupling technique. Journal of Applied Physics, 1999. 85(3): p. 1780-1783.
58. Kang, T.D., et al., Large electro-optic effect in single-crystal Pb(Zr, Ti)O(3) (001) measured by spectroscopic ellipsometry. Journal of Applied Physics, 2008. 104: p. 093103.
59. Nakada, M., K. Ohashi, and J. Akedo, Optical and electro-optical properties of Pb(Zr,Ti)O-3 and (Pb,La)(Zr,Ti)O-3 films prepared by aerosol deposition method. Journal of Crystal Growth, 2005. 275(1-2): p. E1275-E1280.
60. Masuda, S., A. Seki, and Y. Masuda, Influence of crystal phases on electro-optic properties of epitaxially grown lanthanum-modified lead zirconate titanate films. Applied Physics Letters, 2010. 96(7).
61. Kondo, M., et al., Electrooptic properties of lead zirconate titanate films prepared on silicon substrate. Japanese Journal of Applied Physics Part 1-Regular Papers Brief Communications & Review Papers, 2006. 45(9B): p. 7516-7519.
62. Uchiyama, K., et al., Electro-optic properties of lanthanum-modified lead zirconate titanate thin films epitaxially grown by the advanced sol-gel method. Japanese Journal of Applied Physics Part 2-Letters & Express Letters, 2007. 46(8-11): p. L244-L246.
63. Akazawa, H. and M. Shimada, Spectroellipsometric approach to determine linear electro-optic coefficient of c-axis-oriented LiNbO3 thin films. Journal of Applied Physics, 2005. 98(11).
64. Petraru, A., et al., Ferroelectric BaTiO3 thin-film optical waveguide modulators. Applied Physics Letters, 2002. 81(8): p. 1375-1377.
65. Xiong, C., et al., Active Silicon Integrated Nanophotonics: Ferroelectric BaTiO3 Devices. Nano Letters, 2014. 14(3): p. 1419-1425.

66. Lin, Y.Y., et al., XPS analysis of Pb(Zr0.52Ti0.48) O-3 thin film after dry-etching by CHF3 plasma. Applied Surface Science, 2000. 165(1): p. 34-37.
67. Tang, P.S., et al., Electrooptic modulation up to 40 GHz in a barium titanate thin film waveguide modulator. Optics Express, 2004. 12(24): p. 5962-5967.
68. Masuda, S., et al., Electro-optic and dielectric characterization of ferroelectric films for high-speed optical waveguide modulators. Journal of Applied Physics, 2011. 109(12).
69. Nakada, M., et al., Lanthanum-Modified Lead Zirconate Titanate Electro-Optic Modulators Fabricated Using Aerosol Deposition for LSI Interconnects. Japanese Journal of Applied Physics, 2009. 48(9).
70. Shimizu, T., et al., Gigahertz-rate optical modulation on Mach-Zehnder PLZT electro-optic modulators formed on silicon substrates by aerosol deposition. Ieice Electronics Express, 2009. 6(23): p. 1669-1675.
71. Nashimoto, K., et al., Fabrication of electro-optic Pb(Zr, Ti)O-3 heterostructure waveguides on Nb-doped SrTiO3 by solid-phase epitaxy. Applied Physics Letters, 1999. 74(19): p. 2761-2763.
72. Wang, D.Y., et al., Linear electro-optic effect in Ba0.7Sr0.3TiO3 thin film grown on LSAT (001) substrate. Integrated Ferroelectrics, 2007. 88: p. 12-+.
73. Masuda, S., et al., Mach-Zehnder Interferometer-Type Photonic Switches Based on Epitaxially Grown Lanthanum-Modified Lead Zirconate Titanate Films. Journal of Lightwave Technology, 2011. 29(2): p. 209-214.

Chapter 2

Deposition Methods and structural Characterization

This chapter discusses the novel fabrication techniques we developed for depositing ferroelectric thin films on a variety of substrates and their structural characterization. Even though the work is focussed on ferroelectric lead zirconate titanate (PZT) thin films, we have also investigated other important electro-optic, ferro-electric thin films such as barium titanate ($BaTiO_3$), barium zirconate titanate ($Ba(Zr,Ti)O_3$) [1] and lithium niobate ($LiNbO_3$) [2]. Ba-based ferroelectric thin films are developed as an alternative for Pb-free ferroelectrics, even though Pb based films have shown superior properties.

The electro-optical properties of PZT thin films depend strongly on the quality and crystallographic orientation of the thin films. Our studies focused on the requirement of an efficient template or intermediate layer to promote a highly textured (strong orientation along a specific crystallographic axis) thin film growth. At the same time, this layer should also act as an efficient diffusion barrier. We developed a novel deposition method following the chemical solution deposition (CSD) route for both ferroelectric thin films as well for the intermediate layers. This technique is used to realize highly textured PZT, $BaTiO_3$, $Ba(Zr,Ti)O_3$ and $LiNbO_3$ thin films on a variety of substrates such as bare silicon, glass (corning glass type CB90IN (Delta

Technologies)), Glass/ITO, Si/Al_2O_3, Si/SiO_2 and Si/Si_3N_4 waveguides. Since our aim is to prepare ferroelectric thin films for photonic devices, the primary objective is to investigate dielectric thin films, which exhibit very low optical absorption, as the intermediate layers. Secondly, the aim is to develop ultra-thin intermediate layers, so that the ferro-electric films can be effectively used as active cladding layers for waveguide based optical devices and to assure optimal overlap of the optical field with the active layer. In this work, we have demonstrated a number of different ultra-thin lanthanide based dielectric intermediate layers of thickness 5 to 15 nm. We successfully demonstrated ferroelectric thin film growth on this intermediate layers. The films are structurally characterized with X-ray diffraction (XRD), X-ray pole figure measurement, scanning electron microscope (SEM), atomic force microscope (AFM), transmission electron microscope (TEM) etc.

Section 2.1 discusses different techniques for ferroelectric thin film growth and associated challenges. Section 2.2 to section 2.5 elaborates on the chemical solution deposition technique developed for the deposition of intermediate layers and Pb-based ferroelectric thin films. In the following section, the structural characterization (X-ray diffraction, pole figure, SEM, AFM and TEM) of the intermediate layer and the Pb-based ferroelectric thin films are discussed in detail. Section 2.6 to 2.8 and section 2.13 describes the preparation, deposition and structural characterizations of $BaTiO_3/Ba(Zr,Ti)O_3$ and $LiNbO_3$ thin films respectively. Finally, section 2.14 give an overview of the different ferroelectric thin film deposition carried out and types of intermediate layers used.

2.1 Deposition of the PZT thin films - Current deposition methods and challenges

A variety of methods has been used to develop ferroelectric thin films: chemical solution deposition (CSD) [3], RF magnetron sputtering [4], metal organic chemical vapour deposition (MOCVD) [5] and pulsed laser deposition (PLD) [6] are commonly used methods. However, the direct deposition of PZT on silicon substrates still remains a challenge. It is reported that there is inter-diffusion between the Si and the PZT thin film at a high annealing temperature, which makes it hard to form the perovskite PZT phase. Different methods have been proposed and demonstrated to use either a seed or a barrier layer to promote thin film growth [7]. The

nucleation of the PZT thin films strongly depends on the underlying substrate and the interface properties [8]. The dielectric, piezo-electric and electro-optical properties of the thin films depend strongly on the crystal orientation. It is reported that strongly c-axis-oriented PZT thin films can be grown on either single-crystalline oxide substrates or by using a preferentially oriented thick (>100 nm) conductive or dielectric intermediate layer [9].

Metallic intermediate layers are preferred for electrical devices, but often such layers cannot be used for electro-optical devices because the optical absorption is too high. A thick intermediate layer is not necessarily a drawback for certain applications of PZT, but for applications in electro-optical devices the performance is severely limited by the thickness of this layer [9]. Recent works show advancements towards micro and nano scale EO devices on the silicon platform based on complex and costly layer bonding approaches [10] and with more sophisticated epitaxially grown ferroelectric oxides [11].

In the following sections, we explain a rather simple technique based on the CSD method developed in our lab, which employs ultra-thin intermediate dielectric layers to grow highly textured ferroelectric thin films regardless of the substrate material. The films are structurally characterized to confirm the highly textured crystal growth. We believe that it is an alternative to more expensive and sophisticated thin film growth techniques.

2.2 Chemical solution deposition

The CSD method can rely on different deposition methods such as spin coating and aerosol deposition. When depositing films using aerosol, the chemical precursors are atomized to form an aerosol and then deposited on a rotating substrate. Deposition can be enhanced by electrostatic charging of the aerosol. The desired thickness can be obtained using different deposition times and optimising the number of deposited layers. When using spin coating as deposition method, the desired thickness can be obtained by varying the number of deposited layers, spin speed and molar concentration. The advantage of CSD deposition over vacuum deposition methods lies in a better composition control in multicomponent systems, the ability to produce relatively large area coating and the low capital investment required for the equipment. The CSD deposition of $PbTiO_3$ and $Pb(Zr,Ti)O_3$ thin films were first reported by Gurkovich and Budd [12]. In order to prepare the PZT films

Budd et al. used lead trihydrate, titanium isopropoxide, zirconium n-propoxide as source precursor material for Pb, Ti, Zr and 2–methoxy ethanol as solvent. Driven by the potential applications of the PZT films for devices, further optimizations of the PZT films [13] at the early stages were published from the Sandia national laboratories [14], [13, 15].

The CSD method has been widely used to produce PZT thin films for various applications such as capacitors, microelectromechanical systems (MEMS) devices and electro-optic devices. PZT films continue to be developed for other applications, such as ferroelectric RAMs, sensors, bulk acoustic wave (BAWs) and surface acoustic wave (SAW) devices. The CSD method consists of four steps: precursor solution preparation, deposition of the solution onto a substrate by spin coating or aerosol, pyrolysis of organic species at low temperature (300°C–500°C) to obtain amorphous films and crystallization of amorphous films to the desired perovskite phase and densification at high temperature (600°C–700°C).

The crystallization path is typically separated into three different stages [16],[17]. Firstly, the amorphous phase transforms into an oxygen deficient pyrochlore/fluorite phase of $Pb_2(Zr,Ti)_2O_{7-x}$, in the temperature range between 300°C to 600°C. Secondly, the PZT phase starts crystallizing from temperatures above 475°C. Finally, for annealing temperatures above 700°C and for long time exposure, a new lead deficient phase such as $Pb(Zr,Ti)_3O_7$ starts to appear due to the volatilization of PbO. However, this crystallization path depends on many different parameters [18] . The transformation from the amorphous to the perovskite phase strongly depends on the annealing temperature, the annealing ambient, the type of substrates, the solution chemistry, the lead excess precursor and the intermediate layers.

The CSD method is illustrated in Figure 2.1 and Figure 2.2. In this chapter, details of each step for the preparation of PZT thin films are discussed and the crystallization behaviour of PZT thin films with respect to different processing conditions provided in earlier literature are reviewed.

2.3 Preparation and deposition of intermediate layers

Requirement and choice of precursor materials: In this work lanthanide-based thin films are used as intermediate layers for the PZT deposition. The nitrates salts of lanthanides such as $La(NO_3)_3.6H_2O$, $Nd(NO_3)_3.6H_2O$, $Pr(NO_3)_3.6H_2O$ and $Sm(NO_3)_3.6H_2O$ dissolved in 1-propanol are used as precursor solution for intermediate layer preparation.

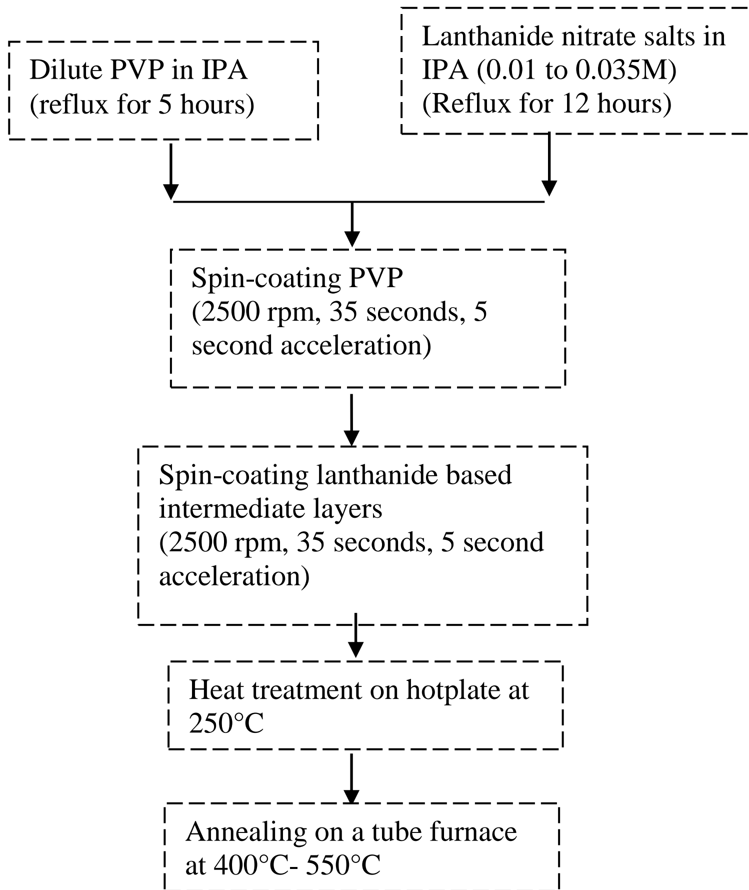

Figure 2.1: Flow chart representing the intermediate layer deposition.

The thermal decomposition of the lanthanide nitrate salts used for intermediate layers produces stable intermediate crystalline phases and finally converted into corresponding oxides after high temperature PZT annealing. Lanthanide oxides are good insulating films and exhibits good optical transparency, which could be ideal for optical devices. We found that specific intermediate crystalline phases formed during the thermal decomposition of the precursor materials results in highly oriented ferroelectric thin films. The structural characterizations of both intermediate layers and ferroelectric thin films are explained in section 2.6. The

intermediate layers are all deposited following a solution deposition procedure as given in Figure 2.1.

We performed the initial experiments with a number of well-known intermediate layers such as ITO, $PbTiO_3$, SiO_2 (see section 2.6.2.1). But after a large number of depositions and characterizations, it is found that the lanthanide based intermediate layers gave the best results with a preferentially oriented PZT thin films.

Deposition procedure: Direct spin-coating of lanthanide based nitrate salts show dispersed solution drops on all spin coated substrates. In order to improve the adhesion, a PVP solution is spin coated prior to the lanthanide based solution for the intermediate layer. Firstly, the PVP (Polyvinylpyrrolidone, avg. molecular weight ~ 40000, sigma aldrich) powder is dissolved (40 wt%) in water and refluxed for 24 hours. The resulting solution shows a pale yellow colour. This solution is preserved as a stock PVP solution. Secondly, PVP solutions are further diluted in 1-propanol (0.1 gram of the stock solution in 40 ml of 1-propanol.) to get the final solution [19]. After the solution is prepared, it is spin coated onto the substrate at 2500 rpm for 35 seconds at an acceleration of 500 rpm/second. The spin-coated substrate is placed on a hot plate at 250°C to get rid of the solvent.

Subsequently, the amorphous films are annealed in a tube furnace at 450 to 550°C, with a ramping rate of 100°C/min (equipment limitation) for 20 minutes, depending on the type of intermediate layers used. For example, when using the lanthanum based intermediate layers annealing is carried out at 475°C, whereas for praseodymium based intermediate layers it is at 415°C to get a highly (100) textured PZT film. The details of the intermediate layers, their annealing temperature and the resulting PZT texture are mentioned in the following sections.

2.4 PZT and PLZT preparation

The flow chart representing the PZT/PLZT precursor solution preparation is described in Figure 2.2. The PZT (52/48) precursor solution is prepared with a 20 % excess of lead to compensate for lead loss during the crystallization heat treatments at 600°C to 650°C. We follow a 2-methoxy ethanol based chemical solution route. Firstly, the lead acetate hydrate salt is dissolved in 2-methoxy ethanol and vacuum distilled at 100°C for 3 hours. In the case of PLZT, lanthanum acetate is also added to lead acetate in required proportion

before distillation. Later, Ti-isopropoxide, and Zr-isoproxide solutions are mixed and chelated in stoichiometric proportion inside a glove box, before mixing it with the distilled lead acetate to get the final solution. The molarity of the final solution is 0.4M.

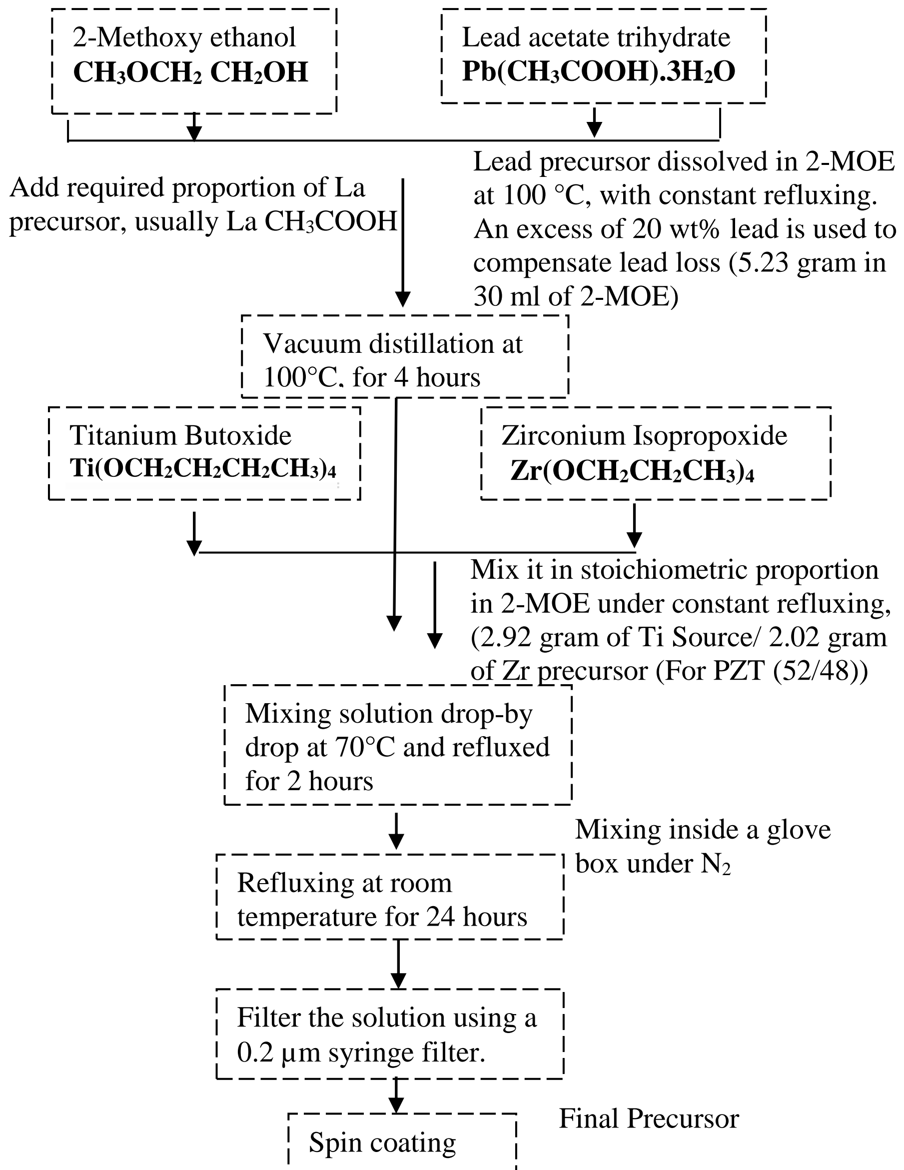

Figure 2.2: Flow chart of PZT/PLZT thin film deposition.

2.5 Deposition procedure – ferroelectric thin films

After the deposition, proper heat treatment is used to control the gelation of the solution into a film, as well as the pyrolysis and the crystallization of the final film. This treatment can be broken into three steps [22]. The first step is the drying of the film. This is usually accomplished on a hot plate at temperatures ranging from 100°C to 200°C depending on the composition of the film.

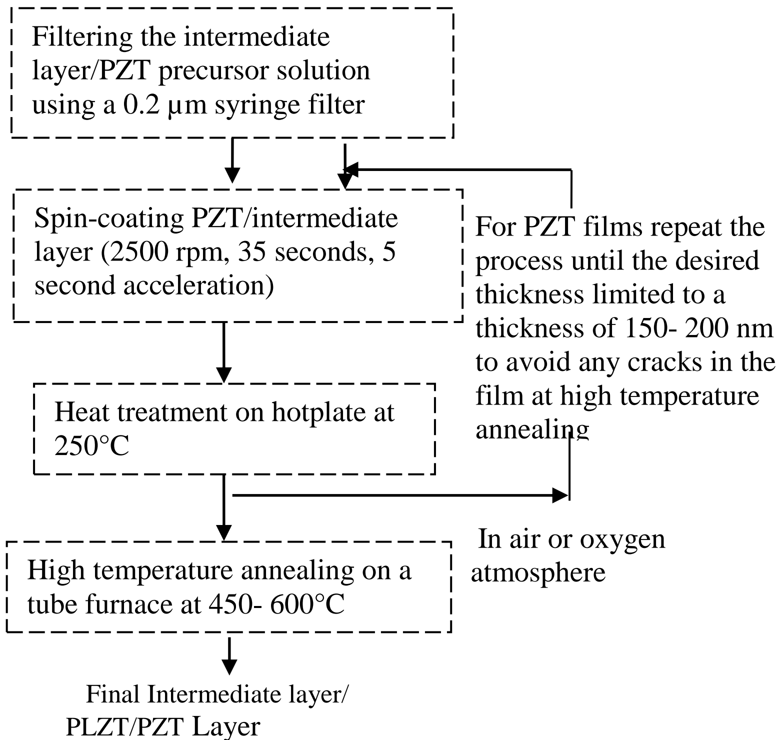

Figure 2.3: Deposition procedure: ferroelectric thin films.

During this stage, the excess solvent is eliminated and the film shrinks and densifies as it loses liquid. After drying, the film is much denser and any remaining liquid is held in by capillary action.

The next heating step removes the organic compounds. This is called pyrolysis and is referred to as the "firing" stage. The temperature for firing of the PZT film can be as high as 400°C to 500°C. During this step, the liquid remaining after the drying stage is eliminated, some organics are evaporated

and the remaining organic compounds are decomposed to form gases such as H_2O and CO_2. After this step, the film is composed of amorphous inorganic oxides. Since the properties of PZT are a consequence of its crystallographic structure, a third heating sequence at a higher temperature is necessary to crystallize the PZT. This step is often referred to as the "annealing" of the film and can be performed either in a tube furnace or a rapid thermal processor (RTP). Of these, the pyrochlore phase produced at low temperature is not ferroelectric and therefore undesirable. The ferroelectric phase has a perovskite structure and the degree of transformation to this phase is of interest.

The deposition procedure for the intermediate layers and PZT/PLZT films are given in Figure 2.3. Firstly, the intermediate layers are spin-coated onto the substrate at 2500 rpm for 35 seconds and heat treated on a hot plate at 250°C for 2 minutes. Subsequently, the layers are annealed at 400°C to 500°C in a tube furnace. Upon annealing the films undergo a sequence of endothermic weight loss reactions to initiate the intermediate phase transformation [20]. As the molarity of the precursor solution for the intermediate layer is increased, it is noticed that the non-uniformity of the spin-coated layers also increases. To avoid this problem, we have followed a multilayer spin-coating and annealing procedure. Each individual layer is spin coated and subsequently annealed in air and this process is repeated over several cycles to achieve a desired thickness. Intermediate layers of 5 to 80 nm have been prepared with this procedure. Secondly, the PZT precursor solution is spin-coated onto the intermediate layer, at 2500 rpm for 35 seconds, followed by pyrolysis at 250°C to burn out the organic components. Each spin coating and pyrolysis step results in a layer of about 50 nm, so the process cycle is repeated 4 times to obtain a film of thickness 200 nm, prior to the annealing process. If the thickness of the films are above 200 nm for annealing, the thermal stress introduces cracks in the PZT film. Subsequently, the amorphous PZT thin films are annealed in a tube furnace at 500°C to 650°C, under flowing O_2 gas or air at atmospheric pressure, for 10 to 20 minutes, to allow crystallization into the perovskite PZT phase. While annealing in oxygen steady oxygen flow of 5 liter/hour is maintained throughout the annealing procedure. The ramping rates for heating and cooling of the specimen in the annealing system are 100°C/min and −50°C/min, respectively. This process is repeated till a desired thickness of the PZT film is achieved.

2.6 Structural characterization

PZT thin films deposited by the CSD process are structurally analysed in detail. The crystallinity, texture, roughness and the growth mechanisms are studied with X-ray diffraction, X-ray pole figure, AFM, SEM and TEM.

2.6.1 Texture analysis- X-ray pole figure measurement

To analyse the mechanism of thin film growth, thicker La-intermediate layers (~ 60 nm) are formed by repeating the spin coating and heat treatment procedure, without deposition of PZT on top. The thickness of the intermediate layer (molarity of the solution- 0.03M) is calculated from ellipsometer measurements as 10.17±0.012 nm, upon single spin-coating and heat treatment procedure. The AFM measurement show an rms roughness of 1.3 nm for the intermediate layer (Figure 2.4). It is found that upon heat treatment at 500°C, the intermediate nitrate layer reacts with the CO_2 present in the ambient air, resulting in the formation of tetragonal $La_2O_2CO_3$ (a = 4.07 Å, c = 13.49 Å). The carbonate formation is also noted for other Ln-based intermediate layers.

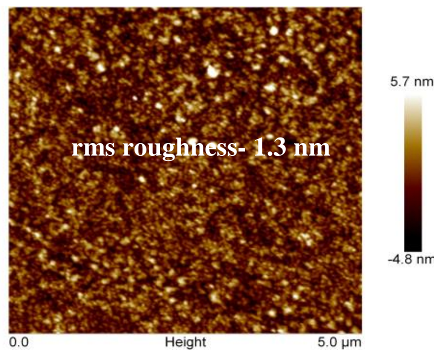

Figure 2.4: AFM image of a La-based intermediate layer of thickness 10 nm and heat treated at 500°C

The XRD patterns shown in Figure 2.5 indicate that the intermediate layers have a strong preferential growth with the c-axis perpendicular to the substrate, showing a good lattice match (mismatch in the a-axis parameters < 0.7%) to PZT. In this work, we refer to the (100) direction as the direction for which the c-axis of the tetragonal phase is perpendicular to the substrate. This convention is often used in other works although the convention to use (001) is followed in many other works. The formation of $La_2O_2CO_3$ is

further confirmed upon recording the XRD at a tilt angle of ~ 48°, bringing the (103) plane into diffraction (Figure 2.5).

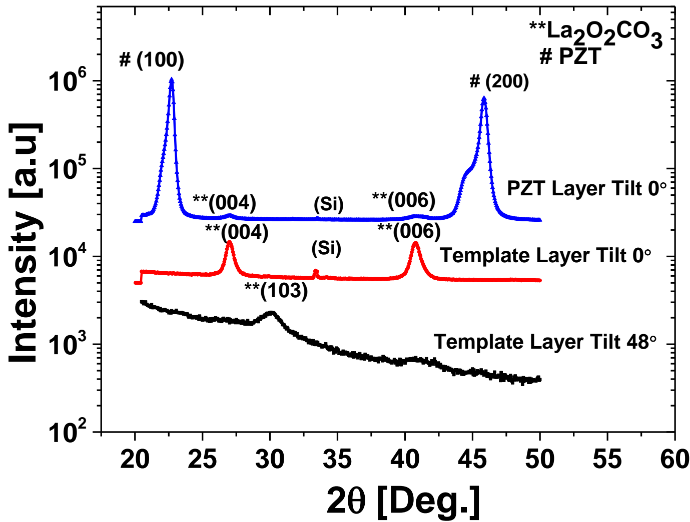

Figure 2.5: XRD measurement of the La-based intermediate layer (thickness ~ 80 nm) at different tilt angles and the PZT layer deposited on the intermediate layer.

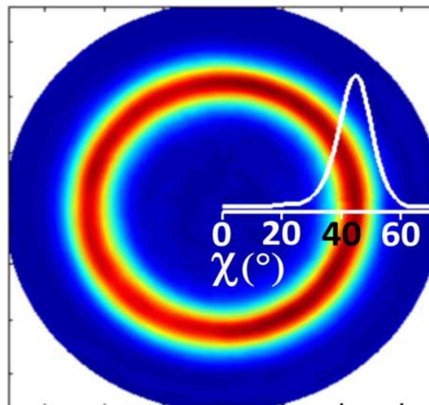

Figure 2.6: X-ray pole figure measurement of the PZT films (annealed at 630°C, thickness ~ 300 nm) deposited on a La-based intermediate layer of 80 nm.

The $Sm_2O_2CO_3$ (a = 3.974 Å, c = 12.92 Å), $Nd_2O_2CO_3$ (a = 3.98 Å, c = 15.605 Å), $Pr_2O_2CO_3$ (a = 4.01 Å, c = 15.68 Å) also demonstrate a preferential out-of-plane orientation and good lattice match with PZT (mismatch <1%). However, it is to be noted that during the carbonate formation different intermediate layers occur at different temperatures [21, 22]. When annealing the intermediate layers in pure oxygen at low pressure, no distinct diffraction peaks are found, confirming that the formation of the carbonate compound plays a key role in the strong preferential orientation of the PZT (52/48) thin film. The conclusions derived from X-ray diffraction are consistent with the microscopic behaviour of the intermediate layer, as studied with STEM and HRTEM (Figure 2.16).

2.6.2 X-ray diffraction measurements-PZT thin films

The samples are first cleaned with acetone, isopropanol and de-ionized water. The measurements are carried out with a D8 Discover diffractometer (Bruker technologies Ltd.,) with CuKα radiation. The diffractograms are recorded for 2θ angles between 15° and 64°, with step size 0.004° and time step 1.2 seconds.

2.6.2.1 PZT deposition on SiO_2, ITO and $PbTiO_3$ Intermediate layers

Even though the PZT material is known for more than a few decades, the direct deposition of PZT films on Si still remains a challenge. A large lattice mismatch and a difference in thermal expansion coefficient makes it difficult to grow such films directly on Si substrates. An efficient intermediate layer is essential to grow the films on Si and SiO_2. Over the years, intense research was carried out to find efficient intermediate layers for ferroelectric thin film growth. A large number of metallic and dielectric intermediate layers have been reported [23],[9],[23, 24],[25],[26]. The intermediate layer is necessary to prevent elemental inter-diffusion and reactions at the interface while high temperature annealing.

It is reported that ultra-thin thermally grown SiO_2 can be used as an intermediate layer for PZT (deposited by pulsed laser deposition), even though no details of the inter-diffusion and reactions at the interfaces are provided [27]. The resulting PZT films were highly (100) oriented on SiO_2 intermediate layers of thickness range between 4 and 10 nm. It is assumed that for SiO_2 thickness less than 10 nm, many small crystallites of SiO_2 epitaxially formed at the interface of amorphous SiO_2 and Si wafer, which

results in an oriented thin film growth. However, as the thickness of the oxide layer is above 10 nm, the surface state of the SiO_2 is dominated by amorphous state that results in randomly oriented PZT films. More recent experiments also showed PZT films on thicker SiO_2 intermediate layers with RF sputtering. However, this method requires a more complex deposition procedure (in terms annealing temperature, ambient, oxygen partial pressure) and produces randomly oriented PZT film [28].

As the first part of the PZT experiments, we tried to use identical SiO_2 intermediate layers of thickness less than 10 nm, as reported previously [27]. However, in our experiments we could not reproduce these results. Figure 2.7 shows the XRD patterns obtained when trying to deposit PZT films on Si and Si/SiO_2 substrates using the CSD method. It is noticed from the measurements that the CSD deposited PZT films on thermally grown ultra-thin intermediate SiO_2 layers of 5 nm and 10 nm (prepared by dry oxidation) show only pyrochlore phase formation and no XRD peaks corresponding with the PZT perovskite phase are observed. The PZT experiments were also conducted with other well-known intermediate layers such as ITO [29] and $PbTiO_3$ [30], [31].

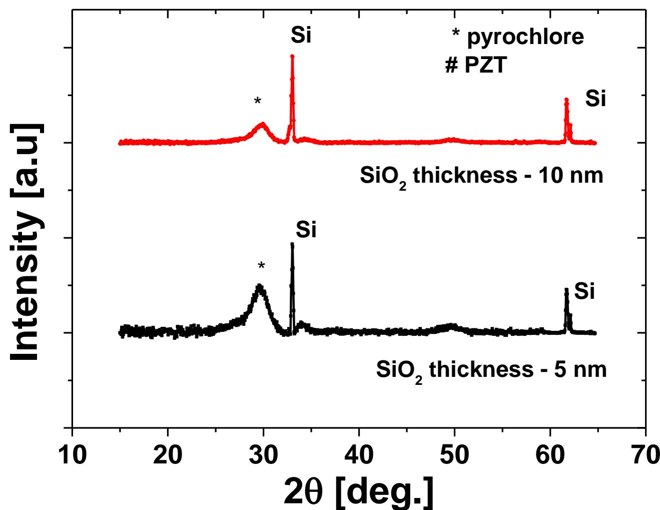

(a)

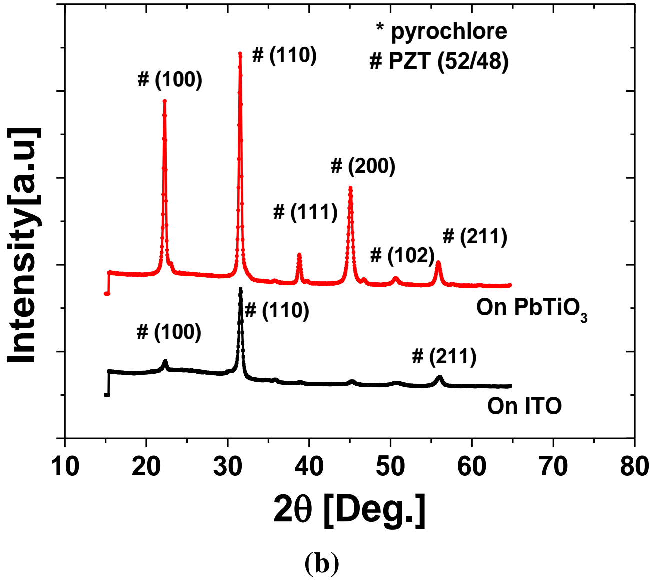

(b)

Figure 2.7: XRD patterns of PZT films annealed at 630°C, (a) thermally grown SiO_2 layers of different thickness (b) on ITO (30 nm) and $PbTiO_3$ (50 nm)

To perform these experiments on a Si substrate, ITO intermediate layers (thickness ~ 30 nm) were deposited using the e-gun evaporation technique. The experiments on glass were performed using commercial ITO (thickness ~ 15 - 30 nm)/glass substrates (Delta technologies, Inc.). The $PbTiO_3$ intermediate layers (thickness ~ 50 nm) were prepared by the CSD method, as described in section 2.4. The results of these experiments are provided in Figure 2.7(b).

The PZT films are deposited and characterized successfully on both glass and Si substrates using ITO intermediate layers and these results match well previous reports [29]. However, the experiments based on $PbTiO_3$ intermediate layers are limited to ITO/glass and Pt/Si substrates. The deposition of $PbTiO_3$ layers directly on Si is difficult due to the lead diffusion. In our experiments we could reproduce the literature results on both ITO and $PbTiO_3$ layers. It is evident from Figure 2.7 that the PZT films deposited on ITO and $PbTiO_3$ intermediate layers are randomly oriented. The XRD patterns show the complete crystallization of the PZT films in to a

perovskite phase over the ITO and $PbTiO_3$ intermediate layers, with no diffraction peaks corresponds to the pyrochlore phase. The PZT films are randomly oriented with mixed (100), (110), (111), (200), (211), (102) crystallographic orientation. The X-ray pole figure analysis confirms that the film deposited by this method shows no specific in-plane texture. Even though we could successfully grow PZT films on Si using ITO intermediate layers, the high absorption of ITO at telecommunication wavelength (~ 1550 nm) is a drawback to use it for optical devices Moreover, it is also reported that the pockels coefficient of the randomly oriented PZT layers on ITO is much smaller than the highly oriented PZT layers grown on MgO [32] and $SrTiO_3$ [33] intermediate layers. The state-of-the-art deposition of ferroelectric thin films on Si for optical devices is limited to MBE grown epitaxial thin films [34].

2.6.2.2 PZT deposition on lanthanide (Ln) based intermediate layers

Figure 2.8 shows the highly textured PZT thin film growth (annealed at 600°C) on silicon substrates under optimal heat treatment of the intermediate layer. The diffractograms show strong diffraction peaks along the (100) and (200) crystallographic orientations at 2θ = 22º.

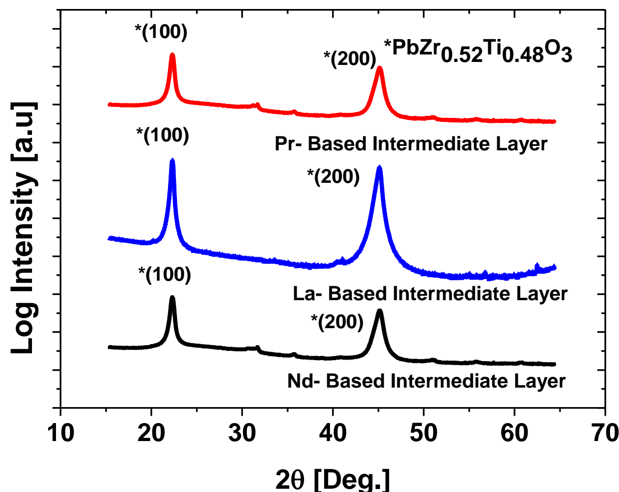

Figure 2.8: XRD pattern of the PZT thin films (annealed at 600°C), on intermediate layers of La, Pr and Nd, which are heat treated at 500°C, 450°C and 440°C, respectively.

Thickness of all PZT layers are identical for the XRD measurements and it is determined by spectroscopic ellipsometry measurements as 200 ± 3 nm. The thickness of the intermediate layer is approximately 10 nm. The intermediate layers presented in this experiment on La, Pr and Nd are heat treated at 500 °C, 450°C and 440°C respectively, before the PZT deposition and annealing. Regardless of the PZT processing conditions such as pyrolysis temperature, pyrolysis time or annealing time, the PZT films deposited onto these intermediate layers are crystallized into a pure perovskite phase, with no evidence of any intermediate secondary phase formation. The detailed analysis of the buffer layers under the above deposition conditions presented in section 2.6.1.

2.6.2.3 Effect of buffer layer treatments

Figure 2.9(a) and Figure 2.9(b) represent the XRD patterns of the PZT films (annealed at 630 ºC) deposited on Nd and La-based intermediate layers, which are heat treated at different temperatures. It is evident that the Nd-based intermediate layers that are heat treated at 350°C and 650°C show a mixed (100) and (110) orientation, whereas the intermediate layer heat treated at 440°C results in a strong (100) preferential orientation.

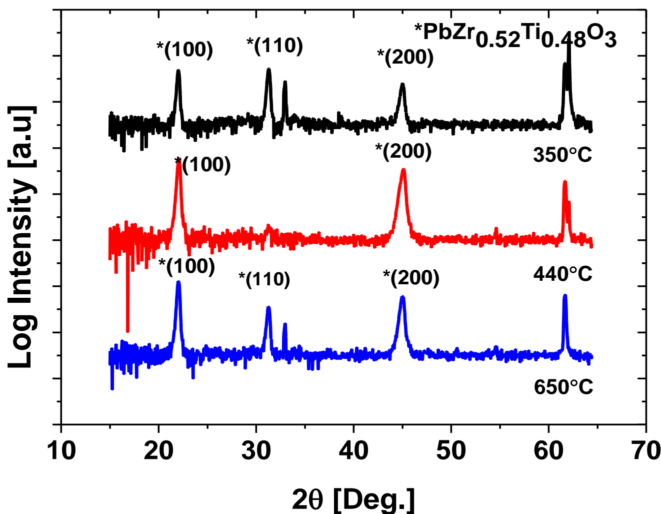

(a)

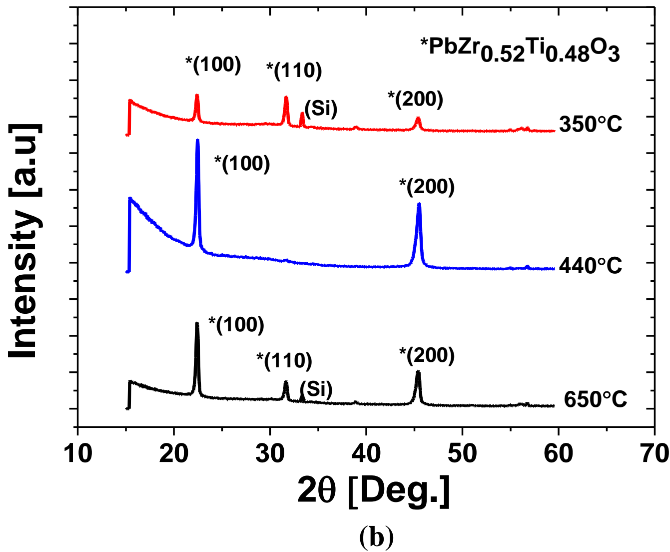

(b)

Figure 2.9: XRD patterns of the PZT films on silicon substrates annealed at 630 °C (a) On Nd and (b) La based intermediate layers of 10 nm, which has been heat treated at different temperatures.

The heat treatment of the intermediate layer influences the nucleation mechanism, which results in different diffraction peaks in the XRD spectrum. It has been reported that heat treatment initiates the transformation of the nitrate film into different crystalline states of $NdO_{0.5}NO_2$, $NdONO_3$ and Nd_2O_3 at 350°C, 440°C and 650°C, respectively. Even though many crystalline phases exist depending on the thermal decomposition of $Nd(NO_3)_3.6H_2O$, we found that the intermediate phase obtained after a heat treatment around 440ºC is the only one resulting in oriented thin film growth., It is noticed that upon heat treatment at 440ºC, the intermediate nitrate layer reacts with the CO_2 present in the ambient air, resulting in the formation of tetragonal $Nd_2O_2CO_3$, which show a strong preferential orientation. The measurements on the intermediate layers are analysed in detail in section 2.6.1._

Figure 2.9(b) represents the XRD patterns of the PZT thin films deposited on a La-based intermediate layer. The intermediate layers are subjected to different heat treatments prior to the PZT thin film deposition and finally

annealed at 630ºC. It is evident that the heat treatment of the intermediate layers plays a crucial role in determining the crystal orientation of the subsequently deposited PZT film. The results obtained here are similar to the x-ray diffraction patterns for the Nd-based intermediate layers (Figure 2.9(a)). As the annealing temperature of the intermediate layer goes above 650 ºC, mixed (100) and (110) orientations are observed. This is due to the possible conversion of the $La_2O_2CO_3$ to La_2O_3. Furthermore, during the heat treatment LnO_2CO_3 is formed rather than the mixed Ln(O,N) compounds, as will be motivated below [35],[36],[37].

2.6.2.4 Effect of intermediate layer thickness

Figure 2.10 shows the X-ray diffractograms of the PZT thin films (annealed at 600°C) deposited on Si substrates coated with a La-based intermediate layer (heat treated at 500°C) of different thicknesses. When the intermediate layer thickness is only 3 nm, the intermediate layers are not efficient to prevent the inter-diffusion of Si and PZT and only the pyrochlore PZT phase is observed (not shown in Figure 2.10).

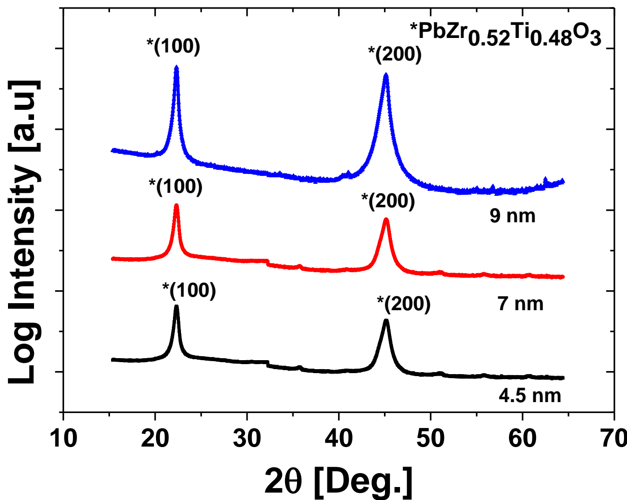

Figure 2.10: XRD patterns of the PZT films annealed at 600°C on a silicon substrate coated with La-based intermediate layers of different thickness (heat treated at 500°C).

A similar result has been reported before with PZT films on ultra-thin intermediate SiO_2 of thickness < 4 nm [27]. However, as the intermediate layer thickness increases above 4.5 nm, well-defined diffraction peaks corresponding to the stoichiometric PZT are observed along the (100) and (200) crystallographic directions, independent of the intermediate layer thickness.

As mentioned before, one of the main objectives of this work is to reduce the thickness of the intermediate layers as much as possible. Dielectric intermediate layers with smaller thickness allow for better interaction of the light with the active PZT layers for waveguide applications. Here we demonstrate one of the smallest reported intermediate layers which support PZT thin film growth on different substrates.

The non-uniformity in the layer thickness and the stress induced in the films are larger with thinner intermediate layers. Therefore, it is necessary to mention that reducing the thickness further down to less than 5 nm, results in micro-cracks in the films. With a thickness as low as 7 nm we observe dense films without any cracks. Table 2.1 compares our work with other reported results.

Table 2.1: Comparison of different oxide based intermediate layers and thickness used for state-of-the-art PZT thin film growth

Substrate	**Intermediate Layer**	**Thickness (nm)**	**Advantage or Limitation**
Si	SiO_2 [27]	4-10 nm [27]	Only possible on Si Substrates
Si, Si_3N_4, SiO_2, ..etc	**LnO_2CO_3** [38]	5-20 (Our Work)	Possible on number of different substrates
Si	TiO_2 [39]	20- 100	Possible on different substrates
Glass	$PbTiO_3$ [40]	75	On glass

Substrate	Intermediate Layer	Thickness (nm)	Advantage or Limitation
Si, Glass	ITO [41]	30	Highly absorbing at λ~ 1550 nm
Si	$YSZ/CeO_2/LSCO$ [42]	5/15/15	On Si
Si	SiO_2 [28]	300	Proven only on Si
Si	MgO [43]	100	Only on Si

2.6.2.5 Deposition on non-planar substrates

Even though we successfully demonstrated PZT thin film growth on a variety of substrates, the use of ultra-thin intermediate layers limits the thin film growth on non-planar substrates. As the step height to the intermediate layer thickness increases above 4, conformity issues related with the spin coating of the intermediate layers play a significant role in determining the quality of the PZT films [3]. The non-uniformity in the spin coated layers leads to an exposure of the corners of the substrate's structures to the PZT solution. As the thickness of the intermediate layers decreases the corners of the non-planar structures get more exposed compared to other regions. We noticed that cracks started appearing at the corners as the intermediate layer thickness falls below a certain critical thickness. The subsequent high temperature annealing of the PZT films results in micro-cracks and unwanted intermediate phases in the PZT films. It degrades the quality of the film and introduces a large leakage current. In order to avoid this problem, for a given structure either the step size needs to be reduced or the intermediate layer thickness needs to be increased.

Increasing the intermediate layer thickness is a rather tedious process. The spin coating and annealing process (each layer of 10 nm) has to be repeated many times to achieve a desired thickness. Therefore we use a planarized

substrate or structures with step height less than 40 to 60nm for intermediate layers of thickness of 10 to 15 nm. Figure 2.11 shows the issues associated with the conformity of spin coating. We conducted the experiments on non-planar substrates using a Si-slot waveguide with a step height of 220 nm and Si-Rib waveguide of step height 70 nm, prepared at imec with a 193 nm deep UV lithography process [44].

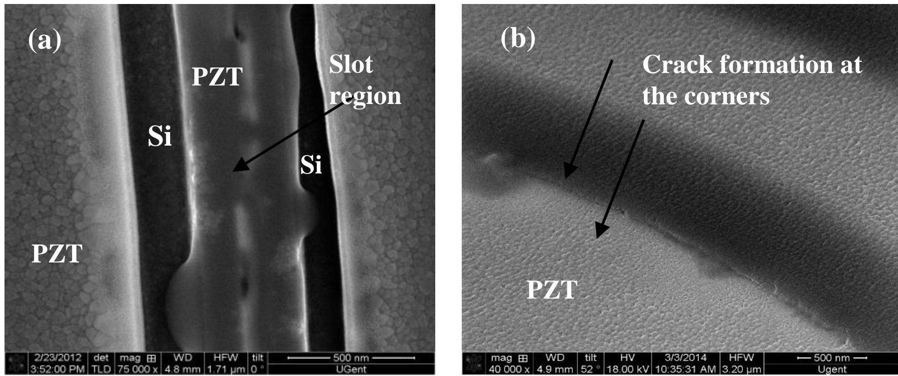

Figure 2.11: SEM top view image of the PZT films (annealed at 630°C) over a La-based intermediate layer of 15 nm, deposited (a) on a Si-slot waveguide of step height ~ 120 nm (b) on a Si-rib waveguide of step height ~ 70 nm.

Figure 2.11(a) show the top-view of the Si-slot waveguide with a PZT layer on top. The slot waveguide is formed with two Si regions (width ~ 200 nm) separated by a small slot region of width of 150 nm and 220 nm step height on either side formed by reactive ion etching. From the SEM images it is very clear that large step height to the intermediate layer thickness results in non-uniformity in the spin- coated layers. Even though the PZT films appear to be uniform with well packed PZT grains, it is noted that micro-cracks are formed at the etched corners of Si after the annealing process due to the non-uniformity in the intermediate layer coating (see Figure 2.11(b)). However, as the step height decreases to < 60 nm, the films are uniform without any cracks.

2.6.2.6 Influence of annealing temperature

It is well known that the orientation of a PZT film on a platinized silicon substrate depends strongly on the thermal treatment conditions, due to the resultant change in the nucleation mechanism. This affects the formation of transient phases such as PbO, the PbPt intermetallic phase and pyrochlore.

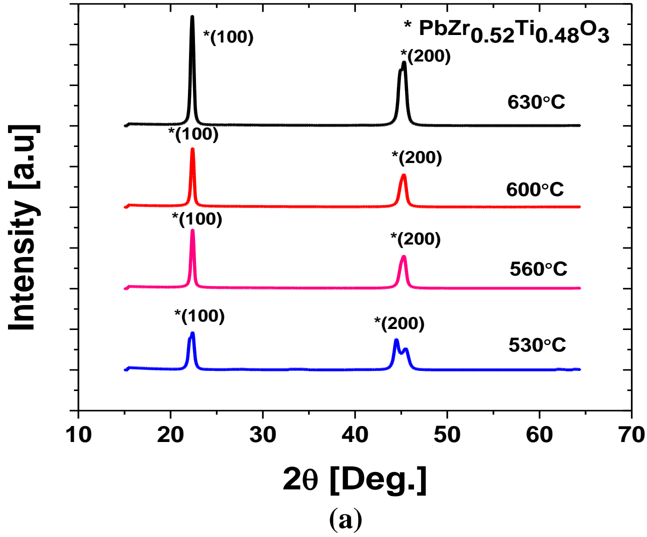

(a)

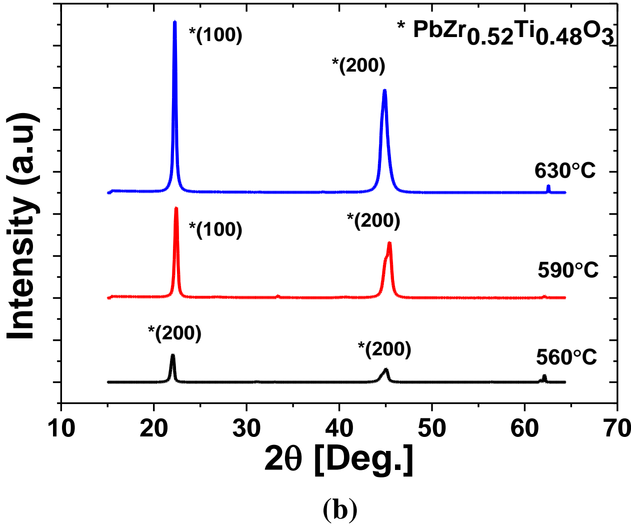

(b)

Figure 2.12: XRD pattern of the PZT film deposited on Si substrate coated with (a) La-based intermediate layer (heat treated at 500°C) (b) on Pr-based intermediate layer (475°C) of thickness 10 nm and annealed at different temperatures

The PZT films coated on a $La_2O_2CO_3$ intermediate layer showed only (100) orientation, regardless of the heating conditions, which means that there is only one kind of nucleation mechanism in operation, governing the orientation of the PZT film. Figure 2.12(a) and Figure 2.12(b) represent PZT films deposited on intermediate layers of La and Pr, respectively and annealed at different temperatures.

Figure 2.12(a) shows the XRD patterns of the PZT films annealed at different temperatures on a glass substrate coated with a La-based intermediate layer (heat treated at 500ºC). It is evident from the measurements that regardless the annealing temperature PZT films deposited on the $La_2O_2CO_3$ intermediate layers are crystallized into a perovskite phase with (100) crystallographic orientation (>99.8%). The presence of the $La_2O_2CO_3$ intermediate layer reduces the nucleation energy for the PZT films to grow along the (100) crystallographic orientation. It allows the crystallization of the films even at a significantly lower temperature down to 530ºC. It allows the crystallization of the films even at a significantly lower temperature down to 530ºC. The films annealed 530ºC show identical crystallization properties with strong preferential orientation (with the (100) orientation ~ 99%), with a decreased diffraction intensity.

Figure 2.12(b) shows the X-ray diffraction patterns of the PZT films deposited on a Pr-based intermediate layer (heat treated at 450ºC) at different temperatures. The results are identical to Figure 2.12(a) with strong orientation of the PZT film along the (100) crystallographic direction. The X-ray pole figure confirms the strong (100) out-of-plane orientation of the film, with no specific in-plane texture.

2.6.2.7 Deposition on different substrates

The PZT experiments are repeated on different substrates including Si, glass, glass/ITO, Si/Al_2O_3, Si/SiO_2 and Si/Si_3N_4. The resulting XRD patterns are shown in Figure 2.13. The PZT experiments are repeated on different substrates including Si, glass, glass/ITO, Si/Al_2O_3, Si/SiO_2 and Si/Si_3N_4. The resulting XRD patterns are shown in Figure 2.13. An apparent peak shift observed for the Glass/ITO sample is due to the minor misalignment.

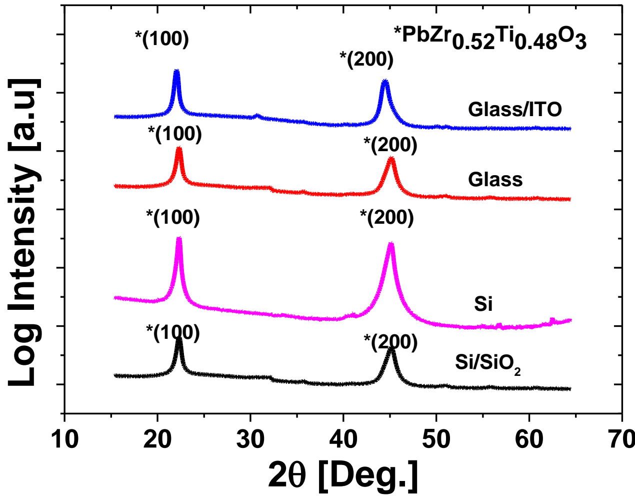

Figure 2.13: XRD patterns of PZT thin films annealed at 600°C, on different substrates coated with La-based intermediate layers (thickness ~ 10 nm, heat treated at 500ºC).

All the PZT thin films show identical crystallographic orientation and similar properties, regardless of the substrate material. This indicates that the orientation of the thin film is not influenced by the substrate and depends only on the nature of the intermediate layer. The minimum thickness of the intermediate layer determined from our experiments to avoid any micro-cracks after high temperature annealing are in the range of 7 to 15 nm

2.6.2.8 Deposition of PLZT thin films

It is known from literature that La-doped PZT films (i.e. PLZT films) exhibit a stronger pockels effect and much lower coercive field than PZT films [45].Therefore we also prepared PLZT films on Si substrates. Figure 2.14 represents the XRD patterns of the PLZT (8/65/35) films deposited on a silicon substrate with a La-based intermediate layer heat treated at different temperatures. The PLZT films were annealed at 600°C. The measurements of the PLZT films shows a strong preferential (100) orientation, very similar to the results observed for the PZT films. All the measurements carried out on PLZT films with different substrates, intermediate layer treatments and

annealing temperatures, produce identical results to that of the PZT thin films.

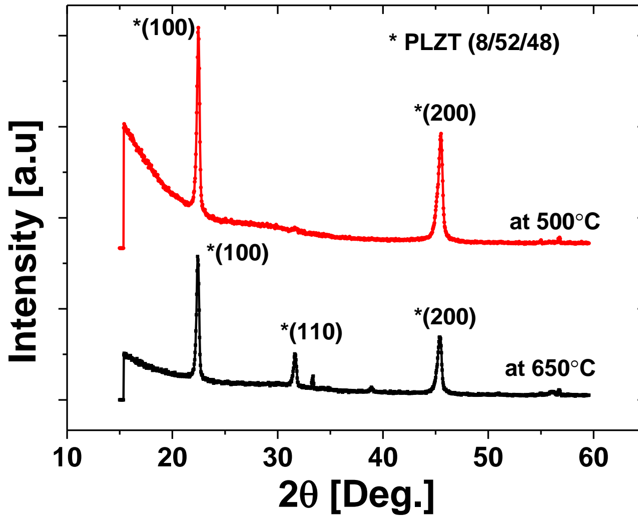

Figure 2.14: XRD pattern of the PLZT thin film annealed at 600°C on La-based intermediate layers of 10 nm, which are heat treated at different temperatures.

2.6.3 SEM analysis of PZT

The surface morphology of the films confirms smooth, dense and uniform polygonal grains without any obvious secondary phase (see Figure 2.15(a) and Figure 2.15(b)). The average grain sizes of the PZT films deposited on Si, with intermediate template layers of Nd and La are estimated as 300 nm and 80 nm respectively. When the intermediate layer thickness is below the critical thickness (intermediate layer thickness smaller than 4.5 nm), the deposited PZT films show micro cracks and pinholes on the film surface. The presence of the inter-crystal voids and micro cracks increases the leakage current during the electrical measurements. These unwanted features are due to the thermal stress in the PZT thin films generated during multiple annealing steps and the non-uniformities in the intermediate layers. The problem can be resolved by increasing the intermediate layer thickness.

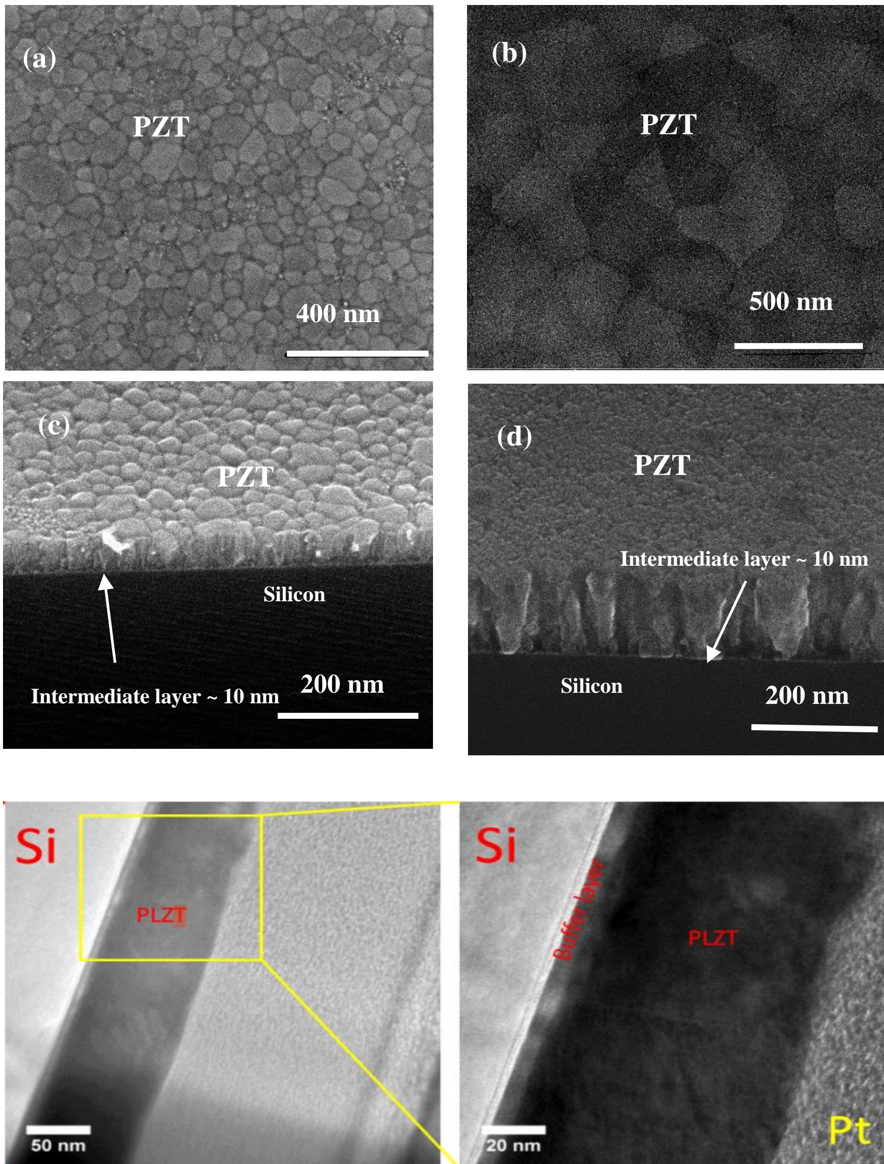

Figure 2.15: (a) SEM top view of the PZT thin film (thickness ~200 nm, annealed at 630°C) deposited on silicon substrate, coated with a Nd- based intermediate layer (thickness ~10 nm, heat treated at 440°C), (b) La- based intermediate layer (thickness ~10 nm, heat treated at 500 °C). (c) Cross-section image of PZT thin film (thickness ~200 nm) annealed at 630°C (d) annealed at 560°C, on a silicon substrate, coated with a La- based intermediate layer (thickness ~10 nm, heat treated at 500°C). (e), (f) TEM cross-section view of PLZT films deposited on La-based intermediate layer (heat treated at 500°C) and annealed at 600°C.

The cross sectional SEM images of the PZT shown in Figure 2.15(c) and Figure 2.15(d) exhibit dense columnar grains. The FIB cross-sections of the PLZT films in Figure 2.15(e) and Figure 2.15(f) confirm the presence of the ultra-thin intermediate layers. This growth behaviour can also be observed in the STEM imaging of a cross section (Figure 2.16). Micrometer sized secondary phases like pyrochlore/fluorite phases are not observed in the SEM images [17]. These observations are also confirmed by the lack of corresponding diffraction peaks and by the well-defined electrical measurements. Also the presence of the thin intermediate layer is evident from the SEM measurement and the thickness matches with the data from ellipsometry measurements.

2.6.4 TEM analysis of PZT

Transmission electron microscopy (TEM) analysis is performed using a JEM-2200FS FEG-TEM (Jeol), operated at 200 keV and equipped with an in-column omega filter to reduce chromatic aberration. Energy dispersive x-ray (EDX) spectroscopy was used to measure the chemical composition in scanning TEM mode (STEM).The conclusions derived from x-ray diffraction are consistent with the microscopic behaviour of the intermediate layer, as studied with STEM and HRTEM (Figure 2.16(b)).

Based on the STEM image, it is clear that the $La_2O_2CO_3$ layer acts as an efficient intermediate layer between the Si substrate and the PZT layer. Also, the brightness variations in the PZT layer suggest the onset of the growth of columnar grains. A line scan by means of EDX was recorded to study the chemical composition of the intermediate layer. The $La_2O_2CO_3$ thin film indeed acts as an efficient intermediate layer between the substrate and the PZT thin film (Figure 2.16(a)), since the compositional gradient for the representative elements Si, La and Pb is steep, taking into account the typical spatial resolution of EDX in STEM. The HRTEM image (Figure 2.16(b)) confirms the crystalline nature of the intermediate layer. In addition, the c-axis is found to be perpendicular to the interface between the PZT and intermediate layer, in line with the texture analysis (Figure 2.6). Furthermore, the PZT layer is well crystallized, starting at the interface with the intermediate layer. Again, the crystallographic orientation, as observed from the FFT power spectrum, is in line with the x-ray diffraction measurements. The (110) planes of PZT are perpendicular to the interface and parallel to the incident electron beam. Consequently, there is epitaxial

growth in the observed region between the $La_2O_2CO_3$ intermediate layer and the PZT thin film.

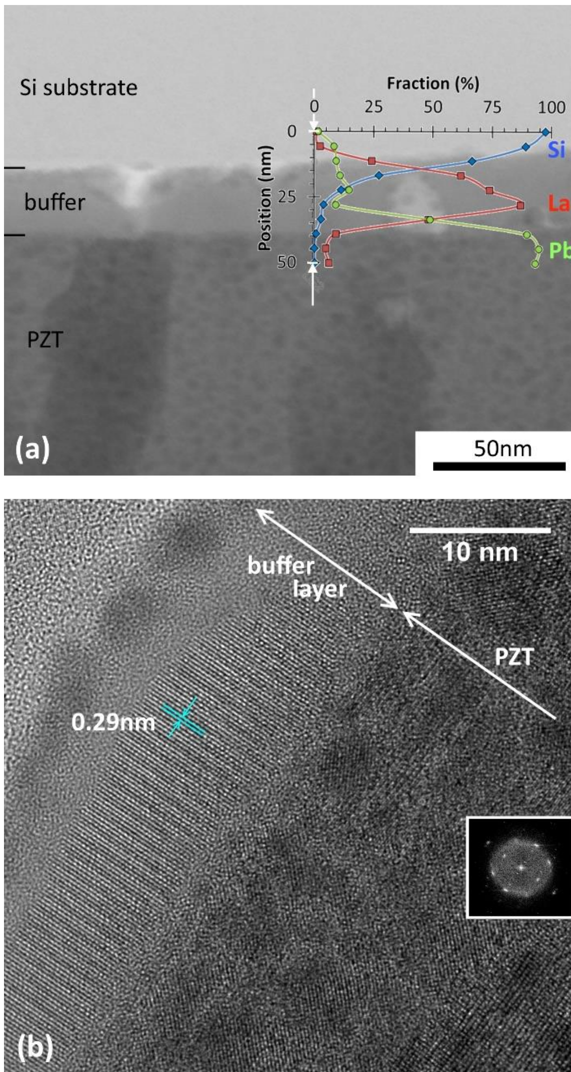

Figure 2.16: (a) STEM image of the cross section of the PZT thin film (annealed at 630°C) on top of the $La_2O_2CO_3$ intermediate layer (heat treated at 500°C). The overlay shows the relative EDX signal intensity measured along the line marked by the two white arrows. For these intensities, only the elements La, Pb and Si were taken into account. (b) HRTEM image of the same cross-section, with indication of the (110) plane spacing in $La_2O_2CO_3$. The inset shows the FFT power spectrum for the PZT layer.

2.6.5 AFM analysis of PZT

Atomic force microscopy (AFM) measurements are carried out to estimate the root mean square (rms) roughness of the PZT films. A 5µm by 5µm square area is taken into consideration for measuring the rms roughness value. The tip width of AFM used in our measurement is between 3 and 5 nm. The measured rms value for the roughness on La, Nd, Pr and Sm based intermediate layers are 2.4 nm, 2.2 nm, 2.8 nm and 2.6 nm respectively.

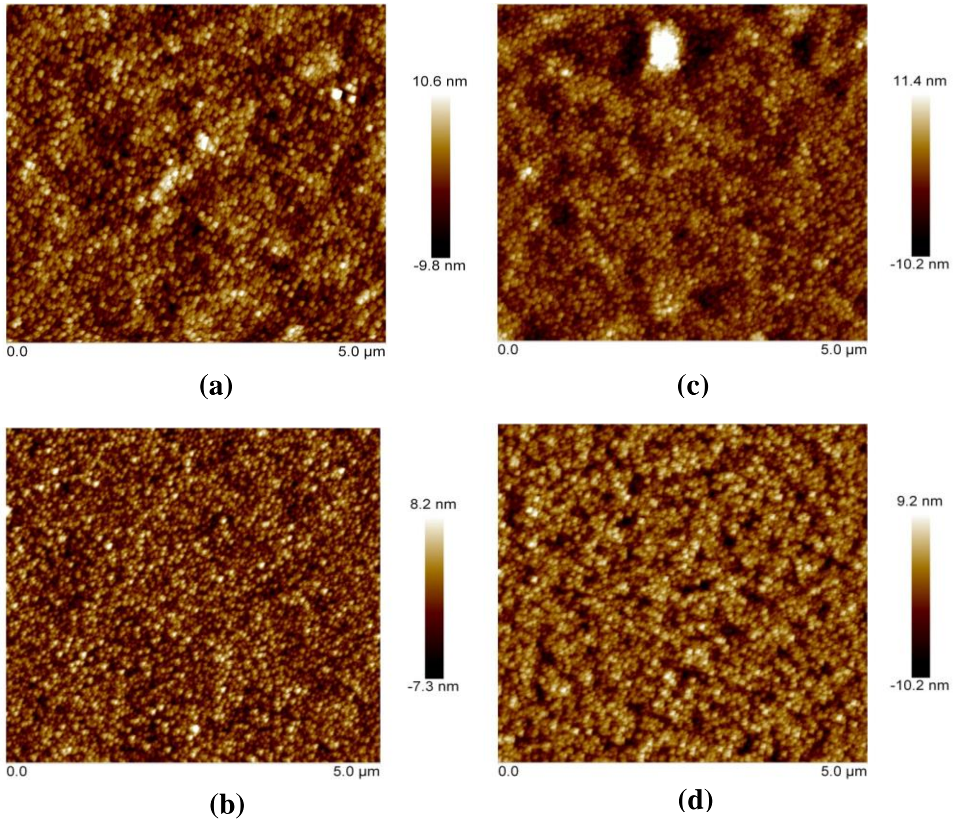

Figure 2.17: AFM images of the PZT films deposited on Si substrates and annealed at 630˚C on (a) Nd (b) Sm (c) La (d) La-based intermediate layers.

2.7 $BaTiO_3$ and $BaZrTiO_3$ thin film preparation and deposition

The preparation of the $BaTiO_3$/$Ba(Zr,Ti)O_3$precursor solution is shown in Figure 2.18.

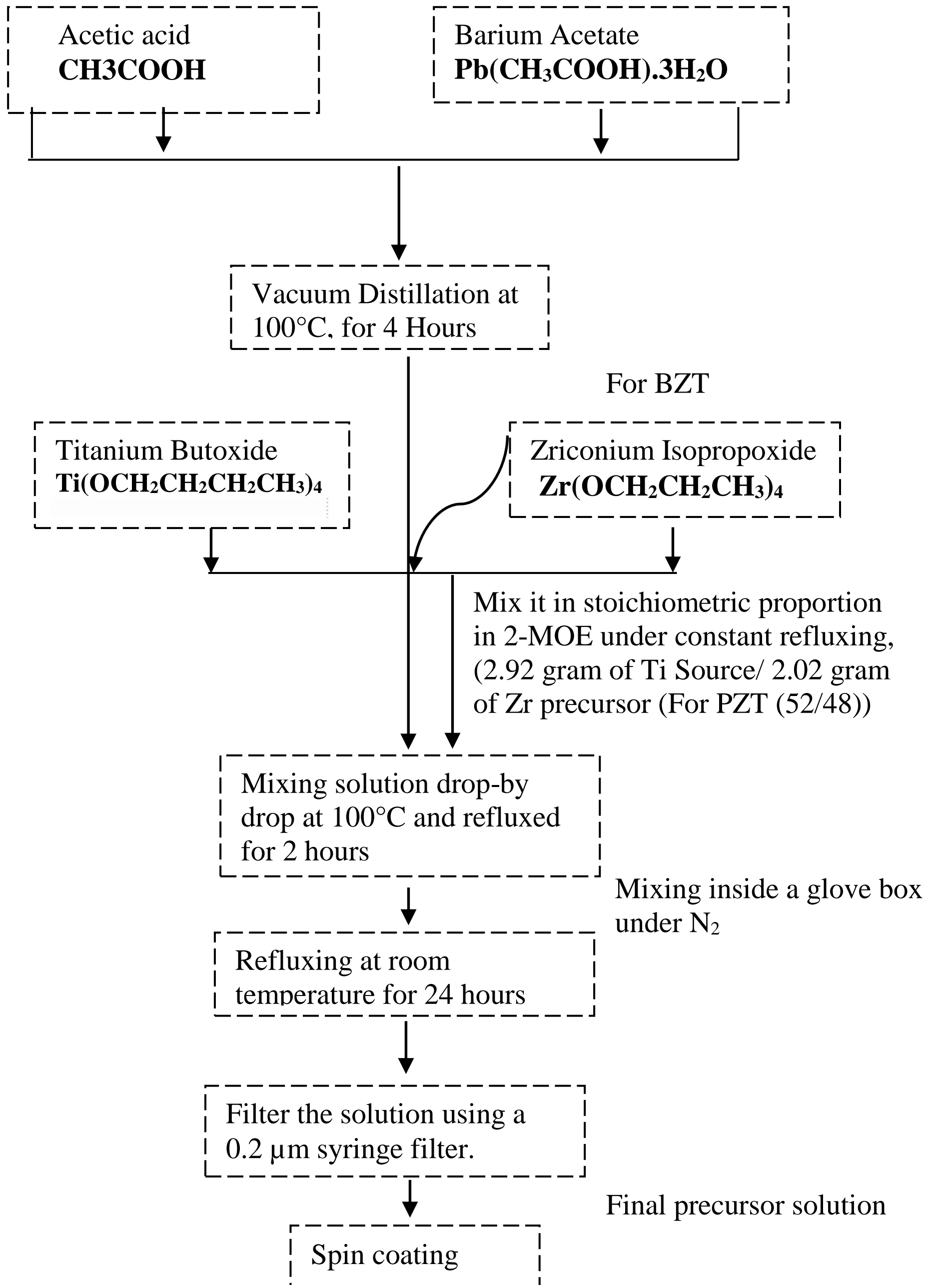

Figure 2.18: Flow chart representing the $BaTiO_3$/ $Ba(Zr,Ti)O_3$ preparation

$BaTiO_3$ and $Ba(Zr,Ti)O_3$ thin films are prepared and tested as an alternative to the Pb based ferroelectric thin films. Reagent grade barium acetate $Ba(CH_3COO)_2$ and titanium butoxide $Ti(C_4H_9O)_4$ are used as source materials for barium and titanium and glacial acetic acid and 2 –methoxy ethanol are used as the solvents. The molarity of the solution is 0.25M. For the deposition of the BTO films we followed the standard deposition procedure for the ferroelectric thin films as described in section 2.5. The BTO precursor sol is spin coated at 3500 rpm for 45 seconds, followed by pyrolysis on a hot stage at 350 °C to burn out the organic components. This leads to a film thickness of about 30 nm. This process is repeated 3 or 4 times to obtain a film thickness around 100 nm.

Then the silicon substrate with the BTO amorphous film is subjected to a high temperature annealing at 600°C - 750°C for 20 minutes, with a tube annealing furnace in ambient air. The annealing temperature for the BTO films is rather high and it is similar to previously reported results. The ramping rates for heating and cooling of the specimen in the annealing system are 100°C/min and -50°C/min respectively. The process cycle (2 or 3 spin coatings and subsequent high temperature treatment) is repeated several times to obtain an oriented thin film with thickness of a few 100 nm.

2.8 X-ray diffraction measurements-$BaTiO_3$ thin films

Figure 2.19(a) shows different x-ray diffractograms of $BaTiO_3$ thin films deposited on bare silicon substrates and subjected to an annealing treatment at 600°C or 700°C. The thickness of the BTO films is determined as 150 ± 3 nm from ellipsometer measurements.

It is evident from Figure 2.19 (a) that a minimum thickness of the intermediate layer is necessary to prevent silicate formation at the Si- BTO interface and to promote crystal growth. Figure 2.19(a) represents a comparison between the BTO thin films deposited on silicon (annealed at 700°C) with different thicknesses of the intermediate layer. When the intermediate layer thickness is 4.4 nm, the secondary fresnoite phases ($Ba_2TiSi_2O_8$) are dominant and only few diffraction peaks correspond to crystalline BTO. However, it is found from our experiments that a slightly thicker intermediate layer of 7 nm is sufficient to yield well defined diffraction peaks corresponding to stoichiometric BTO ($BaTiO_3$), with a mixed (100) and (111) orientation. Any further increase in the intermediate layer thickness leads to a stronger diffraction intensity along the (100)

orientation. The XRD measurements indicate that the films are crystallized into a pure perovskite phase, with a tetragonal geometry.

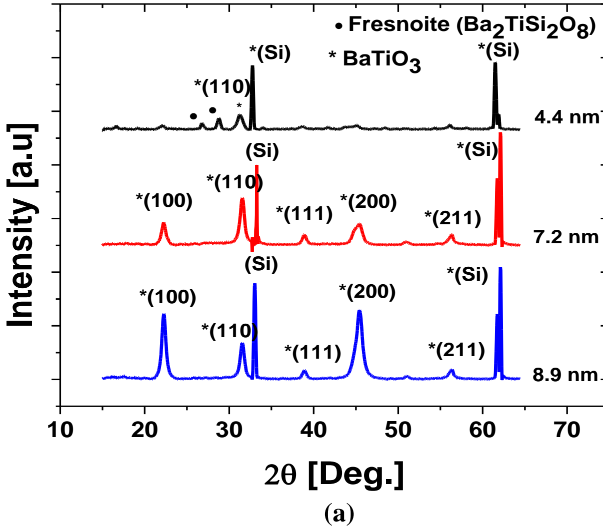

(a)

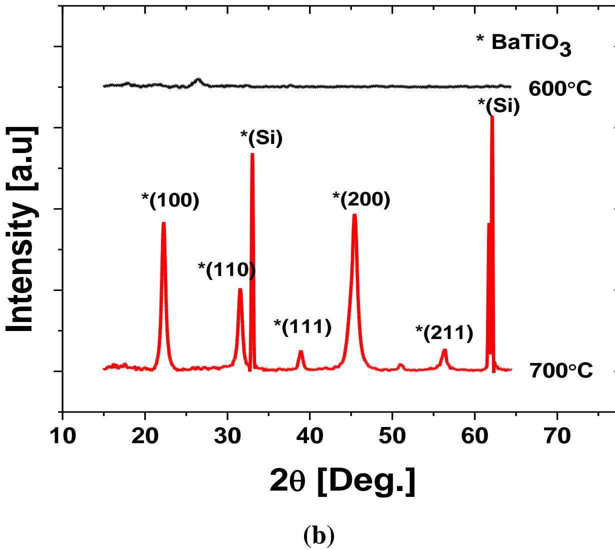

(b)

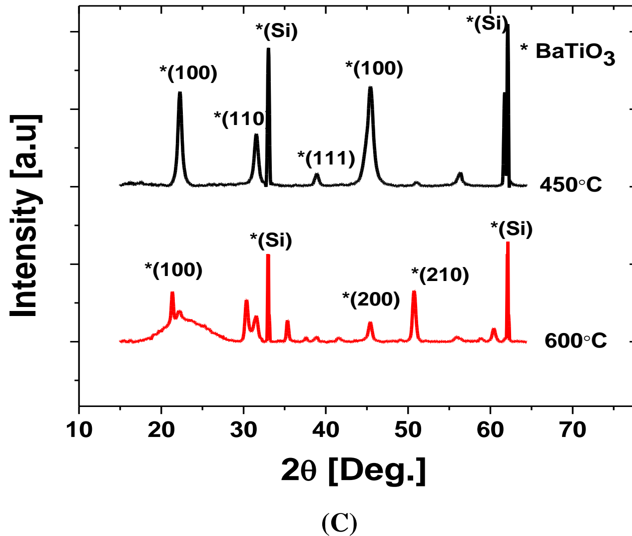

(C)

Figure 2.19: XRD patterns obtained for the BTO thin films: (a) BTO annealed at 700°C, with intermediate layers of different thickness (b) BTO annealed at different temperatures, with a 8.9 nm intermediate layer (c) BTO annealed at 700°C, with a 8.9 nm intermediate layer, heat treated at 450°C and 600°C

It is evident from Figure 2.19(b) that no diffraction peaks are observed for the samples (buffer layer thickness 8.9 nm) annealed at 600 °C, whereas it shows well defined peaks for films annealed at 700 °C. The films annealed at 600 °C do not show any diffraction peaks of fresnoite or BTO, indicating the amorphous nature of the film. The absence of the fresnoite silicate phases also indicates that no reaction happened at the BTO/buffer layer interface due to the interdiffusion of Si.

Figure 2.19(c) shows the XRD patterns of BTO thin films (annealed at 700 °C) deposited on 8.9 nm thick buffer layers, that are heat treated at 450 °C or 600 °C. It is obvious from the measurements that crystallization of the BTO films is influenced by the heat treatment of the buffer layer. The heat treatment influences the nucleation mechanism of the BTO film and results in different diffraction peaks in the XRD spectrum.

Crystal orientation of the BTO thin film: The dielectric, piezoelectric and electro optic properties of the thin films depend strongly on the crystal

orientation. Highly c-axis oriented BTO thin films reported in literature are grown on either a single crystalline oxide substrate or with a preferentially oriented thick (>100nm) conductive or dielectric intermediate layer [46, 47]. The results shown in Figure 2.20 indicate that we can grow good highly c-axis textured BTO films with $La_2O_2CO_3$ intermediate layers, (keeping the intermediate layer thickness as 8.9 nm) by adding the number of annealing steps.

Table 2.2 represent a comparison between the state-of-art deposition techniques used to grow BTO thin films on various substrates using different types of intermediate layers. It is to be noted that most of the deposition methods uses on a highly oriented intermediate layer or a single crystalline substrate to get strongly oriented BTO thin film. The deposition of the highly oriented intermediate layers requires more sophisticated deposition techniques such as ALD, PLD and MBE. However, in our work we uses simple, low cost CSD based techniques to fabricate both intermediate layer as well as the BTO layer. Moreover, our deposition methods allows the BTO thin film growth on both amorphous (glass, glass+ITO, SiO_2, Si_3N_4) and crystalline (Si) substrates.

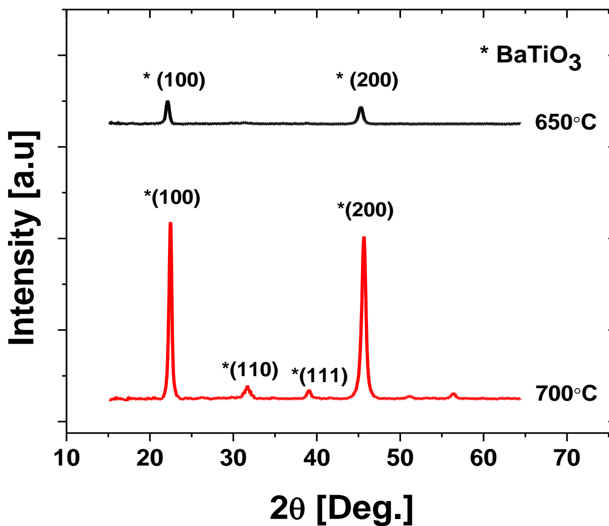

(a)

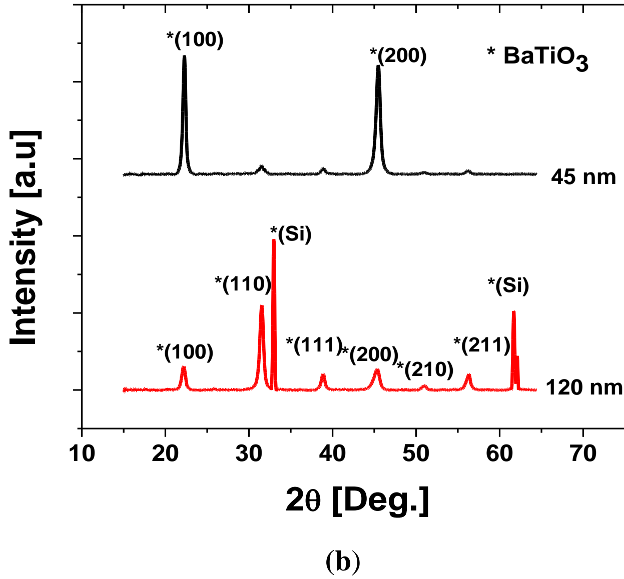

(b)

Figure 2.20: XRD patterns obtained for BTO thin films deposited on an intermediate layer of thickness 8.9 nm and a BTO seed layer of 30 nm (a) annealing after each 30 nm BTO layer deposition, at different temperatures (b) annealing at 700°C after each 30 nm BTO layer deposition, or after four 30 nm BTO depositions (120 nm).

Table 2.2: A comparison of different intermediate layers and thickness used for state-of-the-art $BaTiO_3$ thin film growth.

Substrate	Intermediate Layer	Thickness (nm)	Substrate and method
Si	$SrTiO_3$ [48]	8	On Si substrate by MBE
Si, Si_3N_4, SiO_2, ..etc	LnO_2CO_3[19]	5-20 (Our Work)	Possible on number of different substrates
MgO	No intermediate layer [49]	-	RF sputtering

Substrate	Intermediate Layer	Thickness (nm)	Substrate and method
Si	MgO [49]	100-400	On Si, by RF sputtering
Si, Glass	Ti/Pt [50]	10/100	On different substrates by PLD
Si	$LaNiO_3$ [51]	100	Si
Si	$SrRuO_3$/YSZ [52]	20/70	On Si by PLD
Si	$SrTiO_3$ [53]	5	On Si by PLD and ALD

2.9 SEM analysis

The scanning electron microscope (SEM) images of BTO thin films grown on silicon <100> substrates with different thicknesses of the lanthanum nitrate intermediate layer are presented in Figure 2.21. The films annealed at 600°C, with intermediate layers of different thickness are amorphous and no distinct crystal grains are visible from the SEM measurements.

Figure 2.21(a) and Figure 2.21(b) show the top surface view of BTO films annealed at 700°C, with barrier layers of thickness 6 nm and 7.2 nm respectively. The presence of well-defined polygonal crystal grains is visible and it shows the complete transformation of the amorphous films into a perovskite phase. The presence of the intercrystal voids in the BTO films (~150 nm) deposited with intermediate layers less than 6 nm is visible in Figure 2.21(a) and Figure 2.21(c). However, the present work shows that the density of the intercrystal voids can be decreased to a great extent, by increasing the thickness of the intermediate layer to 7.2 nm. The films deposited with BTO seeding layers have further improved quality and appear to have a dense structure without the presence of pin holes (Figure 2.21(d)). It is also found that as the thickness of the BTO film before annealing is increased above 150 nm, the annealing process results in nano-cracks on the film surface.

The SEM cross-section images as shown in Figure 2.21(c) and Figure 2.21(d) are prepared by cleaving the silicon sample. The cleaving causes rough edges and the brittle nature of the thin film results in numerous

regions without material. The presence of the thin intermediate layer is evident and the thickness matches with data from ellipsometer measurements. The grain sizes of the films deposited at 700°C, with an intermediate layer of thickness 7.2 nm is found to be between 30 - 50 nm, which is comparable to other reported values [54].

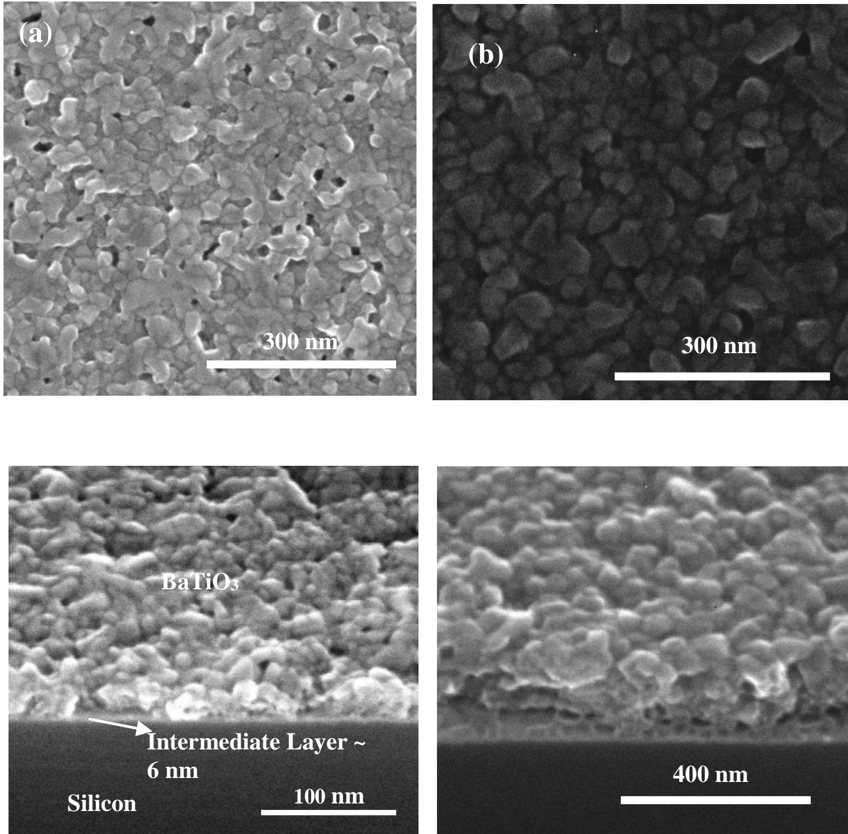

Figure 2.21: SEM top view of BTO thin films annealed at 700°C, with intermediate layer of (a) 6 nm (b) 7.2 nm. Cross section image of the BTO film deposited at 700°C (c) prepared with layer-by-layer annealing for each 30 nm layer, with a intermediate layer of 8.9 nm (d) deposited with an intermediate layer of 6 nm, as shown in Figure 2.21(a).The SEM cross-section images as shown in Figure 2.21(c) and Figure 2.21(d) are prepared by cleaving the silicon sample.

2.10AFM analysis

Atomic force microscopy (AFM) measurements are carried out to estimate the roughness properties of the BTO films. The AFM images of the 150 nm thick BTO films deposited at 700°C, for different thicknesses of the intermediate layers are shown in Figure 2.22(a) and Figure 2.22(b).

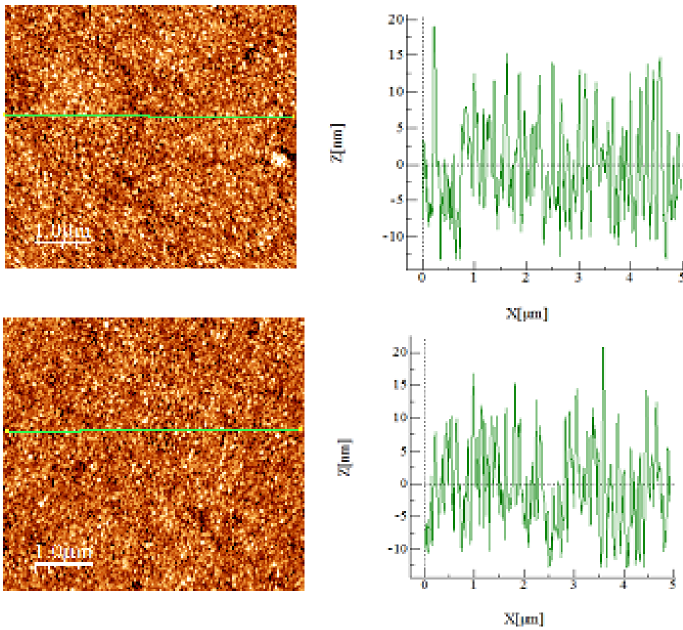

Figure 2.22: AFM images of the BTO thin films deposited at 700°C, for different thicknesses of the intermediate layers (a) 6 nm (b) 7.2 nm.

The film deposited with the 4.4 nm intermediate layer shows an average roughness of 10 nm, whereas the films deposited with intermediate layers greater than 6 nm, show a larger roughness (10 to 15 nm), because of the larger grain sizes.

2.11 XRD- BZT thin films

$BaTiO_3$ and $Ba(Zr,Ti)O_3$ films were developed as an alternative to the Pb-based ferroelectric thin films. A wide range of BTO thin films are reported with various type of dopants such as Sr, Zr and Mn [55], [56], [57]. These doped BTO films have already been used to demonstrate enhanced electro-

optic effects ($Ba(Sr,Ti)O_3$), strong dielectric constant and good tunability of the dielectric constant ($Ba(Zr, Ti)O_3$).

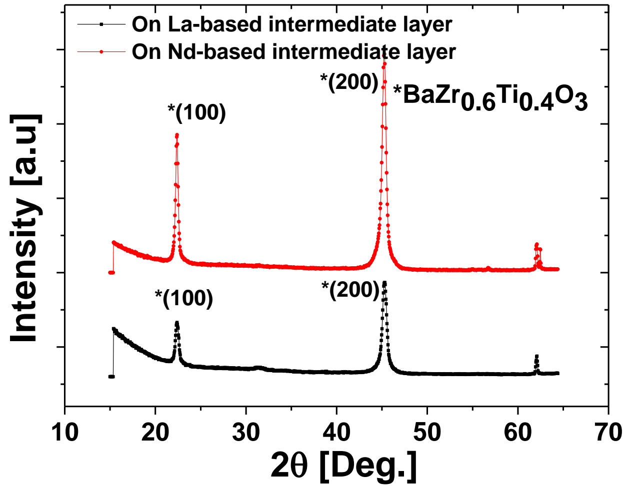

(a)

Figure 2.23: XRD measurements of the BZT thin films annealed at 700°C, on intermediate layers of La and Nd (thickness ~ 10 nm), which are heat treated at 500°C and 450°C, respectively.

Figure 2.23 represent the XRD patterns of the barium zirconate titanate (BZT) thin films deposited on a silicon substrate coated with intermediate layers of La and Nd and annealed at 700˚C. The thickness of the intermediate layers is 10 nm for this experiment. The annealing temperature required for crystallization of the BZT film is larger compared to the PZT thin films. It is evident from the measurements that the BZT films show a strong preferential (100) orientation, very similar to the results observed for the PZT films. However, as the annealing temperature is decreased down to < 650°C, no distinguishable diffraction peaks are observed corresponding to the BZT films. The x-ray pole figure analysis of the BZT film produces results identical to the PZT films, without any specific in-plane texture (see Figure 2.24). We also repeated the measurements on glass and ITO/glass substrates and this produces identical results as in the case of PZT films.

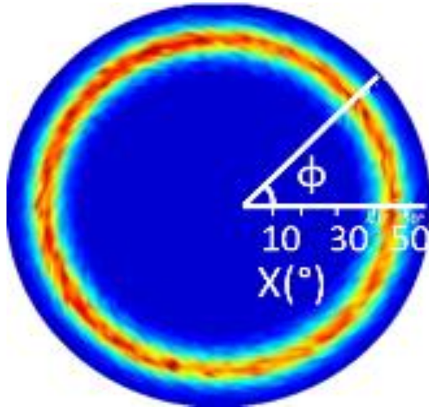

Figure 2.24: X-ray pole figure of $Ba(Zr,Ti)O_3$ thin film deposited on Si substrate coated with La-based intermediate layer of thickness ~ 10 nm and heat treated at 500°C.

2.12 $LiNbO_3$ thin films

Single crystalline $LiNbO_3$ based waveguide technology is widely used for electro-optic and non-linear optic devices. In recent years there were attempts to integrate $LiNbO_3$ thin films onto silicon substrates. However, most of the devices reported with $LiNbO_3$ on the Si platform are based on a complex layer bonding technique [58]. In our work, we fabricated $LiNbO_3$ thin films directly on Si/glass substrate using the CSD technique, following the novel intermediate layers based deposition procedure.

Reagent grade lithium ethoxide $Li(CH_3COO)_2$ and niobium(V) pentaethoxide $Nb(OCH_2CH_3)_5$, were chosen as the source materials for lithium and niobium, whereas glacial acetic acid and 2-methoxy ethanol was used as the solvents [2]. Firstly, lithium ethoxide is dissolved completely in acetic acid at room temperature and further diluted in 2-methoxyethanol. Secondly, niobium ethoxide is added dropwise, in 1:1 molar proportion, with constantly string the solution at 80°C.

The molarity of the solution is adjusted to 0.2M. The solution is then allowed to cool to room temperature with continuous refluxing over 24 hours. The solution has been filtered prior to the deposition process. The solution is the then spin coated using the standard procedure as mentioned in section 2.5.

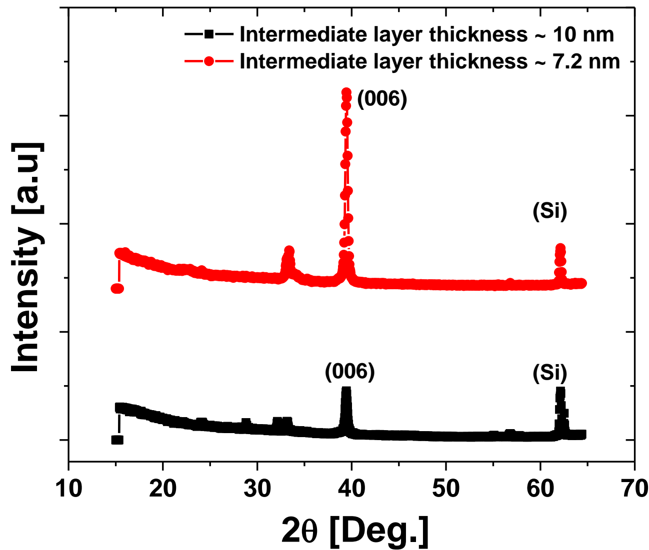

Figure 2.25: XRD measurements of the $LiNbO_3$ thin films annealed at 700°C, on Si substrate coated with $La_2O_2CO_3$ intermediate layers of different thicknesses.

Figure 2.25 represents the x-ray diffraction pattern of the $LiNbO_3$ thin film deposited on a Si substrate. It is evident from the measurements that the $LiNbO_3$ thin films deposited on Si substrate show a strong preferential orientation. However, films which are deposited on intermediate layers less than 7 nm develop micro-cracks after the high temperature annealing process. The experiments were carried out on different substrates, annealing temperatures and intermediate layers produce identical results as in the case of PZT, PLZT, BTO and BZT thin films. Even-though the direct deposition of $LiNbO_3$ thin films are demonstrated directly on Si substrates electro-optic properties of the demonstrated films are rather low compared to other ferroelectric thin films [59]

2.13 Overview of ferroelectric thin film deposition

Table 2.3 give an overview of different ferroelectric thin films deposited over different Ln- based intermediate layer.

Table 2.3: Overview of ferroelectric thin film depositions carried out over Ln-based intermediate layer

	Intermediate layer			
Ferroelectric thin film	$La_2O_2CO_3$	$Nd_2O_2CO_3$	$Pr_2O_2CO_3$	$Sm_2O_2CO_3$
PZT	yes	yes	yes	yes
PLZT	yes	yes	yes	yes
BZT	yes	yes	no	no
BTO	yes	yes	no	no
$LiNbO_3$	yes	No	no	no

2.14 Conclusion

In conclusion, a novel strategy for fabricating highly textured PZT thin films on silicon and a number of different substrates have been developed, by utilizing a chemical solution deposition route. As the first part of the work, novel dielectric thin film based intermediate layers are investigated.

It is known that strongly oriented thin films exhibits superior properties compared to randomly oriented counterparts. As the goal of this thesis is to use the ferroelectric thin films as cladding for Si or Si_3N_4 waveguides, the intermediate layer thickness is an important constraint. Here, we have demonstrated a number of novel ultra-thin lanthanide based intermediate layers (thickness- 5 to 15 nm) as template layers for c-axis textured thin film growth (with a high degree of orientation > 99.8%) on different substrates. A variety of well-known electro-optic thin films are successfully developed with this new deposition procedure. This includes PZT, PLZT, BTO, BZT and $LiNbO_3$. Moreover, as the intermediate layer preserves its orientation regardless of the substrate, our novel method offers the flexibility to grow good quality ferroelectric thin films with a high degree of orientation on amorphous and crystalline substrates (Si, SiO_2, Si_3N_4, glass, ITO etc). Compared to the porous films reported before the structural characterization of our films demonstrate strong preferential thin film growth, with well packed, crack free polygonal crystal grains The novel deposition method offers a low cost and simple method to produce good quality, strongly electro-optic PZT thin films on crystalline and amorphous (SiO_2 and Si_3N_4) substrates for a variety of integrated photonics and electronics applications, where the properties of the films can be tuned for applications spanning from microwave to optical frequencies.

2.15 References

1. Pal, M., et al., Ferroelectric-relaxor behavior of highly epitaxial Barium Zirconium Titanate thin films. Journal of Nano Research, 2015. 34: p. 67-72.
2. Satapathy, S., et al., Blue shift of optical band-gap in LiNbO3 thin films deposited by sol-gel technique. Thin Solid Films, 2012. 520(21): p. 6510-6514.
3. Cooney, T.G. and L.F. Francis, Processing of sol-gel derived PZT coatings on non-planar substrates. Journal of Micromechanics and Microengineering, 1996. 6: p. 291-300.
4. Frunza, R., et al., Preparation and characterisation of PZT films by RF-magnetron sputtering. Journal of Alloys and Compounds, 2011. 509: p. 6242-6246.
5. Menou, N. and H. Funakubo, (111)-oriented Pb(Zr,Ti)O(3) films deposited on SrRuO(3)/Pt electrodes: Reproducible preparation by metal organic chemical vapor deposition, top electrode influence, and reliability. Journal of Applied Physics, 2007. 102: p. 114105.
6. Borowiak, A.S., et al., Pulsed laser deposition of epitaxial ferroelectric Pb(Zr,Ti)O-3 films on silicon substrates. Thin Solid Films, 2012. 520: p. 4604-4607.
7. Chen, L., et al., Microstructure control of (Pb,Sr)TiO3 films on Pt/Ti/SiO2/Si substrates by a TiO2 buffer layer. Thin Solid Films, 2008. 516: p. 1285-1289.
8. Yu, J., et al., Optical and electrical properties of highly (100)-oriented PbZr1-xTixO3 thin films on the LaNiO3 buffer layer. Journal of Applied Physics, 2004. 96(5): p. 2792-2799.
9. Shih, W.C., Z.Z. Yen, and Y.S. Liang, Preparation of highly C-axis-oriented PZT films on Si substrate with MgO buffer layer by the sol-gel method. Journal of Physics and Chemistry of Solids, 2008. 69: p. 593-596.
10. Chen, L. and R.M. Reano, Compact electric field sensors based on indirect bonding of lithium niobate to silicon microrings. Optics Express, 2012. 20(4): p. 4032-4038.
11. Abel, S., et al., A strong electro-optically active lead-free ferroelectric integrated on silicon. Nature Communications, 2013. 4: p. 1-6.
12. Dey, S.K., K.D. Budd, and D.A. Payne, THIN-FILM FERROELECTRICS OF PZT BY SOL-GEL PROCESSING. Ieee Transactions on Ultrasonics Ferroelectrics and Frequency Control, 1988. 35(1): p. 80-81.

13. Schwartz, R.W., et al., Comments on the effects of solution precursor characteristics and thermal processing conditions on the crystallization behavior of sol-gel derived lead zirconate titanate thin films. Journal of Materials Research, 1997. 12(2): p. 444-456.
14. Lakeman, C.D.E. and D.A. Payne, PROCESSING EFFECTS IN THE SOL-GEL PREPARATION OF PZT DRIED GELS, POWDERS, AND FERROELECTRIC THIN-LAYERS. Journal of the American Ceramic Society, 1992. 75(11): p. 3091-3096.
15. Schwartz, R.W., Chemical solution deposition of perovskite thin films. Chemistry of Materials, 1997. 9(11): p. 2325-2340.
16. Brooks, K.G., et al., ORIENTATION OF RAPID THERMALLY ANNEALED LEAD-ZIRCONATE-TITANATE THIN-FILMS ON (111) PT SUBSTRATES. Journal of Materials Research, 1994. 9(10): p. 2540-2553.
17. Lefevre, M.J., et al., Microstructural development in sol-gel derived lead zirconate titanate thin films: The role of precursor stoichiometry and processing environment. Journal of Materials Research, 1996. 11(8): p. 2076-2084.
18. Klee, M., et al., ANALYTICAL STUDY OF THE GROWTH OF POLYCRYSTALLINE TITANATE THIN-FILMS. Philips Journal of Research, 1993. 47(3-5): p. 263-285.
19. George, J.P., et al., Preferentially oriented BaTiO3 thin films deposited on silicon with thin intermediate buffer layers. Nanoscale Research Letters, 2013. 8: p. 1-7.
20. Balboul, B.A.A. and A.Y.Z. Myhoub, The characterization of the formation course of neodymium oxide from different precursors: A study of thermal decomposition and combustion processes. Journal of Analytical and Applied Pyrolysis, 2010. 89: p. 95-101.
21. Shirsat, A.N., et al., Thermochemistry of La2O2CO3 decomposition. Thermochimica Acta, 2003. 399: p. 167-170.
22. Olafsen, A. and H. Fjellvag, Synthesis of rare earth oxide carbonates and thermal stability of Nd2O2CO3II. Journal of Materials Chemistry, 1999. 9: p. 2697-2702.
23. Dutta, S., A.A. Jeyaseelan, and S. Sruthi, Ferroelectric and Piezoelectric properties of (111) oriented lanthanum modified lead zirconate titanate film. Thin Solid Films, 2014. 562: p. 190-194.
24. Kingon, A.I. and S. Srinivasan, Lead zirconate titanate thin films directly on copper electrodes for ferroelectric, dielectric and piezoelectric applications. Nature Materials, 2005. 4(3): p. 233-237.
25. Ahmed, M. and D.P. Butler, Modified lead titanate thin films for pyroelectric infrared detectors on gold electrodes. Infrared Physics & Technology, 2015. 71: p. 1-9.

26. Kondo, M., K. Maruyama, and K. Kurihara, Epitaxial ferroelectric thin films on silicon substrates for future electronic devices. Fujitsu Scientific & Technical Journal, 2002. 38(1): p. 46-53.
27. Lin, Y., et al., Growth and polarization features of highly (100) oriented Pb(Zr0.53Ti0.47)O-3 films on Si with ultrathin SiO2 buffer layer. Applied Physics Letters, 1998. 73: p. 2781-2783.
28. Sriram, S., et al., Nanocolumnar Preferentially Oriented PSZT Thin Films Deposited on Thermally Grown Silicon Dioxide. Nanoscale Research Letters, 2009. 4(1): p. 29-33.
29. Gupta, R., et al., Deposition of nanosized grains of ferroelectric lead zirconate titanate on thin films using dense plasma focus. Journal of Physics D-Applied Physics, 2004. 37(7): p. 1091-1094.
30. Pandey, S.K., et al., Structural, ferroelectric and optical properties of PZT thin films. Physica B-Condensed Matter, 2005. 369(1-4): p. 135-142.
31. Rawn, C.J., et al., INFLUENCE OF TI INTERFACIAL LAYERS ON THE ELECTRICAL AND MICROSTRUCTURAL PROPERTIES OF SOL-GEL PREPARED PZT FILMS. Integrated Ferroelectrics, 1995. 6(1-4): p. 111-119.
32. Wein-Duo, Y. and S.M. Haile, Characterization and microstructure of highly preferred oriented lead barium titanate thin films on MgO (100) by sol-gel process. Thin Solid Films, 2006. 510(1-2): p. 55-6161.
33. Wang, Y., et al., Epitaxial ferroelectric Pb(Zr, Ti)O-3 thin films on Si using SrTiO3 template layers. Applied Physics Letters, 2002. 80(1): p. 97-99.
34. Xiong, C., et al., Active Silicon Integrated Nanophotonics: Ferroelectric BaTiO3 Devices. Nano Letters, 2014. 14: p. 1419-1425.
35. Klingenberg, B. and M.A. Vannice, Influence of pretreatment on lanthanum nitrate, carbonate, and oxide powders. Chemistry of Materials, 1996. 8: p. 2755-2768.
36. Olafsen, A. and H. Fjellvag, Synthesis of rare earth oxide carbonates and thermal stability of Nd2O2CO3II. Journal of Materials Chemistry, 1999. 9(10): p. 2697-2702.
37. Shirsat, A.N., et al., Thermochemistry of La2O2CO3 decomposition. Thermochimica Acta, 2003. 399(1-2): p. 167-170.
38. George, J.P., et al., Lanthanide-Assisted Deposition of Strongly Electro-optic PZT Thin Films on Silicon: Toward Integrated Active Nanophotonic Devices. Acs Applied Materials & Interfaces, 2015. 7(24): p. 13350-13359.

39. Bose, A., M. Sreemany, and S. Bysakh, Role of TiO2 Seed Layer Thickness on the Nanostructure Evolution and Phase Transformation Behavior of Sputtered PZT Thin Films During Post-Deposition Air-Annealing. Journal of the American Ceramic Society, 2011. 94(11): p. 4066-4077.
40. Mhin, S., et al., Role of the PbTiO3 Seed Layer on the Crystallization Behavior of PZT Thin Films. Journal of the American Ceramic Society, 2015. 98(5): p. 1407-1412.
41. Rodriguez-Aranda, M.C., et al., Synthesis and optical characterization of Pb(Zr0.53Ti0.47)O-3 thin films on indium tin oxide/quartz substrates by a simplified sol-gel route. Journal of Materials Science-Materials in Electronics, 2015. 26(6): p. 3486-3492.
42. Fujito, K., et al., Stress control and ferroelectric properties of lead zirconate titanate (PZT) thin film on Si substrate with buffer layers. Japanese Journal of Applied Physics Part 1-Regular Papers Brief Communications & Review Papers, 2005. 44(9B): p. 6900-6904.
43. Shih, W.C., Z.Z. Yen, and Y.S. Liang, Preparation of highly C-axis-oriented PZT films on Si substrate with MgO buffer layer by the sol-gel method. Journal of Physics and Chemistry of Solids, 2008. 69(2-3): p. 593-596.
44. Selvaraja, S.K., et al., Fabrication of Photonic Wire and Crystal Circuits in Silicon-on-Insulator Using 193-nm Optical Lithography. Journal of Lightwave Technology, 2009. 27(18): p. 4076-4083.
45. Tong, S., et al., Lead Lanthanum Zirconate Titanate Ceramic Thin Films for Energy Storage. Acs Applied Materials & Interfaces, 2013. 5(4): p. 1474-1480.
46. Kobayashi, T., et al., Microelectromechanical systems-based electrostatic field sensor using Pb(Zr,Ti)O-3 thin films. Japanese Journal of Applied Physics, 2008. 47: p. 7533.
47. Qiao, L. and X.F. Bi, Origin of compressive strain and phase transition characteristics of thin BaTiO3 film grown on LaNiO3/Si substrate. Physica Status Solidi a-Applications and Materials Science. 207(11): p. 2511-2516.
48. Abel, S., et al., A strong electro-optically active lead-free ferroelectric integrated on silicon. Nature Communications, 2014. 4: p. 1-6.
49. Qiao, L. and X.F. Bi, Crystallographic Texture of MgO and its effect on the growth of BaTiO3 thin films by RF sputtering, in 2006 BIMW: 2006 Beijing International Materials Week, Pts 1-4: MAGNESIUM - ALUMINIUM MATERIALS - AEROSPACE MATERIALS - SUPERCONDUCTING AND FUNCTIONAL

MATERIALS, S. Long, et al., Editors. 2007, Trans Tech Publications Ltd: Stafa-Zurich. p. 2175-2178.
50. Yang, Y.D., et al., Pulsed Laser Deposition of BaTiO3 Thin Films on Different Substrates. Journal of Nanomaterials, 2010.
51. Qiao, L. and X.F. Bi, Effect of LaNiO3 buffer layer thickness on the microstructure and electrical properties of (100)-oriented BaTiO3 thin films on Si substrate. Thin Solid Films, 2009. 517(13): p. 3784-3787.
52. Colder, H., et al., Structural characterisation of BaTiO3 thin films deposited on SrRuO3/YSZ buffered silicon substrates and silicon microcantilevers. Journal of Applied Physics, 2014. 115(5).
53. Niu, G., et al., Epitaxy of BaTiO3 thin film on Si(001) using a SrTiO3 buffer layer for non-volatile memory application. Microelectronic Engineering, 2011. 88(7): p. 1232-1235.
54. Huang, L.M., et al., Barium titanate nanocrystals and nanocrystal thin films: Synthesis, ferroelectricity, and dielectric properties. Journal of Applied Physics, 2006. 100(3).
55. Kim, J.Y., C.R. Song, and H.I. Yoo, Mn-doped BaTiO3: Electrical transport properties in equilibrium state. Journal of Electroceramics, 1997. 1(1): p. 27-39.
56. Kumar, V., et al., Chemical solution deposition of (Ba1-xSrx)TiO3 thin films and characterization. Journal of the American Ceramic Society, 2006. 89(3): p. 1136-1139.
57. Aghayan, M., et al., Sol-gel combustion synthesis of Zr-doped BaTiO3 nanopowders and ceramics: Dielectric and ferroelectric studies. Ceramics International, 2014. 40(10): p. 16141-16146.
58. Park, Y.B., et al., Integration of single-crystal LiNbO3 thin film on silicon by laser irradiation and ion implantation-induced layer transfer. Advanced Materials, 2006. 18(12): p. 1533-+.
59. Akazawa, H. and M. Shimada, Spectroellipsometric approach to determine linear electro-optic coefficient of c-axis-oriented LiNbO3 thin films. Journal of Applied Physics, 2005. 98(11).

Chapter 3

Electrical and Electro-optical Characterization

3.1 Introduction

Although research on ferroelectric thin films is focused mostly on electronic applications, there is an increasing interest towards the use of these films in the optical domain. This is mainly driven by the ever increasing demand for higher bandwidth in computing, telecom, etc. while keeping the power consumption limited. To realize optical data transmission e.g. for chip to chip interconnects, integrated optical devices which are compatible with the electronic platform are indispensable. The well-established ferroelectric oxide based technologies propelled the development of high-speed electro-optic devices on different material platforms, such as LiNbO3. Integrated devices on photonic platforms, such as the silicon based photonic platform, on the other hand do not yet exploit the strong linear electro-optic (EO) properties of ferroelectric thin films [1]. The current state-of-the-art high-speed integrated optical devices are based on $LiNbO_3$ single crystals [2]. The current state-of-the-art high-speed integrated optical devices are based on $LiNbO_3$ single crystals [2]. Lithium niobate exhibits a wide transparency window (0.35 µm to 5.2 µm) and a strong second order non-linear susceptibility which is absent in centrosymmetric semiconductors like Si.

The second order susceptibility allows control of the refractive index of the material via the electro-optic effect, but also allows four-wave mixing and second harmonic generation for wavelength conversion. Using the piezo-electric properties of the material acousto-optic devices can also be developed. Due to the need for rare and costly elements, such substrates are extremely expensive compared to Si single crystals. Replacing the $LiNbO_3$ as substrate and EO material with ferroelectric thin film oxides integrated on the compact silicon photonic platform, could be an alternative to realize smaller, functional and power efficient devices [3],[4, 5],[6, 7],[8].

In the previous chapter, we presented a novel method to deposit ferroelectric thin films on different substrates and details were given concerning the structural properties. This chapter reports on the electrical characterization of PZT, BTO, BZT and $LiNbO_3$ thin films and the electro-optical characterization of the highly oriented PZT thin films. The first half of the chapter deals with the dielectric properties (permittivity obtained with small signal analysis), ferroelectric properties (remnant polarization and coercive field) and current-voltage characterization (electrical conductivity and breakdown field). The electrical measurements presented in this chapter indicate that the deposited films possess high dielectric constant and low dielectric loss. The current-voltage (I-V) characterization confirms the good quality of the deposited ferroelectric thin films with low leakage current and high break-down electric field. The second half of the chapter deals with the electro-optic characterization of the PZT film. The variations in the pockels coefficient with respect to the intermediate layers used, annealing temperature and different PZT compositions are analysed in detail.

3.2 Sample Preparation

The samples prepared for the C-V and C-F measurements use either commercially available ITO (30nm) on glass (Delta Technologies, Inc., USA) or platinized Si (Pt/Ti (100 nm/15 nm) substrates. Ti/Pt electrodes are deposited with electron-gun evaporation. The Si substrate is cleaned in acetone and 1-propanol before the deposition. The thin Ti layer (10 – 15 nm) is used as an adhesion layer before the Pt deposition. The Pt layers are deposited at a rate of 0.6 Å/second and show very good adhesion with the Si substrate.

Prior to the measurements, a top electrode is deposited with either chromium (Cr), gold (Au) or indium tin oxide (ITO) (with surface area

ranging from 0.09 mm^2 to 3.14 mm^2, thickness 50 nm – 100 nm) by e-gun evaporation. The gold contact is deposited at a much slower rate of 0.5 Å/second, to improve the adhesion on the ferroelectric thin film. We found as the deposition rate is increased, the gold contact delaminates upon contact with the measurement probes. Transparent ITO top electrodes are not ideal for electrical measurements because of the high resistivity of the ITO layer, at higher frequencies. ITO top contacts are mainly fabricated for devices used for electro-optic measurements, requiring a top transparent electrode. Since e-gun evaporation does not result in high quality ITO, its properties (transparency and conductivity) are enhanced by a post-deposition heat treatment in flowing oxygen.

3.3 Electrical characterization

The electrical characterization of the films is carried out in terms of capacitance versus voltage (C-V) and capacitance versus frequency (C-F) and current-voltage (I-V) measurements.

3.3.1 Dielectric constant and dielectric loss measurements- PZT thin films

The C-V and C-F (up to 1 MHz) characteristics are measured with a HP4192ALF impedance analyzer. C-V measurements are carried out both on glass and silicon substrates, whereas the C-F measurements are limited to the platinized Si substrate. The voltage is applied to the metal (Au)/insulator (PZT)/metal (Pt) (MIM) structure to perform these measurements. The capacitance-voltage (C-V) hysteresis loops of the PZT thin films on different template layers are illustrated in Figure 3.1. The C-V measurement shows the small signal (V_{ac} = 0.1V) capacitance as a function of the step-wise increased DC bias voltage. The dielectric constant and the loss tangent are extracted from these measurement. Assuming the parallel plate capacitor model, the dielectric constant of the film is calculated using the following equation,

$$c = \frac{\varepsilon_0 \varepsilon_r A}{d}$$

Where c is the capacitance of the PZT film, ε_0 dielectric permittivity in the free space, ε_r is the relative permittivity, A is the area of the electrode and d is the thickness of the PZT thin film.

The measurements feature well-defined butterfly hysteresis loops that saturate at high electric fields with good dielectric tunability. The effective dielectric constant that is obtained from the measurement of the capacitance includes the effect of both the intermediate and the PZT layer. Two maxima for the dielectric constants are observed depending on the direction of the electric field, showing the hysteresis nature of the PZT thin films.

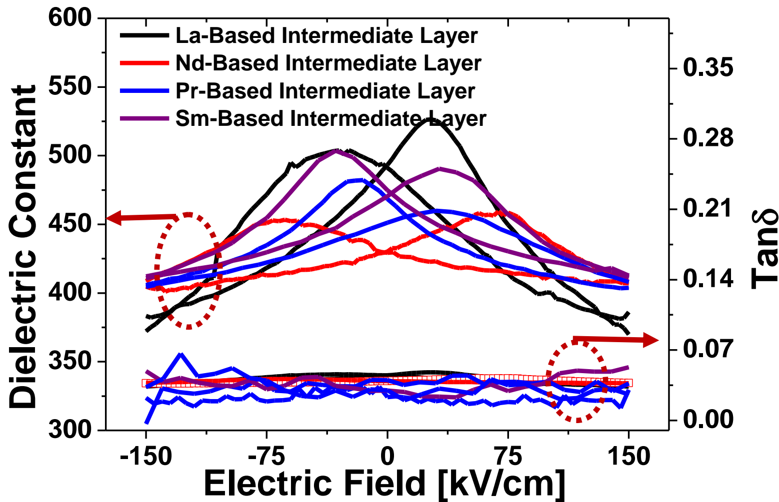

Figure 3.1: Small-signal (Vac = 0.1V, f = 10 kHz) relative dielectric constant of the PZT(52/48) thin films (annealed at 630°C, thickness ~ 600 nm), on different template layers, as a function of applied electric field.

As seen from Figure 3.1, when the DC voltage increased from 0 to 150 kV/cm, the permittivity of the PZT films decreases from 540 to 360, 455 to 400, 502 to 413, and 482 to 405, for La, Nd, Pr and Sm based template layers, respectively. The dielectric loss of the films are 0.045, 0.02, 0.04, 0.36 (at 0 kV/cm) and 0.038, 0.027, 0.02, 0.017 (at 200 kV/cm), respectively for PZT films on La, Nd, Pr, and Sm based template layers. The measurement of PZT film on La-based intermediate layer show a much wider tuning range of the dielectric constant compared to the other intermediate layers. These results are comparable to previously reported results [9].

Figure 3.2 represents the dielectric constant versus voltage characteristics of the PZT films with two different PZT compositions, deposited on Si

substrates coated with Pr-based intermediate layer. A slight decrease in the dielectric characteristics are noted for both 40/60 and 60/40 compositions, compared to the PZT film at morphotropic phase boundary (MPB) composition 52/48 (see Figure 3.1).

The rhombohedral PZT 60/40 film exhibits a dielectric constant of 478 to 425 and dielectric loss of 0.05 to 0.03 as the electric field is increased from 0 to 150 kV/cm. Whereas the tetragonal 40/60 composition show a variation in the dielectric constant of 468 to 417 and a dielectric loss of 0.05 to 0.04, respectively. The variations observed for different Zr, Ti ratio follow the same trend as in the previously reported results [10].

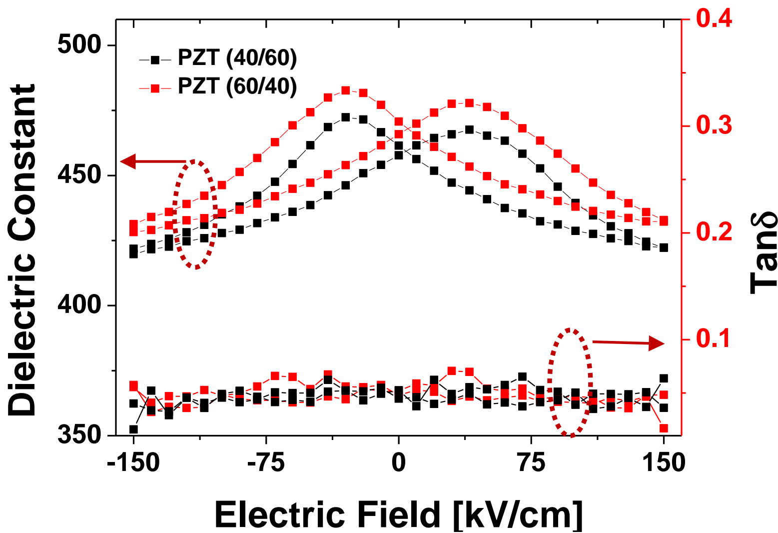

Figure 3.2: Small-signal (V_{ac} = 0.1V, f = 10 kHz) relative dielectric constant of the PZT thin films (annealed at 630°C, thickness ~ 600 nm) deposited on Pr-based template layer (heat treated at 500°C) for different Zr,Ti ratios.

PZT films with composition near the Morphotropic Phase Boundary (MPB) (PZT (52/48)) exhibit a larger dielectric constant due to the increased number of available domain states near the MPB [11]. At MPB, tetragonal and rhombohedral phases co-exist. There are 14 allowed domain states at the MPB, including 6 possible domain states from the ferroelectric tetragonal phase and 8 possible domain states from the ferroelectric rhombohedral phase. Furthermore, not only 90° and 180° domain walls (from tetragonal

geometry) exist, but also 71° and 109° domain wall exist. The spontaneous polarization can be aligned more precisely with an external electric field direction, thus increases dielectric constant and poling efficiency of the PZT films [11].

Figure 3.3 plots the permittivity and dielectric loss tangent as a function of frequency (V_{ac} = 0.1V) for the PZT thin films annealed at 630°C, on La, Pr and Nd template layers. The measurements show a steady response of the dielectric constant and loss tangent up to 1 MHz. In order to perform the measurements in the GHz regime, special electrodes designs compatible with the high speed probes are required. Travelling wave electrodes are reported with a co-planar electrode configuration to measure the ferroelectric properties of the PZT films till 40 GHz [12]. Pt electrodes are highly undesirable at microwave frequencies due to the high resistivity. Unlike the measurements we carried out with a Pt bottom electrode, it is essential to use a combination of Pt/Au/Pt [13] or Cu electrodes with an amorphous TiAl passivation layer [14] to reduce the electrode resistance for MIM capacitor measurements.

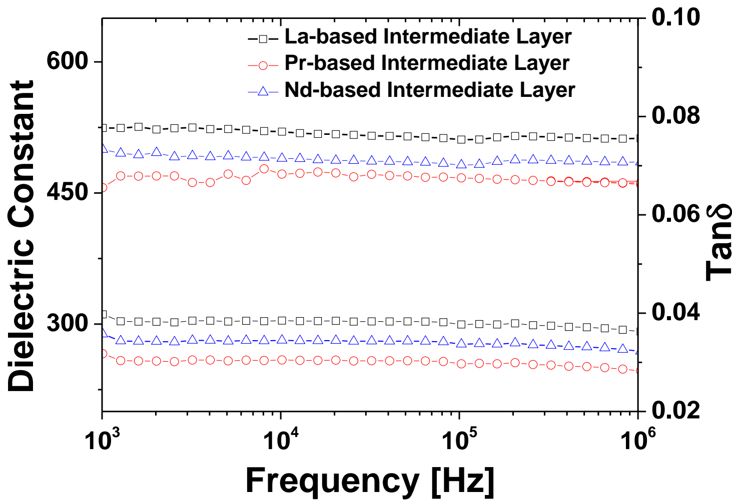

Figure 3.3: Small-signal (V_{ac} = 0.1V) relative dielectric constant and dielectric loss of the PZT (52/48) thin films (annealed at 630°C, thickness ~ 600 nm), on different template layers, as a function of frequency (E_{dc} = 0V).

On overview of the dielectric properties of the films tested in this work is given in Table 3.1.

Table 3.1: Comparison of dielectric properties between different PZT layers

Composition	Dielectric constant	Dielectric loss
PZT(52/48)	540	0.038
PZT(52/48)	502	0.02
PZT(52/48)	455	0.017
PZT(40/60)	468	0.05
PZT(60/40)	478	0.05

3.3.2 P-E hysteresis measurements-PZT thin films

Ferroelectric materials have the unique property to possess spontaneous polarization. The direction of the polarization can be reversed by an applied electric field and this results in a nonlinear hysteresis loop when measuring P. Materials exhibit ferroelectricity below the Curie temperature (T_c) and are paraelectric above this temperature. A Sawyer–Tower circuit (see Figure 3.4) is typically used for experimentally determining the ferroelectric hysteresis loop below T_c. The measurements are carried out at frequencies in the range 100 Hz - 1 kHz with a sinusoidal ac-voltage with an amplitude of 30 V peak-to-peak.

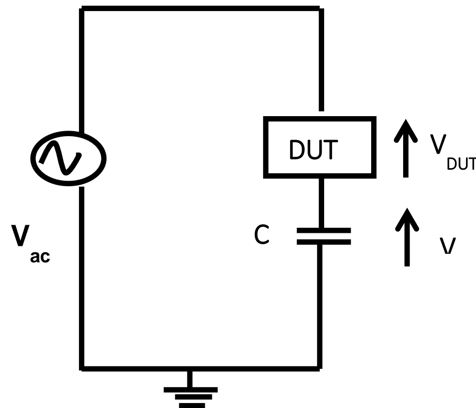

Figure 3.4: Sawyer-tower circuit to measure the P-E hysteresis of a ferroelectric capacitor.

A MIM capacitor is also used for the hysteresis measurements. The remnant polarization (P_r) and the coercive field (E_c) can be acquired through a P-E hysteresis measurement. The circuit is constructed by connecting the

ferroelectric capacitor in series with a known capacitor. Since the capacitors are connected in series the charge across the capacitors is the same.

$$Q = C*V$$

Where Q is the charge on either of the capacitors and V is the voltage across the known capacitor, which is measured with an oscilloscope. The polarisation can then be found as,

$$P = Q/A$$

Where A is the area of the electrodes on the ferroelectric capacitor. The hysteresis curve is plotted by putting the surface charge on the y-axis versus the electric field (voltage divided by layer thickness) applied across the material on the x-axis. The P-E hysteresis loop of a PZT capacitor (annealed at 630°C, thickness ~ 600 nm) deposited on a Pt/Si substrate coated with a La-based intermediate layer is shown in Figure 3.5. Here the P-E hysteresis measurements are plotted for an increasing electric field. The measurement saturates at electric field of about 200 kV/cm, showing coercive field (E_c) of 70 kV/cm and remnant polarization (P_r) of 25 μC/cm^2. Figure 3.6(a) represents the P-E hysteresis measurements of the PZT thin films deposited on lanthanum based intermediate layers annealed at different temperatures.

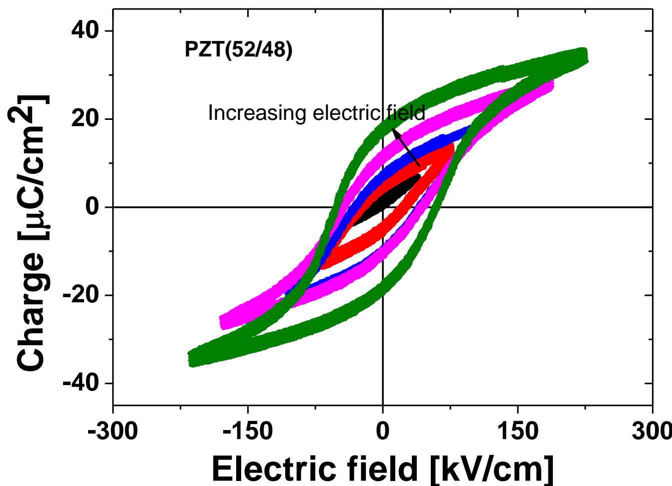

Figure 3.5: P-E hysteresis loop at different applied electric field for a PZT (52/48) thin film (annealed at 630°C, thickness ~ 600 nm) on a Si substrate coated with Nd-based intermediate layers (heat treated at 450°C, thickness ~ 10 nm).

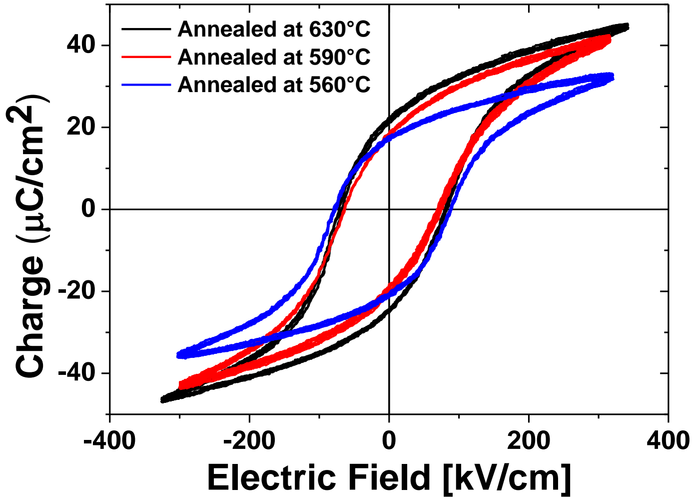

(a)

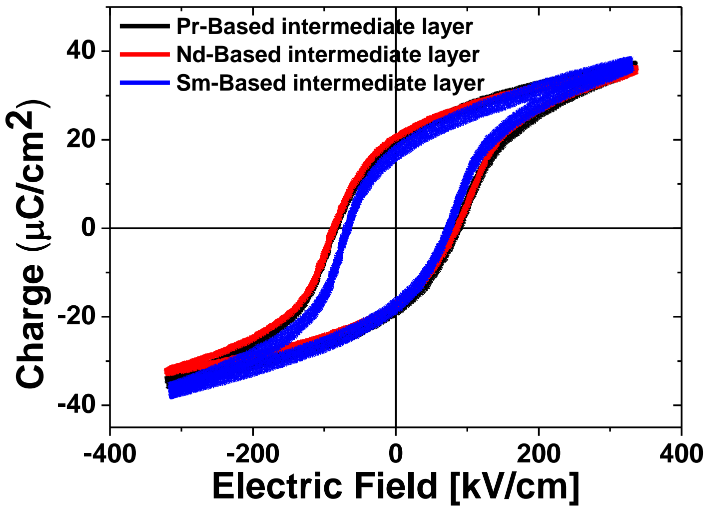

(b)

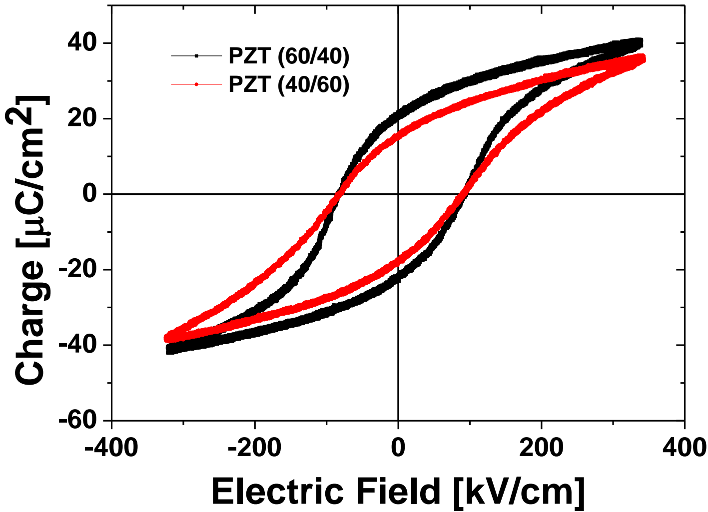

(c)

Figure 3.6: (a) P-E Hysteresis measurements of the PZT thin films (thickness ~ 600 nm, annealed at 630°C) (a) deposited on La based intermediate layer annealed at different temperature (b) deposited on different buffer layers and annealed at 630°C (c) deposited on Pr–based intermediate layer for different Zr:Ti ratios. The measurements are performed at 10 kHz.

The measurements indicate well saturated P-E hysteresis loops. The P_r and E_c of the PZT films (thickness – 600 nm) on a La-based template annealed at 630°C, 590°C and 560°C are 25 µC/cm^2, 19 µC/cm^2, 19 µC/cm^2 and 70 kV/cm, 68 kV/cm, 75 kV/cm, respectively. The PZT films annealed at 630°C show superior electrical properties to the films annealed at lower annealing temperature, with a higher remnant polarization and lower coercive field. The results are comparable to strongly (100) textured epitaxial PZT thin films on LSCO/STO/Si substrate reported by Wang et.al [15], with P_r of 20 µC/cm^2, however with a smaller coercive field of 40 kV/cm.

The grain boundaries are assumed to be the regions of lower permittivity. It means that the grain boundaries have poor ferroelectricity. Therefore, the polarization of the grain boundaries can be very low or even none. The lower the annealing temperature the grain boundaries increases as the grain size decreases. Consequently, a decrease in the remnant polarization is noticed. The annealing temperature influence on the ferroelectric properties are in

line with pervious measurements [16, 17]. Figure 3.6(b) shows hysteresis measurements of the PZT films annealed at 630°C on different intermediate layers. The PZT films exhibit a coercive field of 89 kV/cm, 78 kV/cm, 85 kV/cm and remnant polarization of 22 μC/cm^2, 21 μC/cm^2 and 20 μC/cm^2, on Nd, Sm, and Pr based intermediate layers, respectively. Comparing the results from Figure 3.6(a) and Figure 3.6 (b) Even though, the changes observed in the electrical properties of the PZT films are very small on different intermediate layer, the films deposited on La-based intermediate layer show a slightly higher remnant polarization and lower coercive field. Figure 3.6(c) represents the hysteresis measurements for the PZT films with two different compositions of 40/60 and 60/40 respectively. The remnant polarization and the coercive electric field of the tetragonal 40/60 and rhombohedral 60/40 PZT compositions (thickness – 600 nm, annealed at 630°C) on Pr-based intermediate layers are 17 μC/cm^2, 20.8 μC/cm^2 and 77 kV/cm, 82 kV/cm, respectively. Comparing the different composition of PZT (see Figure 3.6(a) and Figure 3.6(c), the films deposited at MPB exhibit superior electrical properties.

3.3.3 I-V measurements -PZT thin films

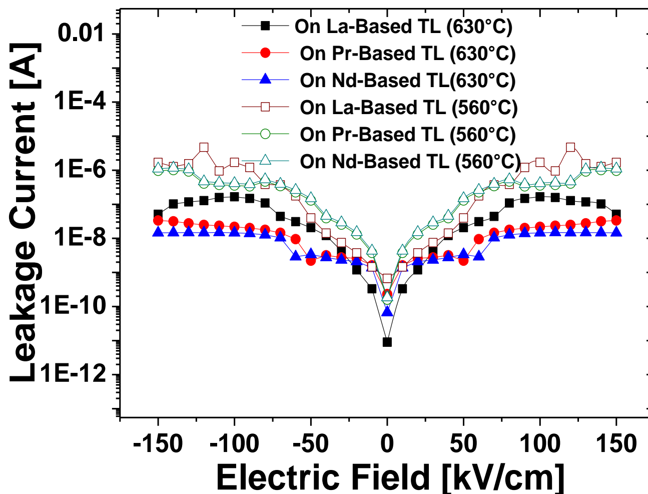

Figure 3.7: Leakage current measurements of the PZT films deposited on platinized Si substrates, coated with different intermediate layers and annealed at two different temperatures (electrode area- 3.14 mm^2)

The current- voltage (I-V) characterization of the PZT films on different intermediate layers as well as annealing temperature is given in Figure 3.7. I-V measurement are performed with a Keithley 236 source measure unit. The leakage current with applied electric field is in the order of 0.1 μA at 150 kV/cm for the PZT films annealed at 630°C on different buffer layers. However, as the annealing temperature is decreased to 560°C, the leakage current increases by an order of magnitude. The increase in the leakage current corresponds well with the decrease in the grain sizes seen in the SEM measurements for the samples annealed at lower temperatures.

3.4 Electrical measurements - BTO and BZT thin films

The dielectric and ferroelectric properties of BTO and BZT (40/60) thin films (thickness ~ 300 nm, annealing temperature ~ 700°C) grown on La-based intermediate layer (thickness ~ 7.2 nm or 8.9 nm, heat treatment ~ 450°C) are shown in Figure 3.8(a) and Figure 3.8(b), respectively. The dielectric constant-voltage measurement shows response with a characteristic butterfly shape indicating the ferroelectric hysteresis nature of the BTO and BZT tetragonal films.

The samples deposited with buffer layers below 6 nm often show electrical short-circuit between the top and bottom contacts, due to the intercrystal void formation. The highly oriented BTO films (thickness ~ 200 nm) deposited on a BTO seed layer, with buffer layers thicker than 7 nm, followed by layer by layer coating (BTO amorphous film ~ 30 nm) and annealing procedure, show well defined hysteresis loops, with characteristic butterfly dielectric response. The BTO and BZT thin films deposited with a 10 nm La-based intermediate layer show a dielectric constant of 270 and 350 respectively. The high dielectric constant of the BZT film shows that BZT can be used as a lead free alternative for PZT films. The P_r and E_c for the BTO and BZT films are estimated as 3.2 μC/cm^2, 6 μC/cm^2 and 55 kV/cm, 38 kV/cm, respectively.

A comparison of ferroelectric properties (P_r and E_c) of different thin films, deposited on different Ln based intermediate layer at different annealing temperatures are given in Table 3.2.

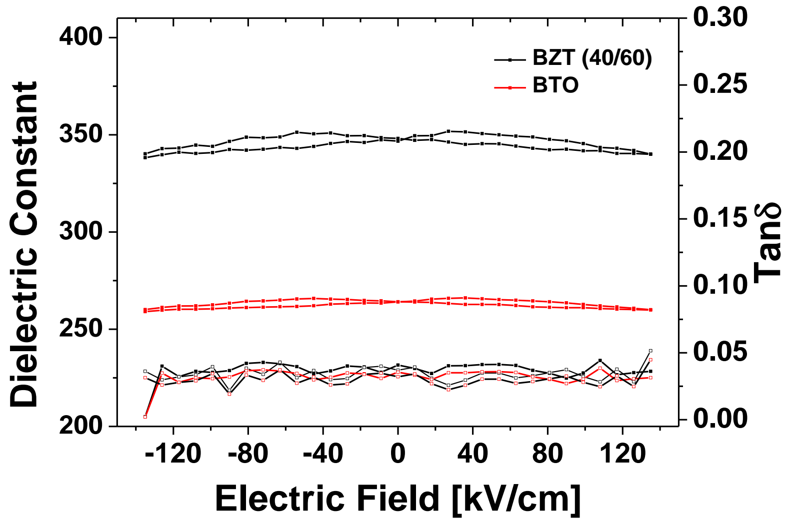

(a)

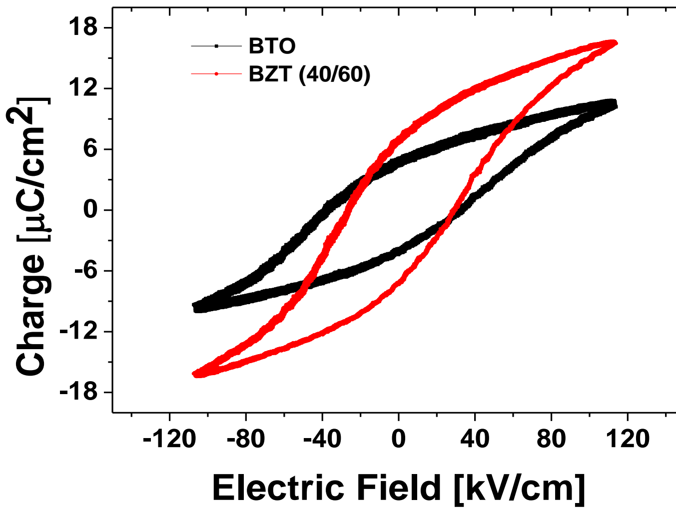

(b)

Figure 3.8: AC dielectric constant as a function of the DC electric field bias for a BTO thin film (~ 200 nm) annealed at 700°C with a 7.2 nm thick intermediate layer (b) P-E hysteresis loop measured at 1 KHz with an ac voltage swing of 10 V-PP , for the BTO films annealed at 700°C with intermediate layers of different thickness.

Table 3.2: Electrical measurement of ferroelectric thin films on different intermediate layers

Thin film	**Annealing temperature**	**Intermediate Layer**	P_r (μC/cm²)	E_c (kV/cm)
PZT (52/48)	630°C	PrO_2CO_3	20	85
PZT (52/48)	630°C	NdO_2CO_3	22	89
PZT (52/48)	630°C	SmO_2CO_3	21	78
PZT (52/48)	630°C	LaO_2CO_3	25	70
PZT (52/48)	560°C	LaO_2CO_3	19	68
PZT (52/48)	590°C	LaO_2CO_3	19	75
PZT (60/40)	630°C	LaO_2CO_3	20.8	82
PZT (40/60)	630°C	LaO_2CO_3	17	77
BZT (40/60)	700°C	LaO_2CO_3	3.2	55
BTO	700°C	LaO_2CO_3	6	38

3.5 Electro-optic characterization of PZT thin films

Before going towards electro-optic characterization of the PZT layers integrated on a waveguide platform, we measure the electro-optic effect of plain PZT layers. The measurement of the pockels coefficient of ferroelectric thin films is not evident and in literature a number of methods have been described and utilized. A comparison between different ferroelectric electro-optic materials and characterization methods is provided in Table 3.3.

Table 3.3: different ferroelectric thin films and electro-optic characterisation techniques

Thin film	**Intermediate Layer/substrate**	**Electro-optic coefficients (pm/V)**	**Method**
BTO	$SrTiO_3$ [8]	102	Lock-in detection
PZT (52/48)	LnO_2CO_3 [18]	230 (Our Work)	Spectroscopic ellipsomtery
PZT (52/48))	Nb:$SrTiO_3$ [19]	148	Spectroscopic ellipsomtery
PLT	Al_2O_3 [20]	55	Prism coupling
Organic polymers (DANS/DPB/AZB)	Glass [21]	1/2/5	Babinet-soleil compensator
PLZT (8/65/35)	Nb:$SrTiO_3$ [22]	498	Prism coupling
PZT (52/48)	$SrTiO_3$ [23]	50	Induced electro-optic Bragg grating

A spectroscopic ellipsometry based approach has been used to estimate the electric field induced birefringence, similar to the method described in previous reports [24],[25]. Our measurements are carried out with a fixed angle spectroscopic ellipsometer (J.A Woollam Co.). The ellipsometer is equipped with a broadband Xe lamp source (λ ranges from 300 nm to 1800 nm) with a rotating polarizer and analyser.

With this method it is possible to extract an effective electro-optic (EO) coefficient without the need to do the full fitting of the layer stack

parameters. However, this method has a few drawbacks. The thickness of the PZT films used for the electro-optic measurement is in the order of 1 µm, which is much larger (~ 100 nm) compared to the films characterised with lock-in detection methods [8]. When the electro-optic effects from the films are smaller, the thickness of the films needs to be increased to obtain more reliable measurements. Also, the top electrode of the samples used for the electro-optic measurements needs to be sufficiently large to contain the laser light. This could lead to an easy breakdown of the ferroelectric film. In that case, an extra good quality dielectric thin film (e.g. an ALD deposited Al2O3 thin film) is need to be deposited between the ferroelectric thin film and the top ITO contact to allow extended electro-optic measurements at high DC fields.

PZT films of thickness 800 nm have been deposited on either ITO/glass substrates or Pt/Si substrates for the EO measurements. To facilitate the ellipsometry measurements, a top transparent conductive ITO thin film of thickness 30 nm is deposited, by e-beam evaporation and subsequent heat treatment at 300°C to obtain sufficient conductivity and transparency of the ITO.

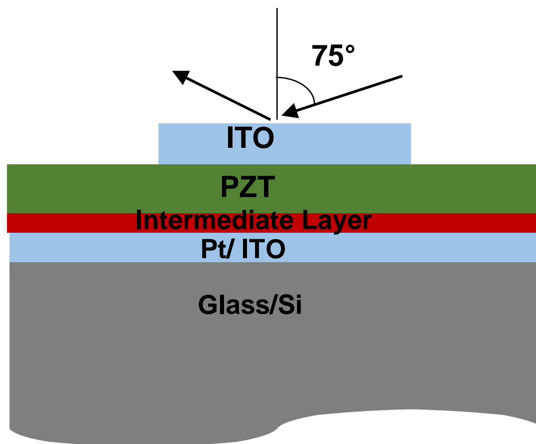

Figure 3.9: Schematic of the sample stack used for the electro-optic measurements

The PZT films are structurally characterized prior to the electro-optic measurements. The X-ray diffraction measurements show strong preferential orientation along the (100) crystallographic direction with sharp diffraction peaks corresponding to the tetragonal PZT (52/48). The SEM measurements

show well packed polygonal crystal grains, with an rms roughness of 3.1 nm as determined by AFM.

To confine the light beam required for ellipsometry completely within the electrode, the top electrode is patterned to a size of 1.5 cm x 0.5 cm using a metal shadow mask. The schematic representation of a typical sample layer stack used for the electro-optic measurements is shown in Figure 3.9. A DC voltage is applied between the top and bottom contact to introduce a change in the refractive index inside the PZT film. Note that we use a relatively large electrode size, but none of the good quality PZT films exhibited a breakdown for field strength up to 200 kV/cm.

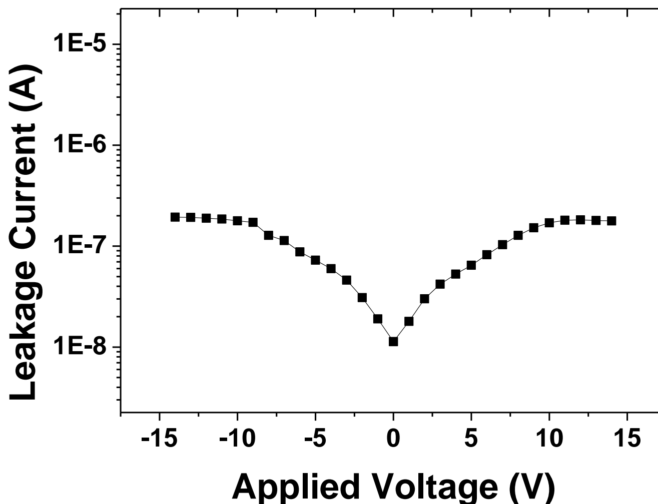

Figure 3.10: Leakage current as a function of applied voltage for PZT films annealed at 630°C on a glass/ITO substrate coated with La-based intermediate layer (heat treated at 500°C). The leakage current is measured for an electrode area of ~ 0.75 cm^2 as used for the EO measurements.

The leakage current measurement performed on the PZT film used for the electro-optic measurement is shown in Figure 3.10. We notice that the current is in the order of 0.1 μA at 150 kV/cm. Such a low power consumption allows us to conclude that a possible refractive index change by leakage current induced heating can be ignored. Moreover, the low leakage current allows the prolonged electro-optic measurements without any dielectric breakdown.

The light is incident under an angle of 75° onto the ITO (30 nm) / PZT (800 nm) / $La_2O_2CO_3$ (10 nm) / ITO / glass sample for the ellipsometry measurements. The measurement gives a value for the ellipsometric angles ψ and Δ, which are used to define the complex reflectance ratio of the p- to the s- polarized light.

$$\frac{r_p}{r_s} = \tan\psi * \exp(\mathrm{i}\,\Delta)$$

In this equation tan ψ is the amplitude reflectance ratio and Δ is the phase shift between the p- and s- polarized light after reflection. In the conventional procedure for analysing the ellipsometry data, the dielectric functions are numerically optimized for each of the layers assuming a certain dispersion relation [24].

The dielectric function of each layer arises from a fitting procedure considering the transmission, reflection and absorption of the light on all possible interfaces. However, each layer needs to be modelled very precisely to extract the small variations introduced by the application of electric fields. The optimization of the model is carried out until the residual mean square converges to the minimum. This method is very tedious in our sample structures as at least 10 parameters (n and k for each of the 5 layers) need to be optimized simultaneously.

Figure 3.11(a) represents the ellipsometry Δ angles measured for the ITO/PZT /$La_2O_2CO_3$/ITO/glass sample. The changes in Δ angle is small so it is not visible on the full, but the zoomed Δ pattern observed in the range of 639 to 641 nm (inset of Figure 3.11(a)) clearly demonstrates the changes observed in Δ. The Δ angle at a given electric field Δ(V,λ) shows a clear shift with the applied electric field, with reference to the value for Δ at 0V (Δ(0,λ)), indicating the linear EO Pockels effect from the film. To make this more visible, the variation observed in the Δ angle at three different voltages is shown in Figure 3.11(b)

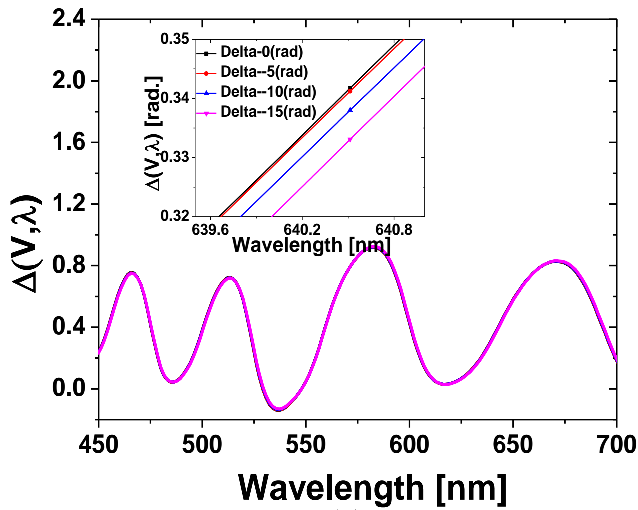

(a)

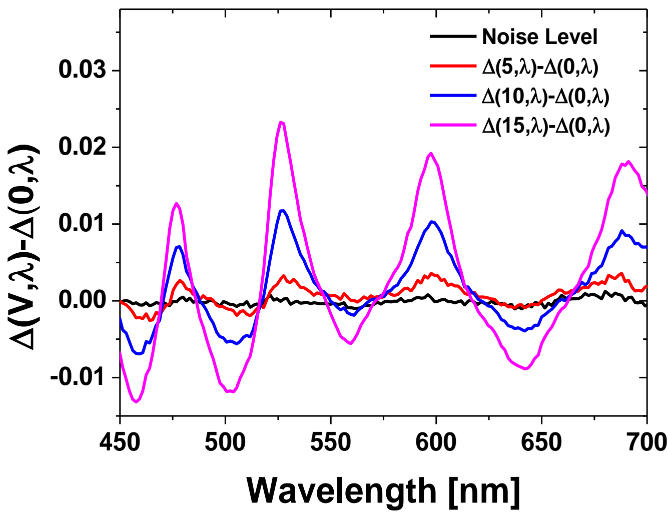

(b)

Figure 3.11: (a) Observed variation in Δ, as a function of the applied voltage (b) Change observed in Δ(V,λ)- Δ (0,λ) at 0V (Noise level) 5V, 10V, and 15V.

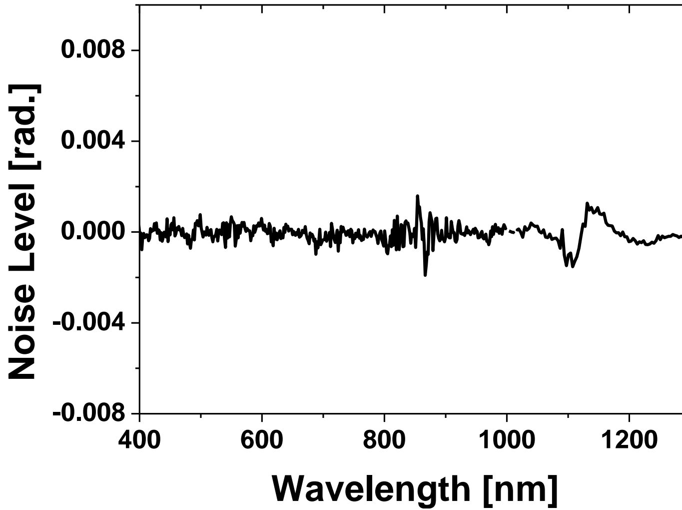

Figure 3.12: Noise level extracted from the measurements using $\Delta(0,\lambda)$- $\Delta^1(0,\lambda)$.

The noise associated with the Δ angle measurements are plotted in Figure 3.12. It is evaluated by mutually subtracting the Δ angles for two consecutive measurements. It is clear that the changes due to voltage are well above the noise level in the Δ spectrum, which confirms the electric field introduced phase change. As the variation expected in the refractive index is in the order of 10^{-3}, it is also assumed that the reflections from the different layer boundaries does not introduce any phase variations in the Δ angles with applied voltages. According to previous reports the contribution to the phase change by the thickness variation in the PZT film due to the piezoelectric effect is negligible compared to that of the refractive index change [26]. Assuming that the film possess a d_{33} piezoelectric coefficient of 300 pm/V (Highest reported on Si [27]), we can evaluate the change in the refractive index induced due to corresponding to the thickness variation [26]. For a PZT film of 800 nm thickness, the refractive index change can be calculated as $5*10^{-5}$, which is two order of magnitude smaller than the refractive index change expected from the electro-optic effect (see Figure 3.14).

It is evident from Figure 3.12 that the noise level associated with the Δ angle measurement is smaller than 0.0015 for the measurement region. The variations obtained in the Δ angle are greater than 0.0015 when applying an electric field, which confirms the electric field induced refractive index

variations. In our measurements, we found that the electric field induced variations are an order of magnitude stronger than the observed noise spectrum (see Figure 3.11(b)).

The method consists of estimating the effective wavelength change in PZT due to the change in the refractive index. To evaluate this, we differentiate the Δ angle, assuming that all other parameters except the optical permittivity tensor of (PZT) remain the same. We obtain that small changes in the effective wavelength caused by a change of the refractive index n(PZT), corresponding to small variation in the applied voltage, can be obtained using the equation [18]:

$$\Delta\lambda = \frac{\partial\Delta(\mathrm{V},\lambda)/\partial V}{\partial\Delta(0,\lambda)/\partial\lambda} * dV$$

The $\Delta\,(0,\lambda)$, $\partial\Delta(0,\lambda)/\partial\lambda$ and $\partial\Delta(\mathrm{V},\lambda)/\partial V$ spectra are plotted in Figure 3.13(a), Figure 3.13(b) and Figure 3.13(c), respectively.

$\Delta\,(0,\lambda)$ represents the ellipsomtery Δ angles obtained without applying any electric field. The $\partial\Delta(\mathrm{V},\lambda)/\partial V$ spectrum is calculated by mutually subtracting the Δ angle obtained at a certain voltage $\Delta\,(\mathrm{V},\lambda)$ to $\Delta\,(0,\lambda)$. The spectrum $\partial\Delta(0,\lambda)/\partial\lambda$ is obtained from the $\Delta(0,\lambda)$ spectrum, by calculating $\Delta(0,\lambda)$- $\Delta(0,\lambda+0.006\ \mu m)$. It is noted that the spectrum resembles the $\partial\Delta(\mathrm{V},\lambda)/\partial V$ spectrum except for the different amplitude. Since a wavelength shift of 0.006 μm corresponds to the oscillatory spectrum in $\partial\Delta(0,\lambda)/\partial\lambda$, by comparison we can extract the effective wavelength shift in the actual oscillatory function given in Figure 3.13(b).

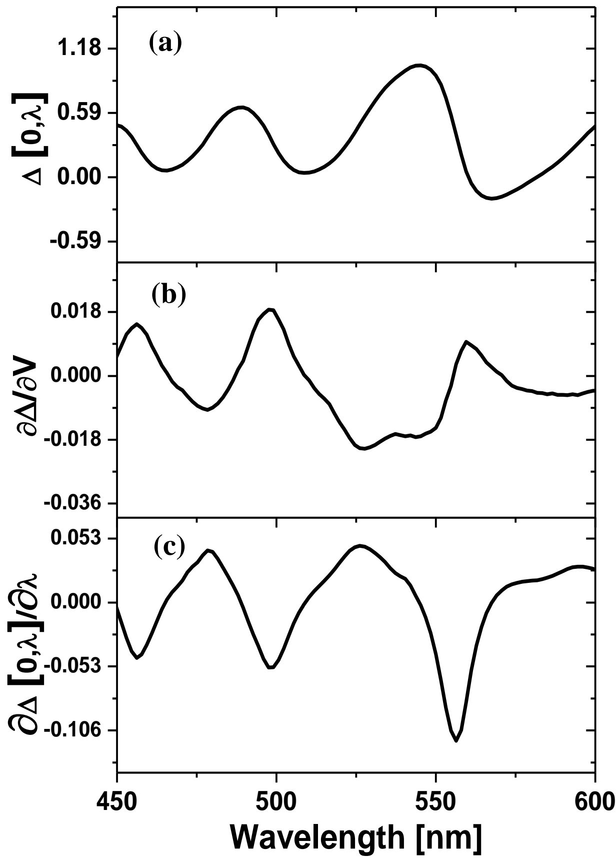

Figure 3.13: (a) Δ angle at 0 V (b) The observed variations in the Δ angle at an applied voltage $V = 15$ V, calculated by Δ (15,λ)- Δ (0,λ). (c) $\partial\Delta(0,\lambda)/\partial\lambda$.

Since the effective wavelength of the light propagating in a medium of refractive index n is given by λ/n, the change in the wavelength observed is converted to the corresponding Δn through $\Delta n = \frac{n}{\lambda}\Delta\lambda$. Finally, the effective pockels coefficient is determined from Δn, using the following equation.

$$\Delta n = -\frac{1}{2} * n^3 * r_{eff} * E$$

Where n is the refractive index, r_{eff} is the effective pockels coefficient and *E is* the applied electric field. Figure 3.14(a) and Figure 3.14(b) represent the refractive index change and the corresponding effective pockels coefficient of the PZT thin films deposited on different lanthanide based template layers with 10 nm thickness annealed at different temperature. The films possess strong effective EO coefficients. The graph indicates which annealing temperature and buffer layer properties result in the highest EO coefficient.

The PZT films annealed at 630ºC on La, Pr and Nd buffer layers exhibit a linear pockels coefficient of 240 pm/V, 215 pm/V, and 200 pm/V respectively, at the wavelength of 630 nm. The pockels coefficient of the films annealed at 560ºC are reduced to 115 pm/V, 96 pm/V and 89 pm/V for the films deposited on La, Pr and Nd intermediate layers. Even though a significant reduction in the pockels effects is observed by reducing the annealing temperature to 560ºC, the electro-optic effects of the films are still comparable to previously reported results for films annealed above 600ºC [28]. Figure 3.14(c) represents the effective pockels coefficient calculation performed for the PZT thin films deposited on La-based intermediate layers with different Zr: Ti ratios.

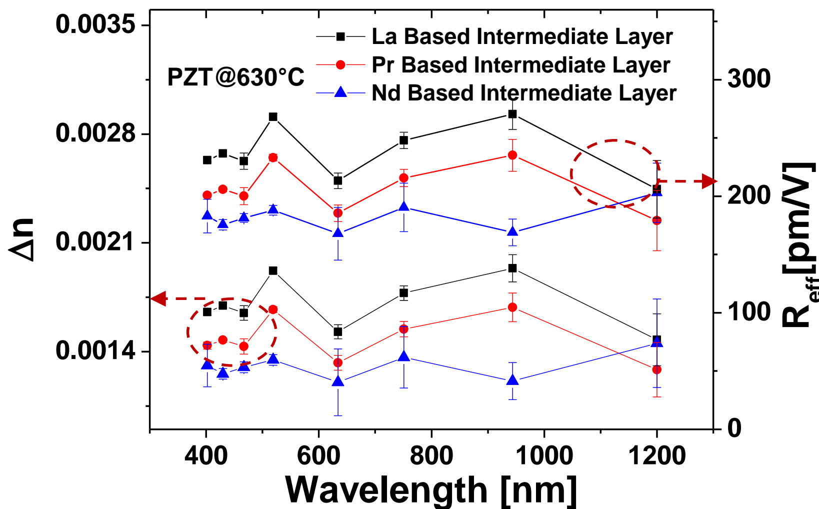

(a)

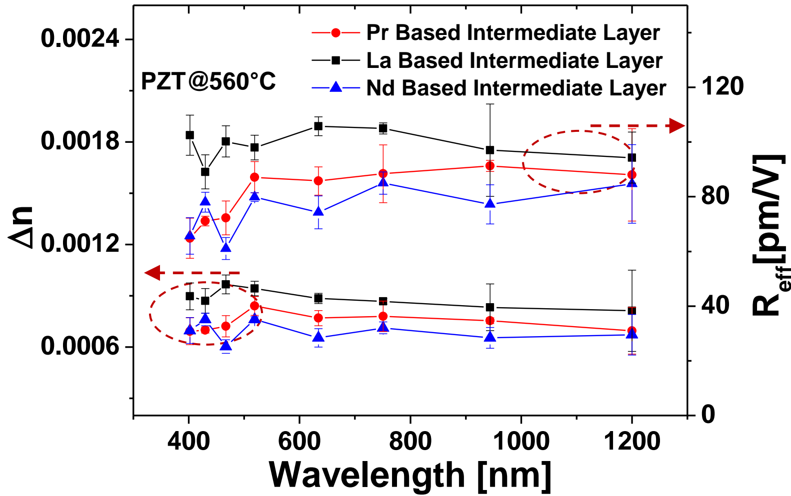

(b)

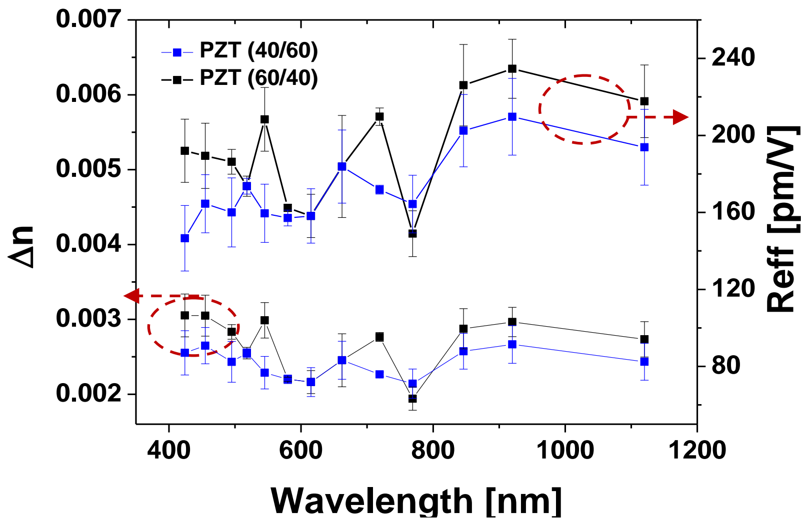

(C)

Figure 3.14: Refractive index change and the effective electro-optic coefficients of the PZT thin film (thickness ~ 800 nm) annealed at (a) 630°C (b) 560°C, on different lanthanide based template layers (c) 630°C on La-based intermediate layers, with different Zr:Ti ratios.

Strong EO effects with a slight decrease in the pockels coefficients are noticed for both tetragonal (40/60) and rhombohedral (60/40) PZT films, compared to the films deposited at MPB (52/48). The measurements shows that tetragonal PZT films with 40/60 composition possess an r_{eff} of 165 pm/V, whereas the rhombohedral 60/40 films shows an r_{eff} of 205 pm/V, at a wavelength of 720 nm, for the PZT films annealed at 630°C, on Pr-based intermediate layers. It is to be noted that the pockels coefficients for both 60/40 and 40/60 compositions are still an order of magnitude stronger to the previously reported values of 24 pm/V and 10 pm/V, for the films deposited on glass substrate with identical compositions [29].

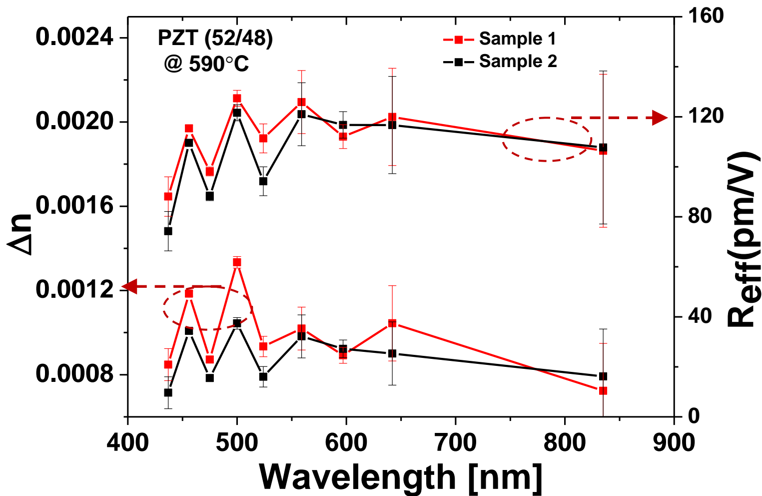

Figure 3.15: Refractive index change and the effective electro-optic coefficients of the PZT thin film (thickness ~ 800 nm) annealed at 590°C, on two different samples.

The electro-optic characterizations are performed on samples prepared under identical conditions to understand the repeatability of this experiment. Figure 3.15 represents the refractive index change and effective pockels coefficient of two PZT (52/48) samples prepared in an identical way (same thickness and annealed at the same temperature of 590°C). As we have used a thicker PZT layer (~ 800 nm) for the electro-optic measurements, the repeated spin-coating and annealing procedure introduces variations in the thickness from the center to the edge of the samples. The measurements are performed on two different samples and at two different locations. We believe that the main reason for the changes observed in our measurements are due to

variations in the thickness of the PZT layer where the measurements are performed. We also noticed a significant deterioration on the electrical and electro-optic properties of the films, if the depositions are carried out over the life time of the PZT precursor solutions. The electro-optic measurements on these samples show easy breakdown of the films due to the increased porosity.

The effective linear electro-optic coefficients (r_{eff}) measured here are comparable to previously reported values. Epitaxially grown (100) oriented PZT (52/48) thin films on a Nd:STO (100) substrate have shown an r_{eff} of 165 pm/V [24]. Masuda et.al [22] have demonstrated further improvement in r_{eff} up to 498 pm/V for an epitaxial (111) oriented PZT (52/48) thin film on a Nd.STO (111) substrate by controlling the crystal phases in the films with a modified annealing procedure and an electro-optic modulator operating at 40 GHz speed was demonstrated with this method [6]. Even though strong electro-optic properties of PZT thin films were demonstrated on different substrates, only few report on PZT-on-silicon [30].

State-of-art PZT/Si photonic devices use the piezo-electric properties of the film, to break the Si crystal symmetry and to introduce the birefringence in the Si [31],[32]. However, the change in the refractive index observed in these devices are an order of magnitude smaller compared to the electro-optics effects measured here. A comparison between the electro-optic properties of bulk ferroelectric ceramic materials, single crystalline thin films and poly crystalline thin films are provided in Table 3.4.

Table 3.4: Comparison of electro-optic properties between bulk and thin film materials.

Type	**Composition**	r_{eff} (pm/V)
Bulk ceramic	PLZT (8/65/35)	612 [33]
	PLZT (7/62/38)	523 [33]
	$BaTiO_3$	1640
Single crystalline thin films	$BaTiO_3$	213 [3]
	PLZT (8/65/35)	498 [22]
	PZT(52/48)	429 [22]

Poly crystalline thin films **(our work)**	PZT (52/48)	240 [18]
	PZT (60/40)	205
	PZT (40/60)	165

3.6 Conclusions

The electrical properties of the PZT, BTO and BZT thin films deposited with our novel deposition techniques are analysed in detail to understand the quality of the films. The films exhibits very good dielectric properties, low dielectric losses. The leakage current measurement performed indicates high breakdown electric field strength, which confirms the very good quality of the PZT films prepared by our method. The P-E hysteresis measurements demonstrate good ferroelectric properties with good remnant polarization and low coercive electric field. The good remnant polarization gives an indication on the good quality of the PZT films, while thecoercive field determines the voltage required to pole the ferroelectric thin film, when it will be used in the final electro-optic modulator. It is to be noted that the films annealed at higher temperature (630°C) exhibit superior properties, which links with the better crystallinity and improved grain sizes at higher temperature.

The electro-optic measurements are consistent with the electrical measurements, as the films deposited at higher annealing temperature exhibit higher pockels coefficients. The strong electro-optic properties of the as-deposited thin films (ranging from 120 pm/V to 240 pm/V), estimated by ellipsomtery, indicate that this PZT film is an ideal candidate for realizing nano-photonics EO modulators The results reported here as comparable to the films deposited using epitaxial thin film growth. Moreover, the novel deposition method offers a low cost and simple method to produce good quality, strongly electro-optic PZT thin films on crystalline and amorphous (SiO_2 and Si_3N_4) substrates (with quasi identical electrical and electro-optic properties)for a variety of integrated photonics and electronics applications, where the properties of the films can be tuned for applications spanning from microwave to optical frequencies.

3.7 References

1. Tang, P.S., et al., Electrooptic modulation up to 40 GHz in a barium titanate thin film waveguide modulator. Optics Express, 2004. 12(24): p. 5962-5967.
2. Wooten, E.L., et al., A review of lithium niobate modulators for fiber-optic communications systems. Ieee Journal of Selected Topics in Quantum Electronics, 2000. 6(1): p. 69-82.
3. Xiong, C., et al., Active Silicon Integrated Nanophotonics: Ferroelectric BaTiO3 Devices. Nano Letters, 2014. 14: p. 1419-1425.
4. Rabiei, P., et al., Heterogeneous lithium niobate photonics on silicon substrates. Optics Express, 2013. 21(21): p. 25573-25581.
5. Xiong, C., et al., Active Silicon Integrated Nanophotonics: Ferroelectric BaTiO3 Devices. Nano Letters, 2014. 14(3): p. 1419-1425.
6. Masuda, S., et al., Electro-optic and dielectric characterization of ferroelectric films for high-speed optical waveguide modulators. Journal of Applied Physics, 2011. 109(12).
7. Abel, S., et al., A strong electro-optically active lead-free ferroelectric integrated on silicon. Nature Communications, 2013. 4: p. 1-6.
8. Abel, S., et al., A strong electro-optically active lead-free ferroelectric integrated on silicon. Nature Communications, 2014. 4: p. 1-6.
9. Min, D., et al., The microwave dielectric properties of dual-layer PZT/ZrO2 thin films deposited by chemical solution deposition. Journal of Physics D-Applied Physics, 2011. 44(25).
10. Khaenamkaew, P., et al., Effect of Zr/Ti ratio on the microstructure and ferroelectric properties of lead zirconate titanate thin films. Materials Chemistry and Physics, 2007. 102(2-3): p. 159-164.
11. Izyumskaya, N., et al., Processing, structure, properties, and applications of PZT thin films. Critical Reviews in Solid State and Materials Sciences, 2007. 32(3-4): p. 111-202.
12. Defay, E., et al., Ferroelectric properties of Pb(Zr,Ti)O-3 thin films until 40 GHz. Applied Physics Letters, 2009. 94(5).
13. Vorobiev, A., et al., Silicon substrate integrated high Q-factor parallel-plate ferroelectric varactors for microwave/millimeterwave applications. Applied Physics Letters, 2003. 83(15): p. 3144-3146.
14. Fan, W., et al., Layered Cu-based electrode for high-dielectric constant oxide thin film-based devices. Applied Physics Letters, 2003. 82(9): p. 1452-1454.

15. Wang, Y., et al., Epitaxial ferroelectric Pb(Zr, Ti)O-3 thin films on Si using SrTiO3 template layers. Applied Physics Letters, 2002. 80(1): p. 97-99.
16. Randall, C.A., et al., Intrinsic and extrinsic size effects in fine-grained morphotropic-phase-boundary lead zirconate titanate ceramics. Journal of the American Ceramic Society, 1998. 81(3): p. 677-688.
17. Mudinepalli, V.R., et al., Effect of grain size on dielectric and ferroelectric properties of nanostructured Ba0.8Sr0.2TiO3 ceramics. Journal of Advanced Ceramics, 2015. 4(1): p. 46-53.
18. George, J.P., et al., Lanthanide-Assisted Deposition of Strongly Electro-optic PZT Thin Films on Silicon: Toward Integrated Active Nanophotonic Devices. Acs Applied Materials & Interfaces, 2015. 7(24): p. 13350-13359.
19. Kang, T.D., et al., Large electro-optic effect in single-crystal Pb(Zr, Ti)O(3) (001) measured by spectroscopic ellipsometry. Journal of Applied Physics, 2008. 104: p. 093103.
20. Boudrioua, A., et al., Electro-optic characterization of (Pb, La)TiO3 thin films using prism-coupling technique. Journal of Applied Physics, 1999. 85(3): p. 1780-1783.
21. Khanarian, G., et al., Electro-optic characterization of nonlinear-optical guest-host films and polymers. Journal of the Optical Society of America B-Optical Physics, 1996. 13(9): p. 1927-1934.
22. Masuda, S., A. Seki, and Y. Masuda, Influence of crystal phases on electro-optic properties of epitaxially grown lanthanum-modified lead zirconate titanate films. Applied Physics Letters, 2010. 96(7).
23. Busch, J.R., et al., LINEAR ELECTROOPTIC RESPONSE IN SOL-GEL PZT PLANAR WAVE-GUIDES. Electronics Letters, 1992. 28(17): p. 1591-1592.
24. Kang, T.D., et al., Large electro-optic effect in single-crystal Pb(Zr, Ti)O(3) (001) measured by spectroscopic ellipsometry. Journal of Applied Physics, 2008. 104(9).
25. Akazawa, H. and M. Shimada, Spectroellipsometric approach to determine linear electro-optic coefficient of c-axis-oriented LiNbO3 thin films. Journal of Applied Physics, 2005. 98(11).
26. Spirin, V.V., C.H. Lee, and K.S. No, Measurement of the Pockels coefficient of lead zirconate titanate thin films by a two-beam polarization interferometer with a reflection configuration. Journal of the Optical Society of America B-Optical Physics, 1998. 15(7): p. 1940-1946.

27. Kim, D.M., et al., Thickness dependence of structural and piezoelectric properties of epitaxial Pb(Zr0.52Ti0.48)O-3 films on Si and SrTiO3 substrates. Applied Physics Letters, 2006. 88(14).
28. Lee, C., et al., Drying temperature effects on microstructure, electrical properties and electro-optic coefficients of sol-gel derived PZT thin films. Thin Solid Films, 1999. 340(1-2): p. 242-249.
29. Yi, G.H., Z. Wu, and M. Sayer, PREPARATION OF PB(ZR,TI)O3 THIN-FILMS BY SOL-GEL PROCESSING - ELECTRICAL, OPTICAL, AND ELECTRO-OPTIC PROPERTIES. Journal of Applied Physics, 1988. 64(5): p. 2717-2724.
30. Kurihara, K., et al., Electrooptic properties of epitaxial lead zirconate titanate films on silicon substrates. Japanese Journal of Applied Physics Part 1-Regular Papers Brief Communications & Review Papers, 2007. 46(10B): p. 6929-6932.
31. Sebbag, Y., et al., Bistability in silicon microring resonator based on strain induced by a piezoelectric lead zirconate titanate thin film. Applied Physics Letters, 2012. 100(14).
32. Tsia, K.K., S. Fathpour, and B. Jalalia, Electrical tuning of birefringence in silicon waveguides. Applied Physics Letters, 2008. 92(6).
33. Haertlin.Gh and C.E. Land, HOT-PRESSED (PB,LA)(ZR,TI)O3 FERROELECTRIC CERAMICS FOR ELECTROOPTIC APPLICATIONS. Journal of the American Ceramic Society, 1971. 54(1): p. 1-&.

Chapter 4

Simulation of Si_3N_4 Modulator Structures

Thin film electro-optic devices attracted great attention over the last few decades and many devices have been already demonstrated on different material platforms. These EO devices rely on the Pockels effect to induce refractive index changes. In order to obtain low loss and compact designs, it is essential to use materials with strong EO coefficients. Ferroelectric thin film materials are attractive candidates because their EO coefficients are typically one order of magnitude larger than those of non-ferroelectric materials [1]. $LiNbO_3$ based external modulators are developed and used extensively in high speed, long-distance optical fiber optic communication systems. However, replacing $LiNbO_3$ with electro-optic thin films with an order of magnitude stronger electro-optic coefficients such as $BaTiO_3$, $Pb(Zr,Ti)O_3$ and $(Pb,La)(Zr,Ti)O_3$ could lead to much smaller and power efficient devices for future communication networks. Moreover, the ferroelectric thin films provide a much wider transparency window compared to Si, covering the visible region and often part of the near ultraviolet. In addition they show good thermal and mechanical stability, compared to their organic counter parts. The electro-optic coefficient of $LiNbO_3$ films are in the order of 30 pm/V [2] , whereas high EO coefficients of 145 pm/V, 150 pm/V and 370 pm/V are reported for devices based on $BaTiO_3$ (BTO) [3], $PbZrTiO_3$ (PZT) [4], $PbLaZrTiO_3$ (PLZT) [5]. Building

on such a promising material, high speed EO modulators have been realized in an integrated fashion [6].This chapter deals with the simulation, fabrication and characterization of different possible modulator structures. Different waveguide configurations have been designed taking into consideration the compatibility with the conventional UV lithography process. Simulations of the waveguide modulator structures are described in detail, based on Si_3N_4 platforms, with active PZT thin film cladding. In the second half of the chapter, we describe the fabrication strategy to realize the PZT/ Si_3N_4 modulator structure and the characterization of these devices.

4.1 Background on current Si_3N_4 based waveguide active tuning devices

Si_3N_4 based waveguides have the advantage of wide transparency and very low propagation loss from visible to near infrared wavelength range[7], [8], [9]. Heterogeneous integration of the active materials on the Si_3N_4 platform can introduce tunable devices, such as phase shifters, modulators and switches.

State-of-art tunable structures have been implemented on Si_3N_4 platform using the thermo-optic effect. However, these devices typically consume 200 to 500 mW of electrical power per modulator and exhibit a modulation speed in the range of 0.4 to 1 kHz [10]. For applications that require a large number of modulator structures, significant reduction on the power consumption to nW level is desired, where thermo-optic modulators imposes restrictions. Vescent photonics [11] demonstrated liquid crystal (LC) based phase shifters with low power consumption and modulation speeds of the devices in the order of 1 to 5 kHz.

Recent advancements on the Si_3N_4 platform were demonstrated using ferroelectric thin film materials for phase shifters [12]. However these phase shifters utilize the piezo-electric effect of the PZT films to obtain a stress-optic based tuning on Si_3N_4 waveguides. A PZT capacitor is formed on the top of a Si_3N_4 waveguide, the voltage applied across the capacitor generates stress, which changes the optical properties. Compared to the state-of-art modulator, this method produces 1 million time reduction in power consumption and 1000 time increase in the modulation speed up to 630 kHz. [12]. However, to reduce the optical loss due to the absorption from the electrodes, the capacitor structures need to be separated further away from the waveguide region by SiO_2 [12], [13], [14]. This reduces the efficiency of

these structures. Moreover, with this procedure, the much efficient and strong electro-optic properties of the films cannot be exploited. Hence there is need of new materials with stronger electro-optic coefficients and novel designs which can explore these effects for future high speed, low power devices..

With the novel processing techniques developed in our lab, we have demonstrated that ferroelectric material which exhibits strong electro-optic effects can be grown on both amorphous and crystalline substrates (see section 3.5). Our processing techniques show the PZT/PLZT/$BaTiO_3$ thin film growth directly on Si_3N_4 substrates, which can be used as an active layer cladding for tunable devices.

Since we have the technology to directly integrate these films on Si_3N_4 structures, we can utilize the electro-optic properties of the film which will result in a more efficient usage of the PZT thin film cladding.

4.2 Modulator configurations

Different modulator configurations can be designed considering the direction of the crystal/optical axis of the ferroelectric thin film and the electrode configuration. The application of the electric field in a direction parallel or perpendicular to the optical axis produces linear electro-optic effects of different magnitudes depending on the electro-optic tensor elements. The electro-optic effects modify the impermeability tensor as follows,

$$\eta_{ij} = \eta_{ij}^0 + r_{ijk} E_k$$

Where η_{ij}^0, r_{ijk}, E_k represents the unperturbed impermeability tensor, the linear electro-optic coefficient tensor and the applied electric field respectively. The coordinate indices i, j, k correspond to the x-, y- and z axis, respectively. The r_{ijk} electro-optic tensor components depend on the crystal symmetry and the crystal phases of the deposited thin films. The linear electro-optic effect is represented by a third rank tensor r_{ijk} . The permutation symmetry of this tensor is $r_{ijk} = r_{jik}$, i, j, k is 1, 2, 3. Therefore, the tensor can be represented by a 6×3 matrix, i.e, $r_{ijk} = r_{ij}$, where i is 1 to 6 and j is 1 to 3.

From the structural characterization we found that our PZT and $BaTiO_3$ films possess a 4 mm tetragonal crystal structure. The electro-optic coefficient for the 4 mm point group is given by,

$$r_{ij} = \begin{bmatrix} 0 & 0 & r_{13} \\ 0 & 0 & r_{13} \\ 0 & 0 & r_{33} \\ 0 & r_{51} & 0 \\ r_{51} & 0 & 0 \\ 0 & 0 & 0 \end{bmatrix}$$

Where the typical reported values for the r_{33}, r_{13} and r_{51} components for the PZT/$BaTiO_3$ films are 150/100 pm/V, 29/20 pm/V and 150/500 pm/V, respectively. The measurements from Chapter 2 confirm that we have highly oriented ferroelectric thin films with a strong out-of-plane orientation for the C-axis. For the simulations, we assume that the films are single crystalline with the same crystallographic orientation. Two possible modulator configuration with c-axis oriented thin films are given below.

4.2.1 Embedded electrode configuration

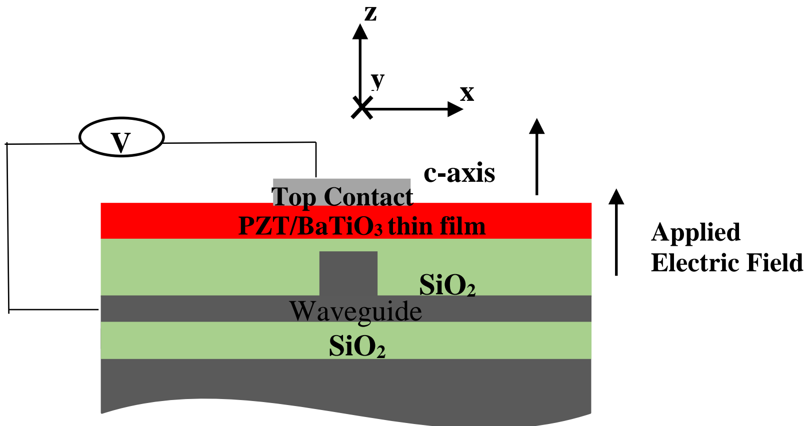

Figure 4.1: Schematic cross section of a PZT/$BaTiO_3$ based modulator with an embedded electrode configuration

The schematic of a modulator with an embedded electrode configuration system is shown in Figure 4.1 below. In order to have a bottom contact the waveguide substrate needs to be conductive (Si and Nd:$SrTiO_3$) to employ this configuration. This configuration is not applicable for Si_3N_4 waveguide, as it is an insulating substrate.

In this configuration we assume that the voltage is applied along the direction of the c-axis. At $E = 0$, the impermeability tensor is as follows,

$$r_{ij} = \begin{bmatrix} \eta_0 & 0 & 0 \\ 0 & \eta_o & 0 \\ 0 & 0 & \eta_e \end{bmatrix}$$

With the application of the electric field, the impermeability tensor is modified as given below,

$$r_{ij} = \begin{bmatrix} \eta_e + r_{13}E & 0 & 0 \\ 0 & \eta_o + r_{13}E & 0 \\ 0 & 0 & \eta_0 + r_{33}E \end{bmatrix}$$

The inverse of the impermeability tensor gives the permittivity tensor,

$$\eta = \varepsilon^{-1} = \frac{1}{\varepsilon_0 (1/n^2)}$$

An electric field applied in a general direction to a non-centrosymmetric crystal produces a linear change in the constants $(1/n^2)_i$ due to the linear electro-optic effect according to,

$$(1/n^2)_i = \sum r_{ij} E_j$$

Considering that the ferroelectric thin films have a tetragonal 4 mm crystal symmetry, using the pockels tensor as mentioned in section 4.2, the refractive index change along the x and z directions can be calculated as,

$$n_z = \sqrt{\frac{1}{\eta_e + r_{33}E}} \approx n_e - n_e^3 r_{33}$$

$$n_x = \sqrt{\frac{1}{\eta_0 + r_{13}E}} \approx n_o - n_o^3 r_{13}$$

The, the effective pockels coefficient of the device can be extracted using the following equation [6] ,

$$r_{eff} = \lambda g \Big/ n_{eff}{}^3 \Gamma V_\pi L$$

Where r_{eff} is the effective pockels coefficient, λ is the wavelength, n_{eff} is the effective mode index, g is the separation between the between the electrodes, Γ is the electro-optic overlap integral, V_π is the voltage for π phase shift, and L length of the active region.

4.2.2 Co-planar electrode configuration

The schematic of a typical co-planar electrode transverse electric (TE) modulator structure is shown in Figure 4.2. The electrodes are deposited on the top of the ferroelectric thin film separated by a small distance. With the embedded electrodes of the previous section the PZT/$BaTiO_3$ thickness needs to be above 1 µm to avoid any substantial absorption from the electrodes. However, with the co-planar configuration, we can use comparatively thinner ferroelectric thin films.

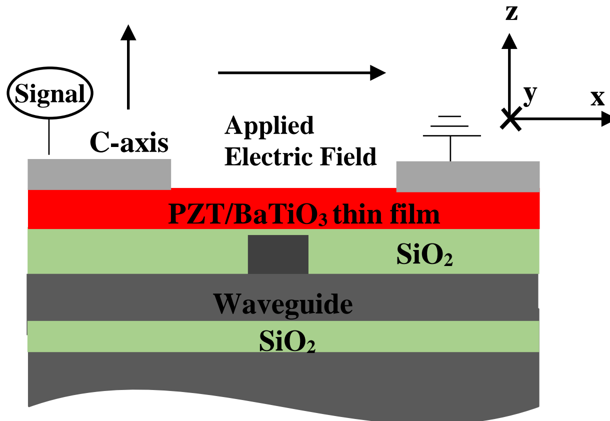

Figure 4.2: Schematic cross section of a PZT/$BaTiO_3$ based modulator (TE polarization) with a co-planar electrode configuration.

The electrodes are separated by a safe distance to avoid any absorption of the propagating mode. It is also easier to fabricate the top electrodes by a conventional UV lithography process. It is reported before that with co-planar electrodes for a c-axis out of plane oriented film, we can explore the strong r_{51} tensor component. The r_{51} value for the $BaTiO_3$ single crystalline films are reported as high as 1200 pm/V, which is about an order of magnitude stronger than the r_{33} values [6].

Approximately the applied electric field will be perpendicular to the c-axis in this configuration and as a result the permeability tensor will be modified as,

$$\eta_{ij} = \begin{bmatrix} \eta_o & 0 & r_{51}E \\ 0 & \eta_o & 0 \\ r_{51}E & 0 & \eta_e \end{bmatrix}$$

The impermeability tensor may be diagonalized by rotating over an angle ϕ about the y-axis.

$$\eta_{ij}^* = \begin{bmatrix} \eta_o + r_{51}E\tan\phi & 0 & 0 \\ 0 & \eta_o & 0 \\ 0 & 0 & \eta_e - r_{51}E\tan\phi \end{bmatrix}$$

The changes in the refractive index with applied electric field along the x and z directions as well as the rotation ϕ, result in a change in the permittivity tensor which leads to refractive index change (see section 4.2.1) as,

$$n_x^* = \sqrt{\frac{1}{\eta_o + r_{51}E\tan\phi}} \approx n_o - n_o^3 r_{51}E\tan\phi$$

$$n_z^* = \sqrt{\frac{1}{\eta_e - r_{51}E\tan\phi}} \approx n_e + n_e^3 r_{51}E\tan\phi$$

Where tan ϕ is given by,

$$\tan 2\phi = -\frac{2r_{51}E}{\eta_e - \eta_o}$$

Typically for the PZT/$BaTiO_3$ thin films the value of r_{51} is between 300 to 1200 pm/V leading to an effective r_{eff} between 200 pm/V [6] and 730 pm/V

[15]. With an optimized waveguide/ferroelectric thin film configuration, we can maximize the electrical and optical signal overlap, to obtain the maximum electro-optic effects. The maximum variation in the refractive index can be obtained at an angle of 45°, however it is possible only for higher applied electric field. Even though most of the ferroelectric materials exhibits strong electro-optic effects, in our work we focussed specifically on PZT based devices. The design of a simple modulator structure based on PZT active layer on Si_3N_4 is presented in section 4.3.

4.3 Simulation of PZT/Si_3N_4 electro optic modulators

The schematic of the standard waveguide configuration used for the simulation is shown in Figure 4.3.

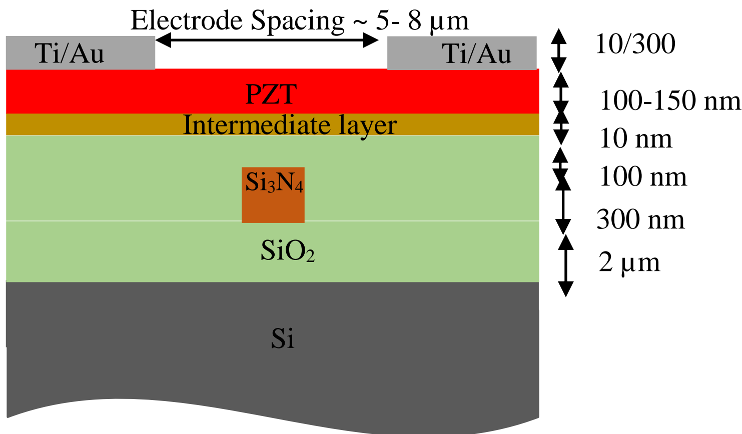

Figure 4.3: Schematic cross section of the heterogeneously integrated PZT/Si_3N_4 modulator with a co-planar electrode configuration.

The simulations carried out here are intended to optimize the PZT cladding layer thickness for minimum waveguide loss (bend loss, transition mode loss and loss introduced by the contact electrodes) and maximum confinement (to increase the electric-optical signal overlap). A standard Si_3N_4 strip waveguide (TE polarization) with a thickness of 300 nm, wavelength of 1310 nm and a width in the range between 500 nm to 2 µm has been considered for the finite element simulations. The schematic of the standard waveguide configuration used for the simulation is shown in Figure 4.3.

Simulations of the electro-optic modulation are carried out for ferroelectric films on Si_3N_4 operating at 1310 nm wavelength, considering the TE polarized light. The chip is planarized with SiO_2. We used the planarized SiO_2 cladding layer to ease the deposition of the CSD deposited PZT thin films. A thin film (100 – 150 nm) PZT layer is grown on top of the Si_3N_4 waveguide. Subsequently, the electrodes are patterned on the top of the PZT layer. The basic criteria for the design is to maximize the overlap between a driving electric field and the propagating optical mode for efficient electro-optic modulation.

The simulation flow for the design PZT/Si_3N_4 modulator is given in Figure 4.4. With an optimal design, this structure allows strong optical confinement of the propagating TE mode in the ferroelectric active layer, without considerable increase in the loss.

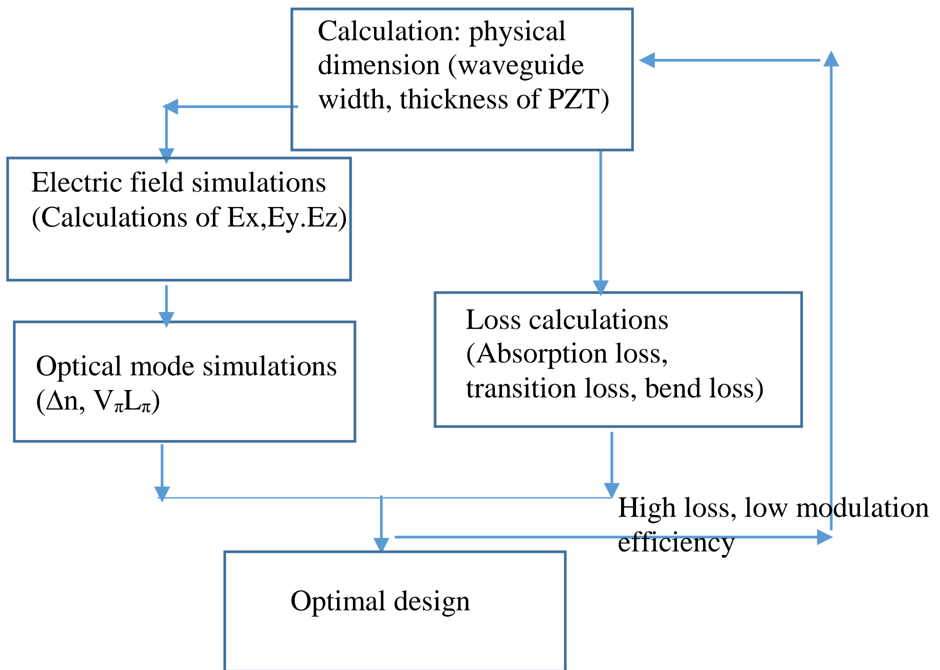

Figure 4.4: Simulation flow for the design of a PZT/Si_3N_4 waveguide modulator.

The specifications of the waveguide structures used for the simulations are mentioned in Table 4.1. A planarized Si_3N_4 waveguide fabricated with the 193 nm deep UV lithography with the following specifications is considered. We assume that a SiO_2 top passivation layer is left over the Si_3N_4 waveguide. The SiO_2 layer is planarized and has a thickness in the range of 50 to 100 nm to facilitate the deposition of the PZT thin film crystals with good conformity.

The specifications of the waveguide structures used for the simulations are mentioned in Table 4Table 4.1. A planarized Si_3N_4waveguide fabricated with the 193 nm deep UV lithography with the following specifications is considered. We assume that a SiO_2 top passivation layer is left over the Si_3N_4 waveguide. The SiO_2 layer is planarized and has a thickness in the range of 50 to 100 nm to facilitate the deposition of the PZT thin film crystals with good conformity.

Table 4.1: Waveguide specifications for simulation of PZT/Si_3N_4 modulator Structures.

Parameter	Value
Top-oxide thickness	50 - 100 nm
Si_3N_4 waveguide width	500 - 1900 nm
Si_3N_4 height	300 nm
Box oxide	2 μm
PZT thickness	100- 150 nm
Electrode spacing	5 - 10 μm
Buffer layer thickness	10 nm
r_{51}	1200 pm/V
r_{33}	250 pm/V
r_{13}	30 pm/V

Simulations of the electro-optic properties for the structure given in Figure 4.3, are carried out using the COMSOL Multiphysics FEM modules. As the first part of the simulation we calculate the static electric field distribution resulting from a voltage applied to the electrodes. This part of the simulation is performed using the electro static simulation module. Subsequently, we calculate the effective refractive index of the TE fundamental mode (@1310 nm) in the waveguide, taking into account the modified refractive index of the BTO layer due to the Pockels effect. The optical mode profile simulation

are performed using the COMSOL RF module. Including the results from the electro-static simulations, we simulate the mode profile using the anisotropic mode solver to evaluate the electro-optic properties.

4.3.1 Calculation of the confinement factor

PZT (52/48) thin films possess a refractive index of 2.4, which is larger than that of the Si_3N_4 (refractive index ~ 2) waveguide. The simulations are performed at a wavelength of 1310 nm, for TE propagating mode. In order to effectively use Si_3N_4 as the waveguide medium and avoid leakage of light, it is essential to optimize the thickness of the subsequently deposited PZT thin film. Due to the larger index of the PZT films the propagating TE mode will start interacting more with the high refractive index PZT medium if the thickness of the PZT is increased. This will result in a large transition mode mismatch loss (see section 4.3.3), electrode absorption loss (see section 4.3.2) and bend loss (see section 4.3.4).

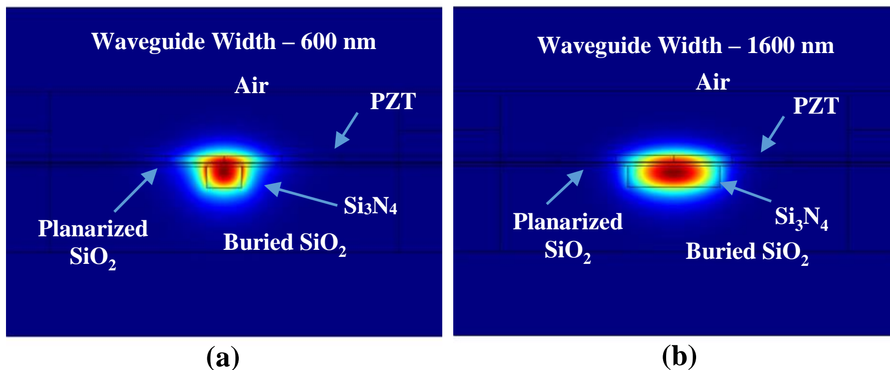

Figure 4.5: TE Guided mode profiles of a Si_3N_4/ PZT (thickness= 100 nm) heterostructure (wavelength- 1310 nm), for a top oxide thickness of 50 nm and waveguide width of (a) 600 nm (b) 1600 nm.

However, it is also essential that a sufficiently large amount of light interacts with the active PZT medium to maximally exploit the strong pockels coefficient of the PZT films. Our simulations shows that the PZT thickness needs to be in the range of 100 to 150 nm to have optimum loss characteristics, while still exploiting the strong electro-optic effect of the PZT films.

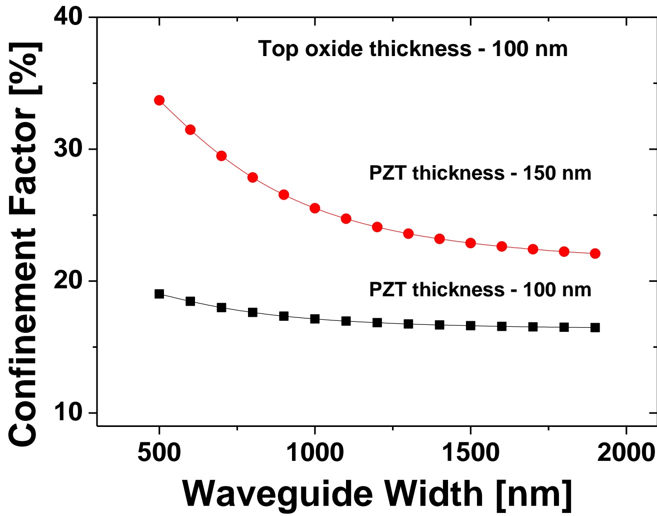

(a)

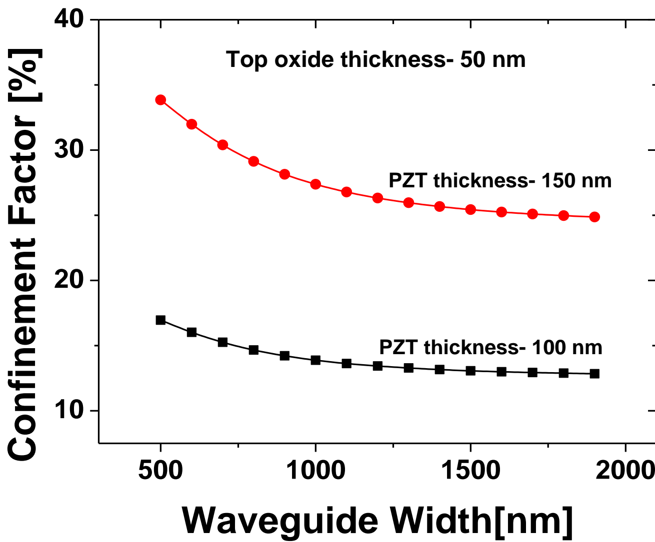

(b)

Figure 4.6: PZT confinement factor as a function of waveguide width (for TE polarization, wavelength= 1310 nm) for Si_3N_4/PZT hetero structures planarized with SiO_2 of (a) 100 nm (b) 50 nm, respectively.

Simulations are performed at λ = 1310 nm as indicated in Figure 4.6. In order to understand the interaction of the guided mode with the active PZT layer, the PZT confinement factor of the waveguides are calculated. The PZT confinement factor is defined as the fraction of the power inside the PZT layer relative to the total power of the guided mode. The confinement factor is evaluated using the following expression,

$$\text{Confinement Factor}=\frac{\int_{PZT} \mathrm{Re}(E\times H)\,ds}{\int_{Total} \mathrm{Re}(E\times H)\,ds}$$

It is clear from our calculations (see Figure 4.6(a) and Figure 4.6(b)) that waveguide width, thickness of the top planarized oxide and the PZT layer thickness are the three main parameters that influence the confinement of the light in the PZT thin film. It is evident that as the thickness of the PZT layer is increased, the evanescent tail of the guided mode interacts better with the PZT active cladding. The confinement factors are increased from 15% to 32%, for a waveguide width of 600 nm, with a top planarization of 50 nm and 100 nm respectively. However, as the waveguide width is increased the propagating TE mode is confined better into the Si_3N_4 waveguide and therefore the confinement factor is reduced from 34% to 23% for a waveguide with 100 nm top oxide, PZT layer thickness of 150 nm and a waveguide width of 500 nm, 2000 nm respectively. This variations ranges from 16% to 9.8% as the PZT thickness is reduced to 100 nm.

4.3.2 Electrode absorption loss

The simulations shows that the confinement of the optical mode in the Si_3N_4/ PZT structures is strongly influenced by the width of the Si_3N_4 waveguide and the thickness of the PZT layers. In particular, strong optical fields are observed in the PZT layers for waveguide width smaller than 700 nm.

The optical absorption originates from the interaction of the propagating electric fields with the metallic electrode is an important loss mechanism present in the modulator design. This loss becomes more pronounced when the electrodes are placed in close proximity to the waveguide. However, a small spacing between the electrodes and waveguide is desirable for the modulators, since a higher electric field can be achieved for a given operating voltage.

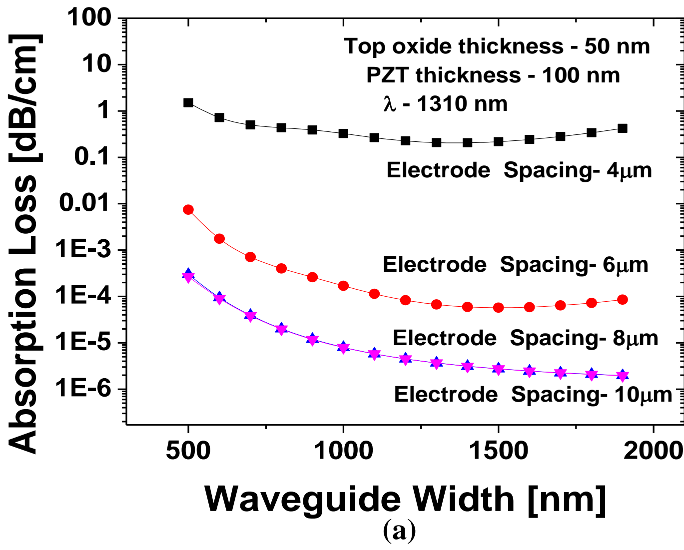

(a)

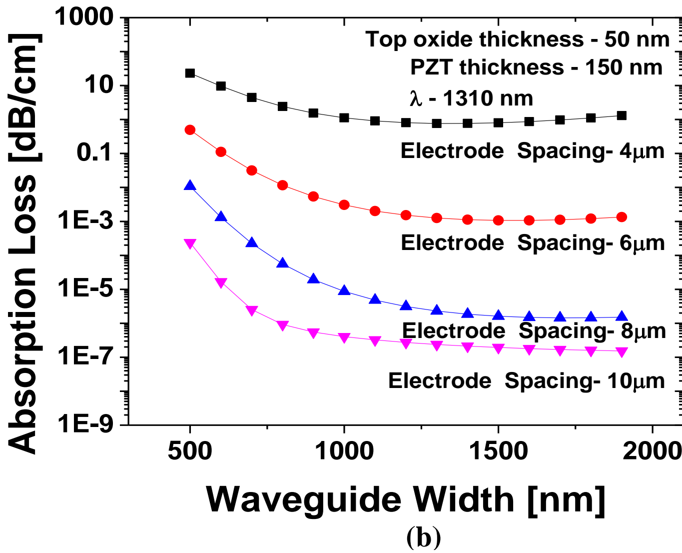

(b)

Figure 4.7: Electrode absorption loss as a function of waveguide width and electrode spacing for Si_3N_4/ PZT heterostructure (TE polarization) with a top oxide thickness of 50 nm and PZT thickness of (a) 100 nm (b) 150 nm, at λ= 1310 nm.

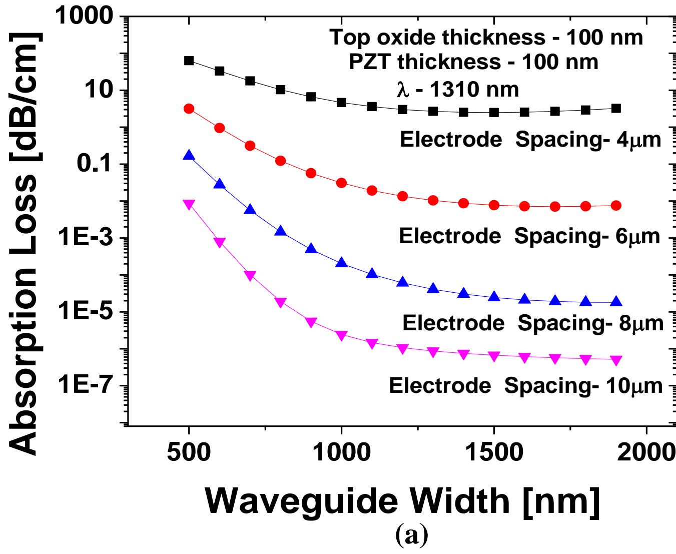

(a)

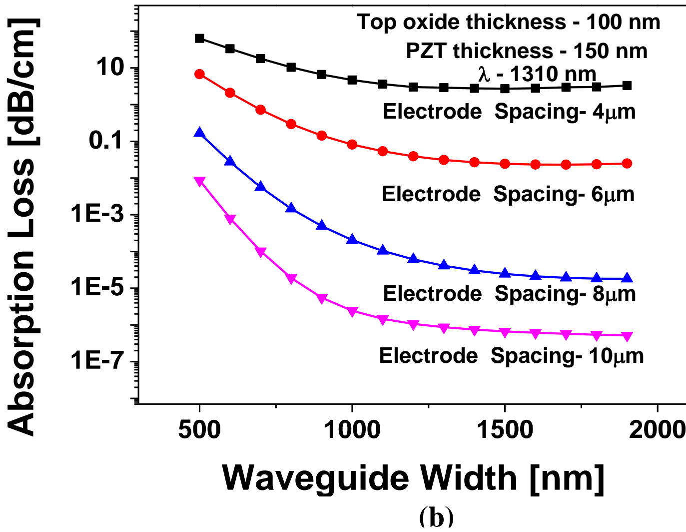

(b)

Figure 4.8: Electrode absorption loss as a function of waveguide width and electrode spacing for Si_3N_4/ PZT heterostructure (TE polarization) with a top oxide thickness of 50 nm and PZT thickness of (a) 100 nm (b) 150 nm, at λ= 1310 nm.

An optimal spacing between the electrode and the waveguide achieves both a minimal loss and a higher electric field in the PZT active layer. The calculation of the absorption loss as a function of waveguide width for a top oxide thickness of 50 nm and PZT thickness of 100 nm and 150 nm is shown in Figure 4.7. The complex refractive index of the gold electrode used for the optical simulation is n_{gold} = 0.5861+j9.862. A significant increase in the electrode absorption loss is noticed as the PZT thickness is increased from 100 nm to 150 nm. The stronger evanescent field of the propagating mode at smaller waveguide width and larger PZT thickness results in larger absorption loss.

The electrode absorption loss varies from as high as 23.05 dB/cm to 0.28 dB/cm and 1.89 dB/cm to 0.03 dB/cm, as the waveguide width is increased from 500 nm to 900 nm, for an electrode separation of 4 µm and 6 µm respectively. Any further increase in the waveguide width leads to negligible reduction in absorption loss as the TE guided mode is confined strongly to the Si_3N_4 waveguides. Figure 4.8 represents the absorption loss calculation for waveguides with top oxide thickness of 100 nm.

4.3.3 Transition mode loss

Depending on the application, it might be necessary to pattern the PZT thin films over the Si_3N_4 waveguides. For example to avoid unnecessary loss in other parts of the chip or to make sure that Si_3N_4 waveguide grating couplers perform efficiently, PZT film must be removed selectively. Our previous simulations show that PZT layer thickness, top SiO_2 thickness and the waveguide width have a crucial influence on the confinement of the light inside the PZT layer. We evaluated the overlap integral of the fundamental TE waveguide mode between etched and un-etched PZT regions to evaluate the transition loss between both regions, assuming that there are two transition regions within the device due to the selective removal of PZT before the input and output grating couplers.

The mode overlap integral is expressed as,

$$\text{Overlap Factor} = \frac{\left|\iint E1(\mathrm{x,y})\,\mathrm{E}2(\mathrm{x,y})\,\mathrm{dxdx}\right|^2}{\iint \left|E1(x,y)\right|^2 dxdy * \iint \left|E2(x,y)\right|^2 dxdy}$$

Where $E_1(x,y)$ and $E_2(x,y)$ represents the fundamental TE guided modes of the etched and un-etched PZT regions respectively.

The typical TE guided mode profile for a Si_3N_4 waveguide and Si_3N_4/ PZT heterostructure used for the overlap integral calculation are shown in Figure 4.9. As expected from the confinement factor calculations, we found that a larger mode shift occurs at lower waveguide widths and with an increase in the PZT layer thickness. Figure 4.10 represents the transition mode mismatch loss as a function of waveguide width, for different top oxide and PZT layer thicknesses.

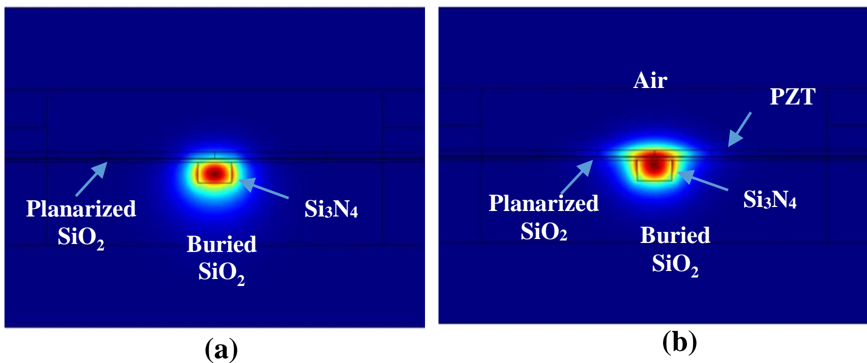

Figure 4.9: TE Guided mode profiles (wavelength- 1310 nm) of a (a) Si_3N_4 waveguide with no active PZT layer and (b) Si_3N_4/ PZT (thickness= 100 nm) heterostructure, for a top oxide thickness of 50 nm and waveguide width of 600 nm.

It is clear from our simulations that as the PZT layer thickness is increased from 100 to 150 nm, the mode mismatch loss is also increased by a factor of 2 to 3. As the PZT thickness is increased the TE propagating mode shifts upwards with a stronger evanescent field inside the PZT active layer. It is clear from our previous calculations that by decreasing the waveguide width, the confinement of the light inside the Si_3N_4 waveguides decreases for any given PZT and top oxide thickness, which further increases the mode-mismatch loss. The mode mismatch loss varies from 4.65 dB to 2.67dB for waveguide widths varying from 500 nm to 2000 nm, for a PZT layer thickness of 150 nm and top oxide thickness of 50 nm. Assuming the same top oxide thickness, as PZT thickness is decreased to 100 nm, we observe that the mode mismatch loss is decreased from 2.61dB to 1.01 dB, for waveguide width ranging between 500 nm and 2000 nm. For the design of the waveguides with a longer active regions using a meander or spiral waveguide structures, sufficient care must be taken to reduce the number of

transitions between the etched and un-etched regions over the waveguide, to reduce the mode mismatch loss. The transitions might be improved using suitable taper structures in the Si_3N_4 or in the PZT layer.

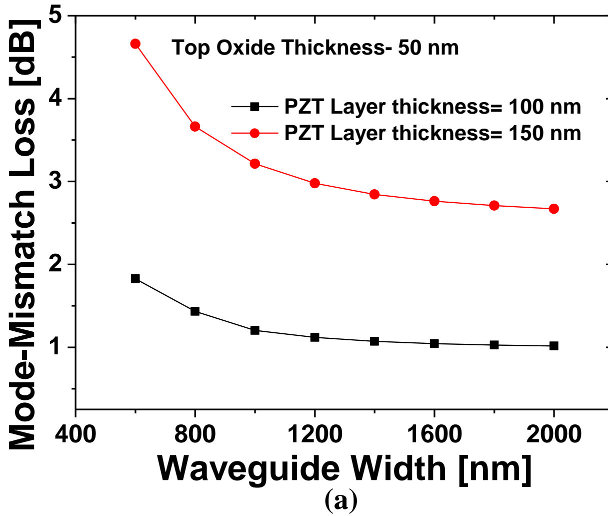

(a)

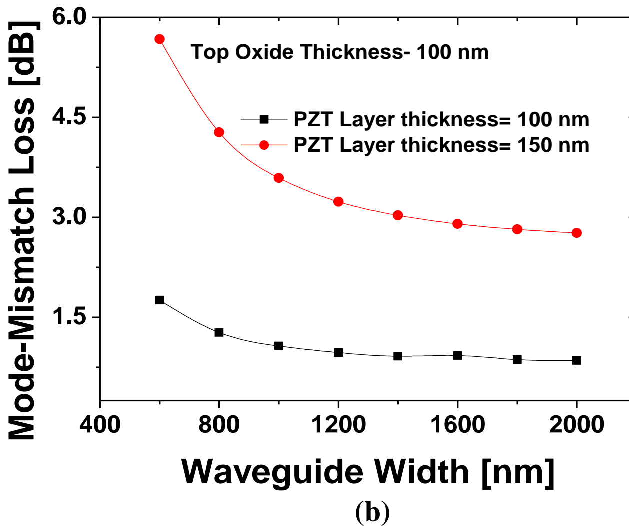

(b)

Figure 4.10: Calculation of the transition mode-mismatch loss (for a single transition) Si_3N_4/ PZT hetero-structure (TE polarization) as a function of waveguide width, PZT layer thickness and top oxide thickness, at λ= 1310 nm.

4.3.4 Bend waveguide loss

The smaller the bending radius, the more compact structures can be designed. We evaluated the bend radiation loss of the Si_3N_4/PZT heterostrucutre as a function of the waveguide width, SiO_2 thickness and PZT layer thickness as in our previous calculations. The bend losses are calculated for the waves propagating around a 180 degree bend. It is evaluated for bending radii between 20 µm and 100 µm.

Figure 4.11 represents the bend loss calculation for waveguide widths from 500 nm to 1100 nm, for a top SiO_2 thickness of 100 nm and PZT layer thickness of 100 and 150 nm respectively. For a waveguide with a width of 700 nm, a top oxide thickness of 50 nm and PZT thickness of 100 nm, the bend radiation loss is as high as 6 dB for a bend radius of 40 µm. However as the bend radius is increased to above 60 µm, bend loss reduced to below 0.1 dB. For larger waveguide width, due to the better confinement of the propagating mode, a smaller radius can be used keeping the bending loss smaller than 0.1dB. However, as the thickness of the PZT layer is increased to 150 nm, the radiation loss becomes more dominant. Even for a bend radius of 60 µm and larger waveguide width of 900 nm, the bend loss is about 10 dB. Therefore the bend radius needs to be further increased to about 90 µm to reduce the bend loss to be smaller than 0.1 dB.

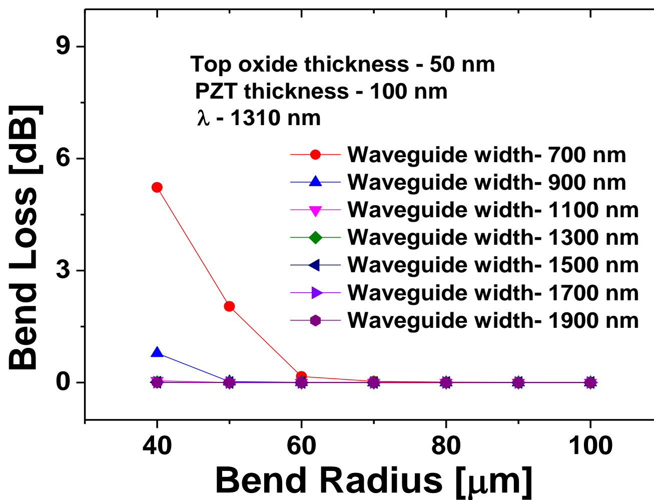

(a)

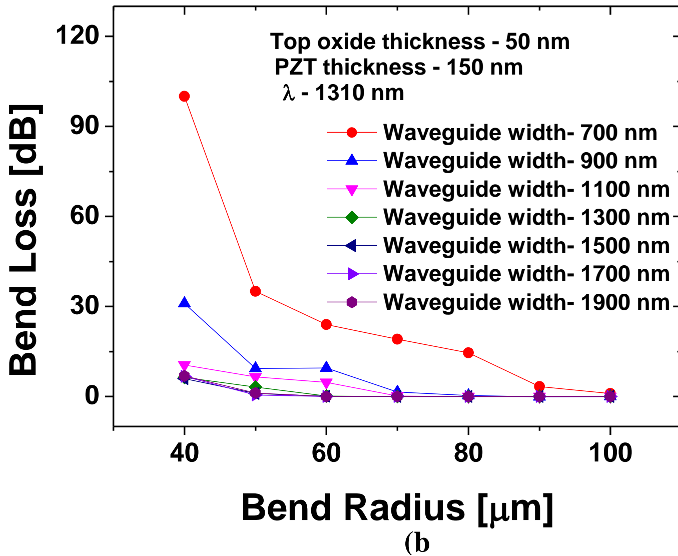

(b

Figure 4.11: Simulated bend loss (wavelength- 1310 nm, TE polarization)for a Si_3N_4/ PZT hetero structure as a function of bending radius and waveguide width, for a top oxide of 50 nm and PZT thickness of 100 nm.

4.3.5 Electro-optic simulations and evaluation of the voltage-length ($V_\pi L_\pi$) Product

One of the objectives in the development of EO modulators is the minimization of the half-wave voltage–length product ($V_\pi L_\pi$). The state-of-art Si-based depletion modulators work at about 1 V.cm, whereas commercially available $LiNbO_3$ based electro-optic modulators operate around 8 V.cm. So far one of the most direct approaches to reduce the $V_\pi L_\pi$ product is to maximize the electro-optic coefficients of the active materials. The r_{33} and r_{51} components of the recently engineered materials such as PLZT, PZT, $KNbO_3$ and $BaTIO_3$ exhibit an order of magnitude stronger (> 200 pm/V) pockels coefficients compared to the existing $LiNbO_3$ based technology. The second approach is to design more innovative waveguide geometries, so as to maximize the electrical and optical signal overlap.

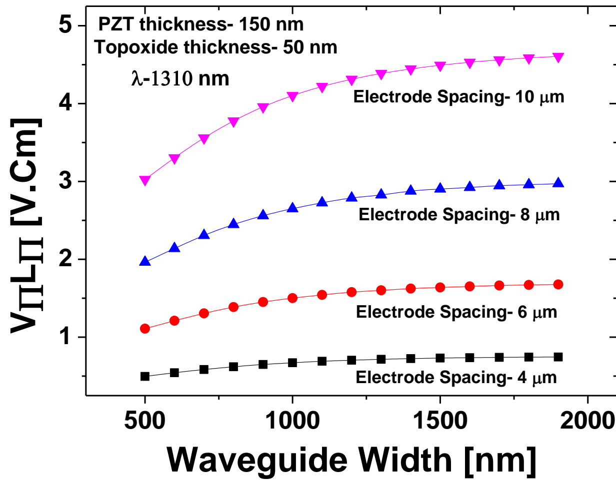

(a)

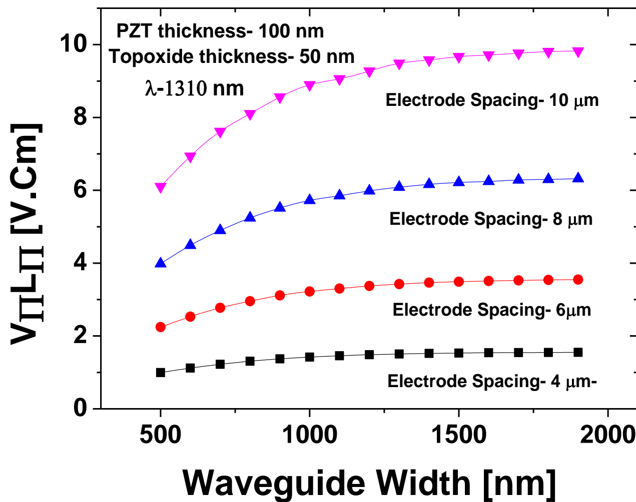

(b)

Figure 4.12: Calculation of the voltage-Length product ($V_\pi L_\pi$) for PZT on Si_3N_4 TE modulator structures with coplanar electrode configuration, with a top oxide thickness of 50 nm, at λ= 1310 nm.

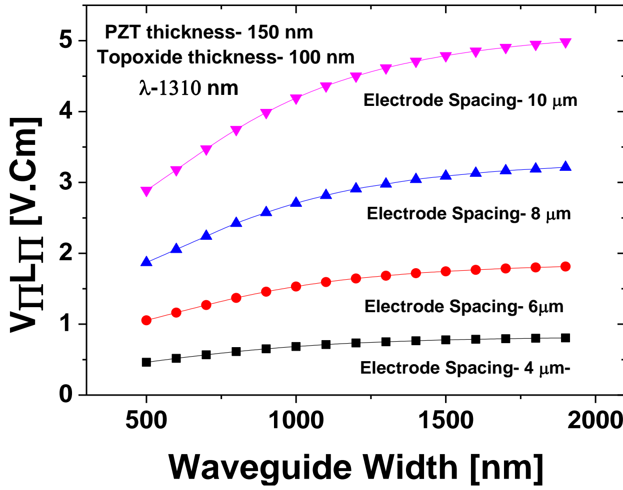

(a)

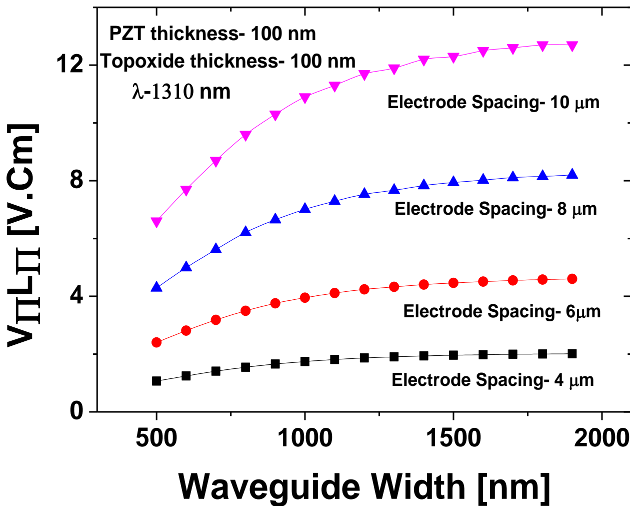

(b)

Figure 4.13: Calculation of the voltage-Length product ($V_\pi L_\pi$) as a function of waveguide width and PZT thickness for PZT/ Si_3N_4 TE modulator structure with a coplanar electrode configuration, with a top oxide thickness of 100 nm, at λ= 1310 nm.

In order to ease the fabrication process we have designed a PZT based modulator structure on Si_3N_4 waveguides with co-planar electrode configurations. With this approach, the electrode contacts can be fabricated over the Si_3N_4 waveguides using a conventional UV lithographic process, as m)the electrode contact is in the order of a few µm. The simulations are carried out considering all the possible parameters such as waveguide width, PZT thickness, top oxide thickness, electrode spacing to achieve maximum overlap between the driving electric field and the propagating electro-magnetic field. Our objective is to achieve a maximum change in the effective refractive index of the propagating mode at a given voltage, while keeping the propagation loss sufficiently low. The details of the co-planar waveguide structure and the simulation parameters are mentioned in Figure 4.3 and Table 4.1, respectively. The values of electro-optic coefficients are taken as 250 pm/V, 30 pm/V and 1200 pm/V, for r_{33}, $r_{13,}$ r_{51} respectively, for identical orientation and configurations.

Figure 4.12 represents the $V_\pi L_\pi$ calculation for the PZT/Si_3N_4 heterostructure, as a function of waveguide width and distance between the electrodes, for a top oxide thickness of 50 nm, at λ= 1310 nm. The $V_\pi L_\pi$ values varied from 1.1 V.cm to 1.67 V.cm and 2.24 V.cm to 3.54 V.cm as the waveguide width increases from 500 nm to 2 µm (electrode spacing- 6µm), for a PZT layer thickness of 150 and 100 nm respectively. A decrease in the confinement factor of the propagating mode inside the PZT films at higher waveguide width results in an increase of the $V\pi$ $L\pi$ product. With an increase in the electrode spacing from 4µm to 10 µm, the electric field inside the PZT layer is strongly scaled and results in an increase in the $V_\pi L_\pi$ product. It increases from 0.49 V.cm to 0.74 V.cm and 3.02 V.cm to 4.06 V.cm for a top oxide thickness of 50 nm, waveguide width of 700 nm, for an electrode spacing of 4 µm and 10 µm, respectively.

Figure 4.13 represents the $V_\pi L_\pi$ calculation for a top SiO_2 thickness of 100 nm. An increase in the thickness of the top oxide layer decreases the confinement of the light inside the PZT active layer. It is noticed that for a width of 700 nm, PZT thickness of 150 nm and electrode spacing of 6 µm, the $V_\pi L_\pi$ product has increased from 1.27 V.cm to 1.35 V.cm. It is noticed from Figure 4.12 and Figure 4.13 that the variations in the $V\pi L\pi$ product with an increase or decrease in the waveguide width is much more dominant as the PZT layer thickness is increased. It is due to the strong variations of the confinement factor with the thicker PZT layers. For an electrode spacing of 6 µm, top oxide thickness of 100 nm and PZT thickness of 100 nm and

150 nm the $V_\pi L_\pi$ product is varied from 1.05 V.cm to 1.74 V.cm and 2.2 V.cm to 4.46 V cm or waveguide width of 500 nm and 1500 nm respectively.

4.4 Conclusions

We proposed a simple design to develop compact TE electro-optic modulators on the Si_3N_4 platform, with ferroelectric thin films. Apart from the devices reported before based on piezo-electric effects [12], we have shown waveguide structures which can utilize the strong electro-optic properties of the PZT/$BaTiO_3$ thin films.

From our simulations, a modulator based on a co-planar electrode system is found as an ideal configuration for PZT/Si_3N_4 hybrid modulators. For TE polarization, with our c-axis out-of-plane oriented PZT films, the co-planar electrodes explore the strong r_{51} tensor element for the electro-optic effects. Moreover, such an electrode system also benefits from the ease of fabrication by conventional UV lithography. This waveguide structure has the advantage that the loss and electro-optic properties can be controlled precisely through the growth of the PZT layer. The thickness of the ferroelectric thin film is designed to use Si_3N_4 as an effective waveguide medium. Following our simulation results, the length of the modulator can be reduced by increasing the thickness of the PZT layer and reducing the thickness of the waveguide thickness. However, an optimal design needs an agreement between modulation efficiency and associated losses. With our design, modulators with $V_\pi L_\pi$ less than 1 V.cm is possible, for structures with Si_3N_4 waveguides of width less than 1 µm, Si_3N_4 thickness of 300 nm, PZT thickness of 150 nm and electrode spacing of 6 µm and a waveguide loss less than 2 dB/cm.

4.5 References

1. Nagata, T., et al., Electro-optic effect in ZnO : Mn thin films. Journal of Alloys and Compounds, 2004. 371(1-2): p. 157-159.
2. Akazawa, H. and M. Shimada, Spectroellipsometric approach to determine linear electro-optic coefficient of c-axis-oriented LiNbO3 thin films. Journal of Applied Physics, 2005. 98: p. 113501.
3. Abel, S., et al., A strong electro-optically active lead-free ferroelectric integrated on silicon. Nature Communications, 2014. 4: p. 1-6.
4. Kang, T.D., et al., Large electro-optic effect in single-crystal Pb(Zr, Ti)O(3) (001) measured by spectroscopic ellipsometry. Journal of Applied Physics, 2008. 104: p. 093103.
5. Masuda, S., A. Seki, and Y. Masuda, Influence of crystal phases on electro-optic properties of epitaxially grown lanthanum-modified lead zirconate titanate films. Applied Physics Letters, 2010. 96: p. 072901.
6. Xiong, C., et al., Active Silicon Integrated Nanophotonics: Ferroelectric BaTiO3 Devices. Nano Letters, 2014. 14: p. 1419-1425.
7. Romero-Garcia, S., et al., Silicon nitride CMOS-compatible platform for integrated photonics applications at visible wavelengths. Optics Express, 2013. 21(12): p. 14036-14046.
8. Subramanian, A.Z., et al., Near-Infrared Grating Couplers for Silicon Nitride Photonic Wires. Ieee Photonics Technology Letters, 2012. 24(19): p. 1700-1703.
9. Subramanian, A.Z., et al., Low-Loss Singlemode PECVD Silicon Nitride Photonic Wire Waveguides for 532-900 nm Wavelength Window Fabricated Within a CMOS Pilot Line. Ieee Photonics Journal, 2013. 5(6).
10. Roeloffzen, C.G.H., et al., Silicon nitride microwave photonic circuits. Optics Express, 2013. 21(19): p. 22937-22961.
11. Davis, S.R., et al., A New Generation of Previously Unrealizable Photonic Devices as Enabled by a Unique Electro-Optic Waveguide Architecture, in Liquid Crystal Xii, I.C. Khoo, Editor. 2008, Spie-Int Soc Optical Engineering: Bellingham.
12. Hosseini, N., et al., Stress-optic modulator in TriPleX platform using a ezoelectric lead zirconate titanate (PZT) thin film. Optics Express, 2015. 23(11): p. 14018-14026.
13. Tsia, K.K., S. Fathpour, and B. Jalalia, Electrical tuning of birefringence in silicon waveguides. Applied Physics Letters, 2008. 92: p. 061109.

14. Sebbag, Y., et al., Bistability in silicon microring resonator based on strain induced by a piezoelectric lead zirconate titanate thin film. Applied Physics Letters, 2012. 100(14).
15. Petraru, A., et al., Ferroelectric BaTiO3 thin-film optical waveguide modulators. Applied Physics Letters, 2002. 81(8): p. 1375-1377.

Chapter 5

Fabrication and characterization of waveguide electro-optic devices

With the optimized design parameters as described in the previous chapter, electro-optic devices are fabricated and characterized on the Si_3N_4 waveguide platform. First, a brief description of the fabrication process is provided. The PZT layers are synthesized with precise thickness control, to achieve minimum loss and maximum electro-optic overlap as found by the simulations. During my thesis also a reactive ion etching (RIE) process is developed and optimized to selectively remove the PZT layer. Subsequently, the fabricated devices are DC characterized.

The DC measurements demonstrate the strong electro-optic properties of the PZT films, as expected from the thin film measurements in section 3.5. The $V_\pi L_\pi$ product is comparable to state-of-the-art ferroelectric thin film based electro-optic devices. The waveguide losses obtained for the PZT/Si_3N_4 heterostructure are comparable to that of the best reported results.

5.1 Fabrication of Si_3N_4/PZT electro-optic devices

The Si_3N_4/PZT heterostructure electro-optic devices designed in Chapter 4 are fabricated in the UGent cleanrooms using a number of deposition steps for the different layers, UV lithography and etching steps. In the following sections we will explain the fabrication procedure in detail. Special attention will be devoted to the cleaning procedure, the ferroelectric thin film deposition, reactive ion etching (RIE) of the ferroelectric thin film, lithography and metallization. The schematic representation of the fabrication steps for Si_3N_4/PZT electro-optic devices is shown in Figure 5.2.

5.1.1 Need for planarization

As described in section 2.6.2.5 the conformity associated with the spin coating of the intermediate layer and PZT precursor solution is a challenge on structures with large step height (above 50 nm). The spin coating of thinner intermediate layers of 15 nm results in considerable non-uniformity. It is observed that subsequent deposition of PZT and BTO layers over this intermediate layer results in micro cracks, pyrochlore intermediate phase formation and fresnoite silicate formation. In order to overcome this problem, we can either use devices with smaller step height or planarize them with SiO_2. In this work the latter approach was followed.

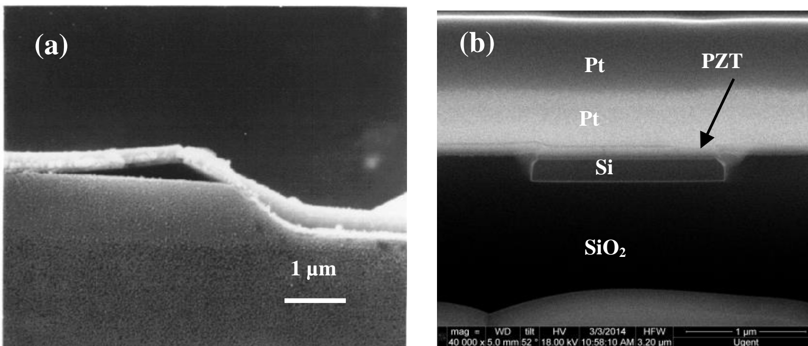

Figure 5.1: (a) Example from literature: PZT films coated on a pattered SiO_2 film. The SiO_2 film was formed on a Si substrate by wet oxidation and patterned to a 1 µm step by wet etching (source: [1]) (b) Our deposition: planarized Si waveguide with intermediate layer and PZT layer on top.

Standard Si_3N_4 waveguides from imec, with a step height of 300 nm are used for our applications. The dies contain spiral waveguides for loss

characterisation and symmetric Mach-Zehnder Interferometers with different waveguide widths. All devices are connected to grating couplers for coupling light on and off the chip.

An example of the PZT coating on a planar and a non-planar structure is provided in Figure 5.1. The conformity issues associated with the spin coating of PZT film over a large etch step is clear from Figure 5.1(a)[1]. However, in our work, a SiO_2 layer is deposited over the Si_3N_4 waveguides by PECVD and planarized by chemical mechanical polishing (CMP) to a thickness of 50 to 100 nm. This facilitates the easy deposition of the intermediate layer and ensures the quality of the PZT layer, with well packed crystal grains and without cracks, as described in 2.6.3. The example FIB cross-section of a Si waveguide planarized with SiO_2 is given in Figure 5.1(b). The arrow point towards the PZT layer deposited over the SiO_2 by CSD and the top Pt layers are deposited to prevent the damages to the device during focussed ion beam (FIB) etching.

5.1.2 Sample cleaning

When they arrive, the samples are coated with protective photoresist to avoid damage to the devices. The samples are first cleaned in acetone with an ultrasonic agitation for 5 minutes to remove the photoresist. In the next step, samples are cleaned in iso-propanol in an ultrasonic bath, followed by the final cleaning in running deionized (DI) water. Finally, the samples are dried in an oven at 100°C for 15 minutes, before proceeding to the ferroelectric thin film deposition.

5.1.3 Ferroelectric thin film preparation

In order to have accurate control over the PZT thickness, a precursor solution of 0.3 M is prepared, following the method described in 2.4. La-based intermediate layers are used in this experiment, as it results in layers with the highest pockels coefficients. First, the intermediate layer is spin coated and heat treated at 500°C. Subsequently, the PZT layer is spin coated and heat treated on a hot plate at 300°C. The thickness of the PZT layers upon each spin coating and annealing step is estimated to be in the range of 37 to 45 nm (measured with an ellipsometer). The process of PZT spin coating and heat treatment is repeated 3 times to achieve the desired layer thickness, before annealing the sample in a tube furnace at 630°C. This results in a total PZT thickness of about 130 nm. We have carried out an

XRD and SEM measurement on these samples, which confirm the expected strong preferential growth of the PZT thin film.

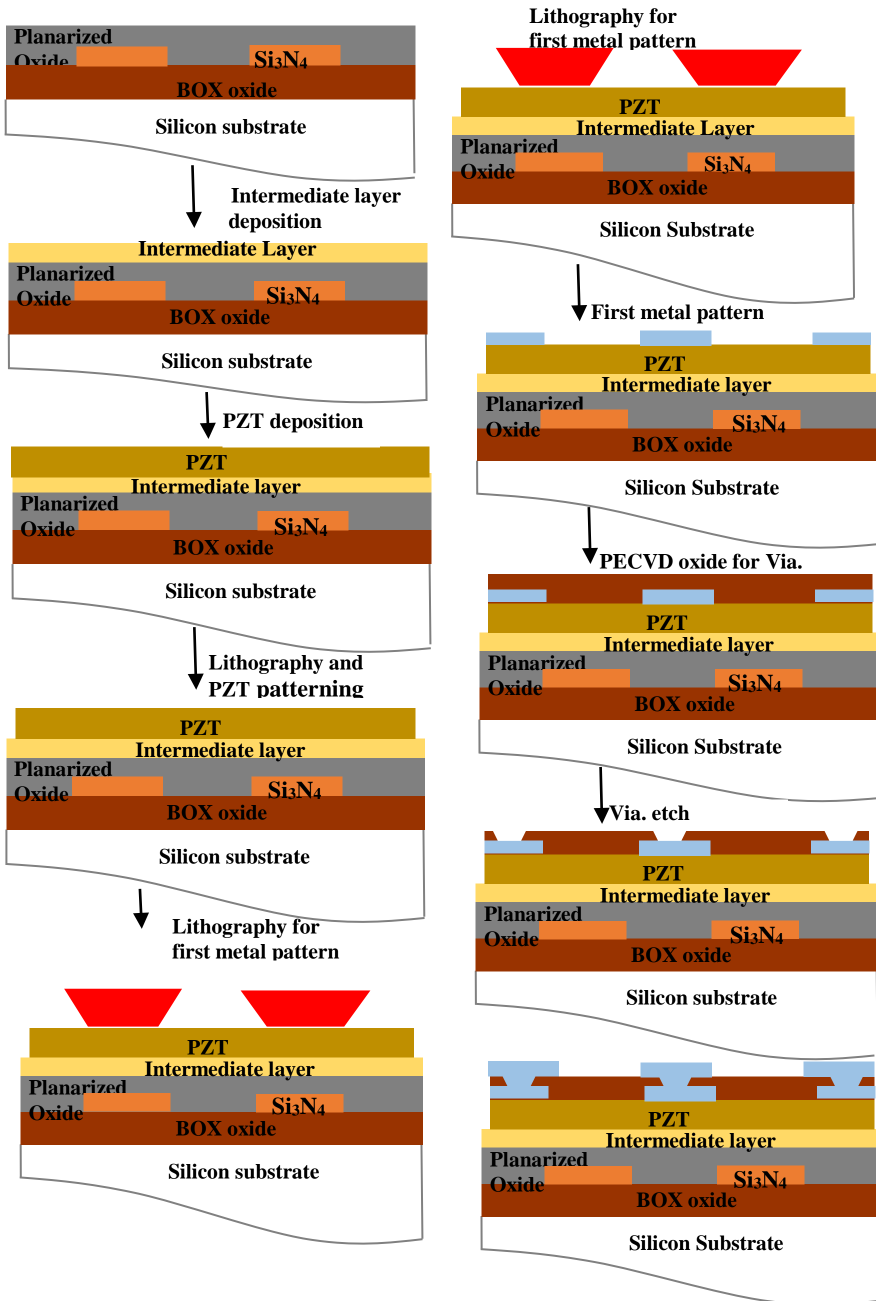

Figure 5.2: Fabrication procedure for PZT/ Si_3N_4 electro-optic devices

5.1.4 Lithography

Lithography and dry or wet etching is used to define a patterns on a substrate. During lithography a light sensitive organic polymer is spin coated onto the sample surface to form a thin layer. This resist is then exposed selectively by shining UV light through a mask, which contains the desired pattern. In our work, we used two types of photo resist: AZ 9260 and AZ 5214 (MicroChemicals GmbH, UK) depending on the type of pattern to be transferred. AZ 9260 is a typical positive photoresist, where the region exposed through the Cr metal mask can be removed by a water based solution, thereby transferring the exact pattern as in the Cr metal mask. This is used a first time for patterning the PZT layers over the waveguide. Before applying the resist, first TI PRIME adhesion promoter (MicroChemicals GmbH, UK) is spin coated at 3000 rpm for 40 seconds followed by prebaking the sample at 120°C for 3 minutes. Secondly, the photoresist is spin coated at 5000 rpm for 40 seconds and prebaked at 110°C. The sample is then exposed for 100 seconds through the chrome mask in a MA6 mask aligner and the photoresist is developed in a 1:3 solution of AZ400:DI water for 2 minutes. We post bake at 120°C for 2 minutes, before using the photoresist mask for the etching process. This etching process will be described in a following section.

The positive photoresist produces a positive slope, which makes it hard to use it a for metal deposition and lift-off process. Using such a pattern, the sidewalls of the resist would be covered with the deposited material, which makes it hard to lift-off the metal layer. Therefore, we used AZ 5214 as a lift-off photo resist. It is a negative photoresist, which is commonly used for lift off. The negative resists are designed to facilitate lift-off processes by attaining a reproducible undercut. Such an undercut helps to prevent the resist sidewalls from being coated, which makes the subsequent lift-off easier. We used the lift-off resist to transfer the metal pattern onto the PZT thin films. First, AZ 5214 photoresist is spin coated at 3000 rpm for 40 seconds, followed by prebaking at 100°C for 3 minutes. Then, the resist is exposed through a photomask in an MA6 mask aligner for 12 seconds and post baked on a hot plate at 120°C for 3 minutes. The samples are then flood exposed (exposure without mask) for 50 seconds, to get the desired features upon developing the photoresist. Finally, the samples are developed in a standard photoresist developer AZ400 (MicroChemicals GmbH, UK) diluted in DI water at 1:4 ratio for 32 seconds.

5.1.5 Etching of PZT thin film

In order to transfer the desired pattern into the PZT thin film we used the hard baked photoresist as a mask on the PZT thin film. The patterns are formed by selectively etching the PZT thin film. Etching of the PZT film can be either wet or dry. The wet etching procedure uses a liquid etchant, which usually produces fairly smooth sidewalls. The etchant can be very selective, however the wet etching results in an isotropic etch profile with no directionality.

PZT wet etching is rather difficult. A number of PZT etchants use hydrofluoric acid in different combinations with ammonium fluoride (NH_4F) and/or hydrochloric acid (HCL) [2], [3]. One of the disadvantages of these etchants is the non-selectiveness towards the planarized oxide layers. HF for example etches SiO_2 much faster than the PZT film. Since the PZT layer thicknesses for our application are rather small, wet etching is not a good option for PZT pattering. Nevertheless, wet etching of PZT is widely used for MEMS applications [4] where the Pt bottom electrode is used as an excellent etch stop layer as it is very selective to etchants involving HF.

Plasma etching (dry etching) can be highly directional. In a plasma system the etching can be physical, chemical or a mixture of both. A high electric field is generated inside the plasma chamber with an RF generator operating at 13.56 MHz. Depending on the mixture of gases used, some gases undergo ionization to produce electrons and ions. Due to the difference in their mobility, after few cycles electrons get accumulated near the electrodes, hence a voltage bias develops between the plasma and the electrodes. The voltage bias accelerates the positive ions towards the electrode resulting in physical etching. In a plasma system, free radicals present inside the chamber result in chemical etching whereas the ions result in highly directional etching due to the physical bombardments. The type of mixtures used, the flow rate, the pressure inside the chamber and the RF power are the parameters, which can be used to control the etching rates and etch profiles.

Many studies have reported on the etching of PZT films using different dry etching methods, including reactive ion etching (RIE), magnetically enhanced reactive ion etching (MERIE), and high-density plasma etching, such as electron cyclotron resonance (ECR) and inductively coupled plasma (ICP) etching. The etch process uses various gas mixtures, which are mostly based on either chlorine or fluorine [5], [6], [7], [8] chemistry. In general, chlorine chemistries show much faster etching than fluorine chemistries,

while the etch profiles can vary depending on the etching conditions. On the other hand, chlorine chemistries generally exhibit clean etch profiles, but the selectivity towards the photoresist mask is poor compared with the fluorine chemistries. We used initially the CHF_3/Ar based chemistry for etching the CSD deposited PZT films. The results of these experiments are summarized in Table 5.1.

Table 5.1 : PZT dry etching with CHF_3/Ar plasma

Etching gas (CHF_3/ Ar)	Pressure	Power	Etch rate
30/10 sccm	30 mTorr	100 W	2 nm/minutes
30/10 sccm	30 mTorr	400 W	0.5 nm/min
10/30 sccm	15 mTorr	100 W	50 nm/minutes
10/30 sccm	15 mTorr	400 W	150 nm/minutes

With flow rates of the gases CHF_3/Ar controlled to 30/10 sccm (standard cubic centimeters per minute), pressure 30 mTorr and RF power of 100 W, the etch rate of the PZT film is limited to 2 nm/min. With the CHF_3/Ar ration above 1, we believe that the etching of the PZT film is dominated by chemical etching rather than physical sputtering. It is reported that chemical etching of PZT is limited by the formation of non-volatile etch products such as PbF_2 and ZrF_4 [7]. Therefore, a combination of physical etching with the chemical etching is essential to remove the reaction by-products. The physical removal of the material can be enhanced by either decreasing the pressure or by increasing the power.

To increase the etch rate of the film we increase the RF power from 100 W to 400 W. However, this unexpectedly results in a decreasing etch rate of the films. We believe this decreasing etch rate originates from carbon contamination from the CHF_3 gas (observed as a thin black layer over the sample), where carbon acts as an inhibitor preventing further etching. When the flow rate of the gases is changed to 10/30 sccm for CHF_3/Ar at 15 mTorr and 100 W, as expected an increase in the etch rate to about 50 nm/min was observed. The etch rate is increased further by increasing the RF power to 400 W. However, it is to be noted that the surface roughness of the films also

increases rapidly. This happens due to an increased physical removal of the PZT material at low power and increased Ar concentration. Therefore we switched to an etching chemistry relying on pure SF_6 gas for the PZT films. With a flow rate of 30 sccm, pressure 15 mTorr and power 150 W, we obtained an etch rate of 8 nm/minute. The etched surface looks smooth indicating that the etching with pure SF_6 is more chemical. Figure 5.3 shows a SEM image of the patterned waveguide sample.

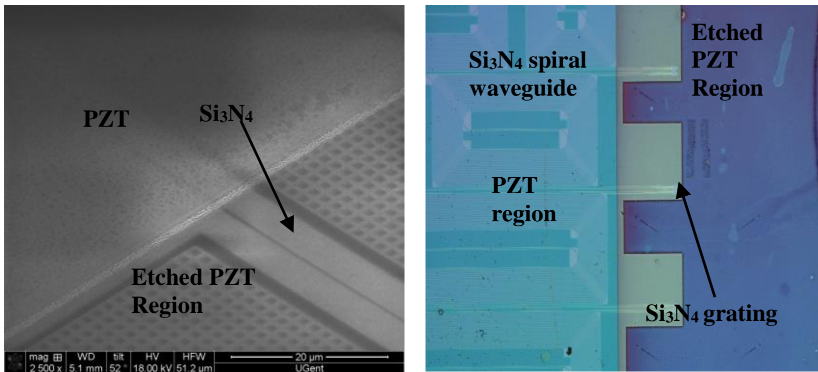

Figure 5.3: (a) SEM image of the Si_3N_4/PZT waveguide patterned by RIE with a CF_4 based chemistry. (b) Microscope image of the patterned Si_3N_4/PZT spiral waveguide used for loss measurements.

5.1.6 Metal contact and oxide etching

After patterning of the PZT layer and lithography with a lift-off resist, the first metallization of the samples is carried out in an e-gun evaporation system. A Ti/Au layer is used as the metal contact for the PZT thin films. A thin layer of Ti (about 15 nm), is deposited to improve the adhesion of the thick Au layers (thickness ~ 300 nm). It is noticed that as the evaporation rate of the Au is increased above 2 Å/second, the adhesion of the gold layer to the PZT film is rather poor. These layers are also damaged easily upon contact with the measurement probes. When using a deposition rate less than 1 Å/second the adhesion of the Au layers to the PZT film improves drastically. As the mach-zehnder phase shifter arms are separated by only 40 µm, we used a PECVD oxide of 1.2 µm over the metal layers, to etch vias for the final metal contact for high speed measurements. The PECVD oxide is prepared at 200°C using silane (SiH_4) and ammonia (NH_3) as precursor

gases. The vias are opened in the oxide layer using a thick photoresist mask. However it is noticed that the etching of the via through the oxide layer deposited over the gold layer is rather difficult. We followed a wet etching procedure using buffered hydrofluoric acid (BHF) (SiO_2 etch rate ~ 200 nm/min). Even with an increase in the etching time (4 times the usual time), we noticed that the oxide layer is not etched down completely. Subsequent final metallization through the vias resulted in no electrical contact with the first Au layer. Most of the characterization results mentioned in the following sections are based on the first small metal contacts over the PZT films. In this case, high speed characterization of the devices is not possible (contact needles separated by 100 µm), since the first metal layers are small and very close to each other. The microscope image of the waveguide sample after first and final metallization is provided in Figure 5.4.

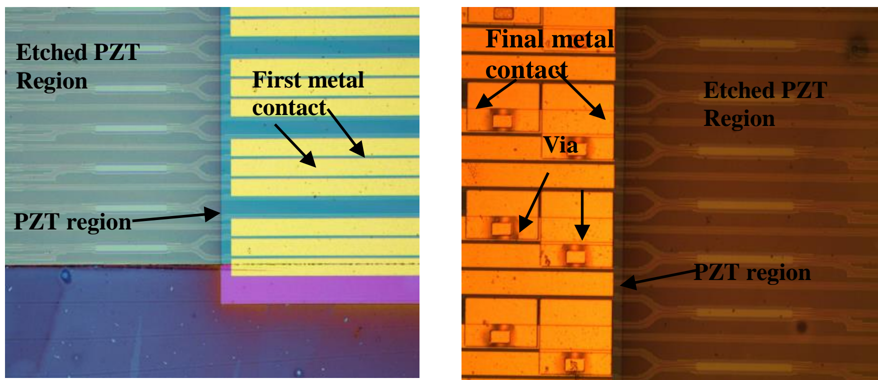

Figure 5.4: Microscope image of the Si_3N_4/PZT structure (a) with first layer metal pattern (b) after final metallization

5.2 Characterization of Si_3N_4/PZT electro-optic devices

The grating couplers are designed for TE guided propagation in the Si_3N_4 waveguides, with the center wavelength around 1310 nm. Figure 5.5 represents the waveguide loss measurement of the Si_3N_4/PZT structure, estimated by a cut back method, where spiral waveguides of different lengths are used. The top view of the Si_3N_4 waveguide with patterned PZT used for the loss measurements is shown in Figure 5.3(b). The PZT layers over the waveguides are patterned to remove it from the grating couplers. Leaving the PZT films over the grating structures would shift the grating

characteristics, thereby increasing the insertion loss. The MZ phase shifter structures are also patterned leaving the grating coupler and multimode interference coupler (MMI) without PZT, to avoid changing the splitting ratio of the MMIs. The loss measurements of the waveguides and the characteristics of the MZ phase shifters with and without PZT film are provided in Figure 5.5. The large insertion loss for the spirals originates from the large bend losses due to the fact that the PZT layer is not removed over the waveguide bends. The waveguide loss for the Si_3N_4/PZT heterostructure is extracted as 0.59 ±0.08 dB/cm at λ= 1310 nm.

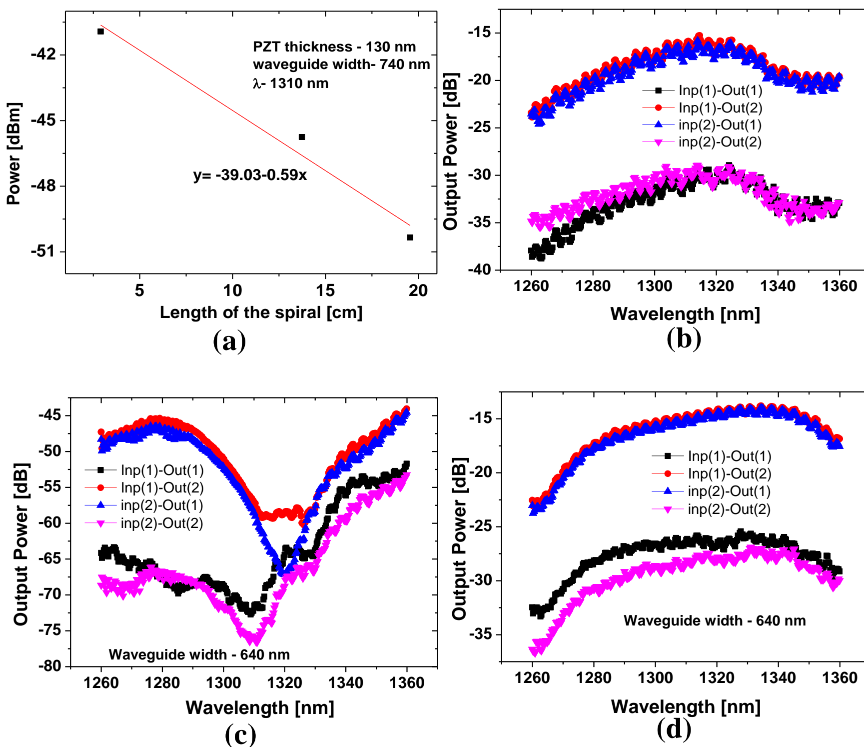

Figure 5.5: (a) Loss extraction using spiral waveguides. Charateristics of MZI phaseshifter for a waveguide width of 640 nm and PZT thickness of 130 nm (b) before PZT deposition (c) after PZT deposition without pattering (d) after PZT patterning

It is confirmed from the MZI measurements that the large insertion loss of the spiral waveguide originates from the large bend losses due to the unpatterned PZT over the waveguide bend (see Chapter 4). However, in the case of MZIs, the PZT layer is removed over the bends and remains only over the straight waveguides. It is evident from the measurements that when the PZT layers are not patterned, a large loss is introduced due to the shift in the grating coupler and MMI characteristics. However, as the layers are patterned, the measurements resembles that of MZIs without PZT. This indicates the very low loss introduced by the PZT layers and the proper patterning of the PZT above the grating couplers and MMIs.

5.2.1 Electro-optic characterization

The schematic of the measurement device and the measurement set-up are provided in Figure 5.6.

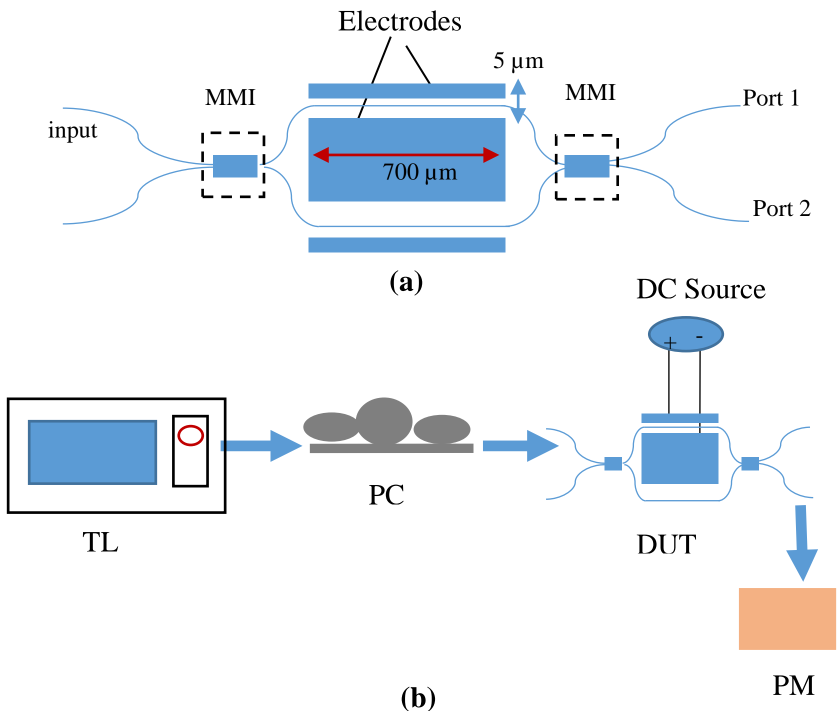

Figure 5.6: (a) Schematic of the MZI waveguide used for the electro-optic measurements. (b) Measurement set-up for electro-optic characterization. TL- Tunable laser, PC- Polarization controller, DUT- Device under test, PM- Power meter.

The measurement is carried out on a symmetric MZI waveguide of varying widths. The electrode separation and length are 5 µm and 700 µm, respectively.

An optical microscope image of the electrodes patterned on the Si_3N_4 waveguide is given in Figure 5.4(a). We use a tunable laser (wavelength range – 1260 to 1330 nm) as a light source. The grating couplers are specifically designed for a linear polarization (TE). We used polarization paddles to set the correct polarization before the light is coupled to the waveguides. A second fiber collect the output light and feds the to a power meter. When the voltage is applied to the electrodes, the pockels effect in the PZT films introduces a phase shift in one arm of the MZI. As the light from the two arms are combined it introduce an interference pattern. The V_π of the device is calculated from one maximum to the following minimum transmission intensity at any one of the output ports. . Unlike the measurements performed in section 3.5, where the electric field is applied orthogonally to the PZT film (the (100) crystallographic orientation), the co-planar electrodes result in electric field lines in the plane of the field and predominantly perpendicular to the preferential crystal orientation.

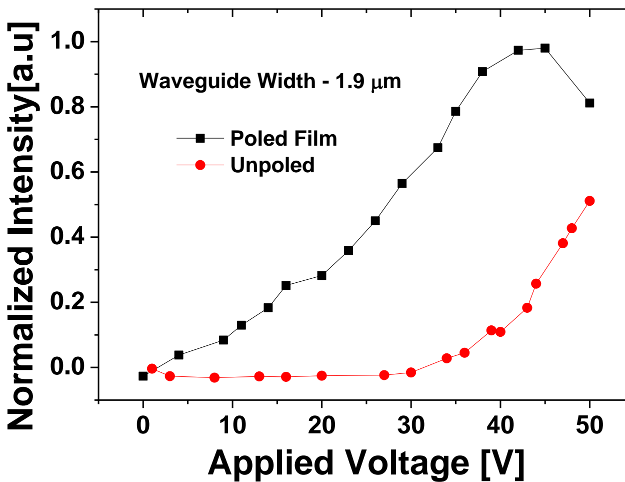

Figure 5.7: MZI characteristics of a Si_3N_4/PZT waveguide of width 1.9 µm, electrode seperation of 5 µm and electrode length of 700 µm, under poled and unpoled condition.

The films are poled to enhance the electro-optical properties prior to the measurements. The electric field poling of the PZT film is performed at 1.5 times the coercive electric field, as derived from the P-E hysteresis measurements (see section 3.3.2) and is considering the spacing between the electrodes.

With a coercive field of 70 kV/cm, it means that the poling is performed with an applied DC voltage of 50 V for an electrode separation of 5 µm. The MZI characteristics for a waveguide of width 1.94 µm and electrode separation 5 µm and electrode length 700 µm, is given in Figure 5.7. It is clear from the measurements that the poled PZT film exhibits a π phase shift, whereas the unpoled film shows a much slower variation. The $V_{\pi}L_{\pi}$ product of this device is calculated as 2.94 V.cm.

As the Si_3N_4 waveguide width decreases, the light confinement in the PZT film increases for a given PZT thickness. As expected, we observe a significant improvement in the electro-optic properties at smaller waveguide widths. Figure 5.8(a) and Figure 5.8(b) represent the electro-optic characterization of the MZI waveguides of widths 540 nm and 1540 nm respectively. For an MZI with a waveguide of width 540 nm and electrode length of 700 µm, a phase shift of 3π is observed for 50 V DC. Whereas for a waveguide width of 1.5 µm, the phase shift is reduced to 2π. The $V_{\pi}L_{\pi}$ product for these devices are estimated as 1.68 V.cm and 2.16 V.cm, for waveguides of width 540 nm and 1540 nm respectively. For the waveguide of 540 nm, the corresponding variation in the refractive index can be extracted as $0.39*10^{-4}$ (for 1 V).

Comparing with the simulations for an identical PZT thickness of 130 nm and top planarized oxide of thickness 50 nm and 100 nm, the $V_{\pi}L_{\pi}$ product for the waveguide width of 540 nm is calculated as 0.91 V.cm, 0.94 V.cm. Whereas for a waveguide width of 1540 nm, it is 1.37 V.cm and 1.54 V.cm, respectively. The modulation efficiencies obtained from the experiments are smaller compared to the simulation results. We believe that it is probably due to the difference in the thickness of the top planarized oxide and the PZT layers. An exact estimation of the top oxide thickness and PZT layer thickness is rather difficult with FIB measurement, due to charging of the layers. It is noticed from the simulations that even the smallest variations in this parameters significantly changes the modulation efficiency.

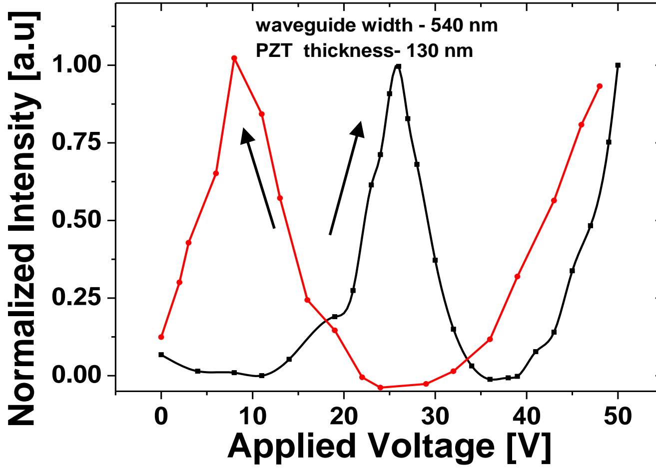

(a)

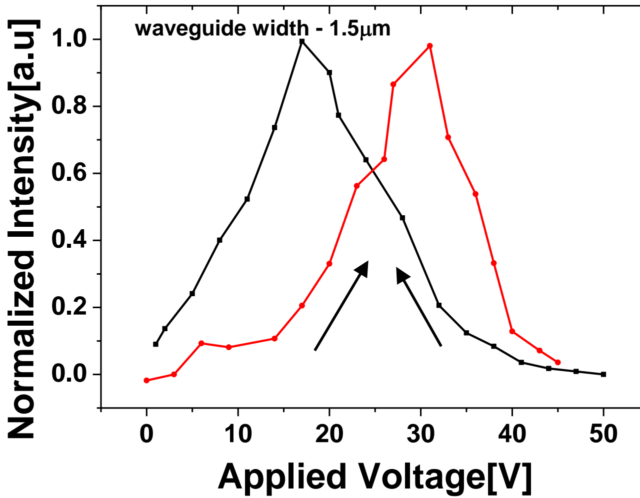

(b)

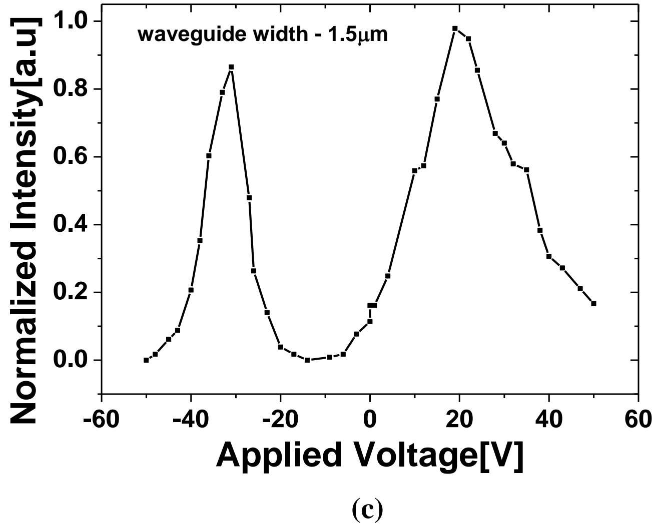

(c)

Figure 5.8: Electro-optic characterization of Si_3N_4/PZT MZI for an electrode length of 700 µm, electrode seperation of 5 µm and waveguide width of (a) 540 nm (b) 1.5 µm (c) 1.5 µm (from -50V to 50 V).

The best $V_\pi L_\pi$ product that is obtained here is one order of magnitude better than previously reported results on Si_3N_4 waveguides [9] and very similar to recently reported results on Si-BTO based slot waveguide [10]. In the latter case, the electro-optically active material consists of an epitaxially grown single crystal BTO thin film. This film possesses a very strong r_{51} tensor component of about 1200 pm/V- 1500 pm/V. However, the $V_\pi L_\pi$ product in our work is comparable to this result, as we can pattern the electrodes much closer to the waveguides, without any further increase in the waveguide loss. The advantage of integrating the BTO layer in the slot waveguide is that it does not need to be patterned, which eases the fabrication process. The amorphous Si layer deposited over the BTO layer is patterned with conventional Si RIE etching process. The propagation loss of the reported device is 44 dB/cm for an active $BaTiO_3$ layer of 80 nm, which is about two orders of magnitude higher than in our measurements with Si_3N_4 with PZT cladding (thickness of 130 nm).

If large voltages are applied, the curves exhibit a strong hysteresis effect. Practical devices should be designed with longer electrodes allowing for

lower driving voltages. Figure 5.8(c) shows electro-optic response of the MZI (waveguide width 1.5 µm) for both positive and negative half cycles.

Following these initial measurements the devices where covered with a SiO2 planarization layer for realizing more robust contacts. Unfortunately, as explained above, the required vias could not be etched in the SiO_2 layer and the devices could not be further characterised.

5.3 Conclusion

Electro-optic waveguide devices have been fabricated on the Si_3N_4 platform with PZT cladding layer, using conventional UV lithography. An etching process has been developed to efficiently pattern the PZT films in order to free the grating couplers. The fabricated devices are DC characterized to understand the electro-optic properties. The $V_\pi L_\pi$ product for these devices are estimated as 1.68 V.cm, 2.16 V.cm and 2.94 V.cm (after poling), for waveguides of width 540 nm, 1540 nm and 1940 nm respectively. The results are comparable to the best reported results for ferroelectric electro-optic devices. Currently the measurements are limited to DC voltages. The high speed characterization of the films requires further optimization of the fabrication process.

5.4 References

1. Cooney, T.G. and L.F. Francis, Processing of sol-gel derived PZT coatings on non-planar substrates. Journal of Micromechanics and Microengineering, 1996. 6: p. 291-300.
2. Zheng, K., J. Lu, and J. Chu, A novel wet etching process of Pb(Zr,Ti)O-3 thin films for applications in microelectromechanical system. Japanese Journal of Applied Physics Part 1-Regular Papers Short Notes & Review Papers, 2004. 43(6B): p. 3934-3937.
3. Liu, W., J. Ko, and W. Zhu, Device patterning of PZT/Pt/Ti/thin films on SiO2/Si3N4 membrane by a chemical wet etching approach. Journal of Materials Science Letters, 2000. 19(24): p. 2263-2265.
4. Wang, G.X., et al., Preparation and characterization of lead zirconate titanate thick films prepared by chemical solution deposition for MEMS applications. Ceramics International, 2015. 41: p. S250-S253.
5. Lee, Y.J., et al., A study of lead zirconate titanate etching characteristics using magnetized inductively coupled plasmas. Surface & Coatings Technology, 2000. 131(1-3): p. 257-260.
6. CheeWonChung, YoHanByun, and HyeInKim, Inductively Coupled Plasma Etching of Pb(ZrxTi1- x)O3 Thin Films in Cl2/C2F6/Ar and HBr/Ar Plasmas. The Korean Journal of Chemical Engineering, 2002. 19(3): p. 524-528.
7. Lin, Y.Y., et al., XPS analysis of Pb(Zr0.52Ti0.48) O-3 thin film after dry-etching by CHF3 plasma. Applied Surface Science, 2000. 165(1): p. 34-37.
8. Peng, S. and Y. Xi, Effect of microstructure on reactive ion etching of sol-gel-derived PZT thin film. Ceramics International, 2004. 30(7): p. 1215-1218.
9. Hosseini, N., et al., Stress-optic modulator in TriPleX platform using a ezoelectric lead zirconate titanate (PZT) thin film. Optics Express, 2015. 23(11): p. 14018-14026.
10. Xiong, C., et al., Active Silicon Integrated Nanophotonics: Ferroelectric BaTiO3 Devices. Nano Letters, 2014. 14: p. 1419-1425.

Chapter 6

Conclusions and outlook

The main conclusions and an overview of the main achievements of my work are listed in the following section. Next also some possible improvements are discussed and insight is given into possible future work.

6.1 Conclusions

In the first part of the work, a method to deposit ferroelectric thin films on Si and amorphous substrates is investigated for photonic applications. Experiments are conducted on both the existing as well as on new dielectric thin film materials as intermediate layers for the ferroelectric thin film deposition. The experiments performed on the existing intermediate layers such as ITO and $PbTiO_3$ produce randomly oriented ferroelectric films.

The electro-optic properties of the ferroelectric thin films strongly depend on the crystallographic orientation. Moreover, to use them for electro-optic applications, the thickness of the intermediate layer needs to be as small as possible and the intermediate layer material must be transparent at telecommunication wavelengths. In our work, a novel type of intermediate layer is demonstrated that allows depositing highly c-axis textured ferroelectric thin films on different platforms. The ultra-thin lanthanide-based layer with a thickness ranging from 5 to 15 nm is used as intermediate layer for the ferroelectric thin film growth. During the high temperature

annealing process to crystallize the ferroelectric thin films, the intermediate lanthanide layers are converted to their corresponding oxides, which are transparent from visible to the telecommunication wavelength.All the intermediate layers as well as ferroelectric thin films reported in this work are deposited following a chemical solution deposition procedure. A number of well-known ferroelectric thin films such as PZT, PLZT, BTO, BZT and $LiNbO_3$ are successfully deposited with preferential c-axis out-of-plane crystal orientation with our new deposition technique. A variety of structural characterization techniques such as XRD, X-ray pole figures, SEM, TEM and AFM are used to confirm the quality and properties of these thin films. The SEM and AFM measurements confirm we obtain smooth, well packed, crack free polygonal crystal grains. The EDX measurements confirm that the lanthanide based intermediate layer acts as an efficient diffusion barrier for Pb and it prevents any reactions at the interfaces at high annealing temperature, when used with sub-micrometer waveguide structures. The novel deposition method offers a low cost and simple method to produce good quality, strongly electro-optic PZT thin films on crystalline (Si) and amorphous (glass, glass+ITO, Al_2O_3, SiO_2 and Si_3N_4) substrates for a variety of integrated photonic and electronic applications.

The electrical properties of the PZT, BTO and BZT thin films are analysed with C-V, C-F, and I-V measurements to understand the quality of the films. The films exhibit very good dielectric properties, low dielectric loss and good dielectric breakdown strength. A large dielectric constant of ~ 600 for PZT thin films, 260 for BTO and 350 for BZT thin films (scaled by the buffer layer thickness, dielectric constant, and electrode parameters) is measured. The films show very low leakage currents in the order of 3.18 $\mu A/cm^2$ for an electric field of 150 kV/cm. The P-E hysteresis measurement gives a feedback on the good quality of the film (strong remnant polarization) and poling voltage (low coercive electric field). It is found that the films annealed at higher temperature exhibit superior properties owing to the better crystallinity and larger grain sizes.

The electro-optic properties of the PZT thin films are estimated with ellipsometry. The PZT films annealed at 630ºC and 560ºC on La, Pr and Nd buffer layers exhibit a high linear effective pockels coefficient of 240 pm/V, 215 pm/V, 200 pm/V and 115 pm/V, 96 pm/V, 89 pm/V, respectively, at a wavelength of 630 nm. The electro-optic measurements show a similar trend as expected from the electrical characterization, with a larger pockels coefficient for higher annealing temperatures. These results are comparable

to measurements of single crystalline PZT thin films, showing that our PZT film is an ideal candidate for realizing silicon nano-photonic EO modulators.

In the second part of the work, we propose a basic design for compact electro-optic modulators on the Si_3N_4 platform with ferroelectric thin films. Since the Si_3N_4 substrate is insulating, a contact scheme with embedded electrodes is rather difficult. So, the electrodes are designed in co-planar configuration, which eases the fabrication process. First, an optimal thickness for the PZT layer is calculated (100 to 150 nm) to use it as a cladding layer over the Si_3N_4 waveguide. Since the refractive index of PZT is larger than that of Si_3N_4 the PZT layer needs to be sufficiently thin in order to avoid light leakage. The thickness of the PZT layer is calculated to improve the light confinement in the PZT layer and to minimize the transition loss and bend loss Since the light absorption from the contact electrodes is one of the main loss mechanisms for waveguides with co-planar electrodes, the electrode spacing is optimized to reduce the mode absorption loss and to improve the $V_\pi L_\pi$ product. Simulations are performed to find an optimal trade-off between the modulation efficiency and the associated losses. With our design, modulators with $V_\pi L_\pi$ less than 1 V.cm are possible for devices with Si_3N_4 waveguides with a width of less than 1 µm, a Si_3N_4 thickness of 300 nm, a PZT thickness of 150 nm and an electrode spacing of 6 µm. The loss for these waveguides is less than 1dB/cm.

The devices are fabricated by lithography and RIE etching. An etching process based on SF_6 gas is developed to efficiently pattern the PZT films. The fabricated devices are DC characterized to understand the electro-optic properties. The $V_\pi L_\pi$ product for these devices is estimated as 1.16 V.cm, 1.75 V.cm and 3.5 V.cm, for waveguides with a width of 540 nm, 1540 nm and 1940 nm respectively. The results are comparable to the best reported results for ferroelectric thin film based electro-optic devices. Thus far our work is limited to DC-characterisation. The high speed characterization of the films requires further optimization of the fabrication process.

6.2 Outlook and future work

To reach the goal of a high speed integrated optical modulator, further improvements can be made on the materials, processing techniques, electrodes and possible new designs to use both TE and TM polarizations.

6.2.1 Improvement of the thin film processing

During this work it became obvious that crystallization of the PZT films under controlled oxygen ambient can improve the electro-optic coefficients, bringing them close to the bulk values. High temperature annealing introduces oxygen vacancies in the ferroelectric thin films. The O_2 vacancies formed result in the pinning of the domain walls and reduce the domain wall motion. The controlled oxygen partial pressure treatment (above the oxygen partial pressure at the ambient) has a tendency to reduce the oxygen vacancies inside the PZT film and counteract the excessive lead loss at high temperature annealing. This could bring better performance of the films at high frequencies as required by the modulator. We have demonstrated that the use of La-based intermediate layers can reduce the annealing temperature for the PZT deposition down to 530°C, albeit with reduced electrical properties. A combination of PZT growth on our intermediate layers with oxygen partial pressure crystallization method could potentially allow lower annealing temperature, without compromising on the electrical and electro-optical properties.

The issues associated with the Pb loss of the PZT films can also be overcome by performing rapid thermal annealing (RTA). For applications that require films of thicknesses in the order of a few micrometers RTA annealing is preferred. The layer by layer annealing procedure in a tube furnace is time consuming for thicker substrates and the annealing of PZT for such an extended period of time results in excessive lead loss.

6.2.2 Improvement of modulators using other materials and/or electrode configurations

In this work only electro-optic devices based on PZT-films were demonstrated. $BaTiO_3$ thin films can also be used. In other publications that demonstrate electro-optic waveguide modulators mostly BTO is used as it is an ideal option for electro-optic devices. The r_{51} tensor component for BTO thin films is larger than for PZT thin films. For electro-optic devices based on the co-planar electrode configuration, the effective pockels coefficient strongly depends on the r_{51} tensor component. PLZT films are also an interesting candidate for electro-optic applications. Compared to the PZT(52/48) composition used in our work, La-doped PZT films (PLZT(8/52/48)) show a lower coercive electric field (E_c< 40 kV/cm) which eases the switching of the spontaneous polarization direction. This can

significantly reduce the electric field (and voltage) required for poling. Moreover, the PLZT films exhibit electro-optic effects comparable to the PZT films (see Table 1.2). Initial experiments performed on Si_3N_4 waveguides are based on electrodes designed as lumped elements. However, for high frequency operation, travelling wave electrodes need to be designed to ensure a low driving voltage together with high bandwidth operation.

6.2.3 Modulators using TM polarized light

An embedded electrode system could be an ideal configuration for waveguide modes with TM polarization, where the applied voltage is along the c-axis direction. Since our films possess a strong c-axis out-of-plane texturing, the electric field applied along the c-axis could bring a strong variation in the refractive index through the high r_{33} tensor component. Since Si_3N_4 is an insulating substrate, realizing an efficient TM modulator with embedded configuration is not straightforward. However, such a structure is possible by using Si as a waveguide medium and a highly doped Si can be used as a bottom contact for an embedded electrode configuration.

6.2.4 Modulators on Si platform

The modulators can be fabricated on the Si platform using ferroelectric thin films as cladding. Both TE and TM modulators are possible with our c-axis oriented ferroelectric thin films. Efficient TE modulators are possible with co-planar electrode configuration and TM modulators with embedded electrode configuration. Modulation efficiency of the electro-optic modulators can be improved by increasing the electro-optic overlap integral. One of the techniques to improve the mode overlap is to use a Si-slot waveguide structure. However, deposition of ferroelectric thin films on a horizontal slot structure is difficult as discussed in chapter 2, due to the conformity associated with the spin-coated layers. A vertical slot structure is possible by using a Si/PZT/amorphous Si sandwich layer as explained in Figure 1.6.

6.2.5 Waveguide tuning based on the piezoelectric effect

In this thesis, we solely focussed on the electro-optic effects from the ferroelectric thin films. The piezoelectric properties can also be used for tuning the waveguides. The waveguide devices reported before based on the piezoelectric tuning were not so efficient due to large separation of the lossy

PZT capacitors (Pt/PZT/Pt) from the waveguide core. This is to avoid the absorption loss from the Pt electrodes. The Pt film serves as an intermediate layer for PZT growth as well as a bottom electrode (see section 1.6.1). This reduces the effective strain transfer to the waveguide introduced by the piezoelectric effect. With our new deposition procedure, the PZT films can be directly deposited over the Si waveguide, where Si can be used as a bottom electrode. With this configuration, the strain generated by the piezoelectric effect can be more efficiently transferred to the Si waveguide. Even though the electro-optic effects give a larger change in the refractive index (with the same electrode configuration) compared to the piezoelectric effect, this configuration can be very effectively used for acousto-optic devices.

6.2.6 Optical nonlinearities

Ferroelectric thin films exhibits strong second order nonlinear optical properties. Initial experiments performed with PZT film on a glass substrate show second harmonic generation. Currently, we are trying to quantitatively to estimate the second order nonlinear electro-optic coefficient.

Appendix A

Simulation of Si-PZT electro-optic devices

Simulation of Si/PZT based electro-optic devices

The simulations are performed assuming a single crystalline PZT/BTO thin film, deposited as a cladding layer over a planarized Si waveguide (see section 5.1.1). Different modulator configurations can be designed considering the direction of the crystal/optical axis of the ferroelectric thin film and the electrode configuration.

Considering a tetragonal 4mm crystal structure (see section 4.2), we assume the tensor elements r_{51}, r_{33} and r_{13} as 500 pm/V, 100 pm/V, 30 pm/V, respectively. The results of the simulation based on embedded and co-planar electrode configuration are explained in the following sections.

A1: Embedded electrode configuration

The Si waveguide with an embedded electrode configuration is given in Figure 1. The Si ridge waveguide of width 450 nm, thickness 220 nm, and slab height 60 nm is considered for this simulation. The BTO/PZT film is

thick enough to prevent any abortion of the propagating mode. With this configuration, the strong electro-optic effects observed in our measurements in section 3.5 can be explored. The results of the c-axis and a-axis oriented films for both TE and TM propagating modes are given in Table A1.

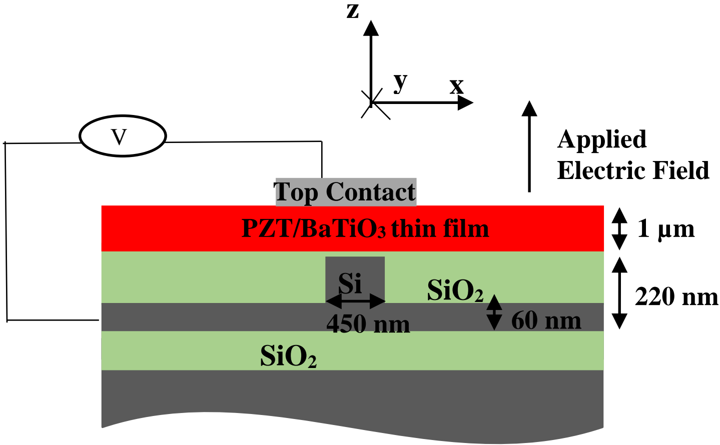

Figure A1: Si/PZT modulator with an embedded electrode configuration

Table A1: Simulation results for Si/PZT structure with embedded electrode configuration

	a-axis oriented		**c-axis oriented**	
	TE	**TM**	**TE**	**TM**
Confinement factor(%)	19.8	65.6	17.2	69.9
$\mathbf{n_{eff}}$	2.51	2.27	2.51	2.27
$\mathbf{\Delta n}$	$2.3*10^{-4}$	$1.43*10^{-3}$	$2.5*10^{-4}$	$3.4*10^{-4}$
$\mathbf{V_{\pi}L_{\pi}}$**(V.cm)**	0.18	0.059	0.31	0.22

It is clear from Table A1 a-axis oriented films show much stronger electro-optic effects compared to the c-axis oriented films. This is due to the stronger influence of r_{51} component have in a-axis oriented films (r_{33} influence c-axis oriented films).

A2: Co-planar electrode configuration

The Si/PZT modulator structure with a co-planar electrode configuration is shown in Figure A2. For the simulations we assumed an electrode separation of 4 µm, and PZT thickness of 250 nm. As the electrodes are separated away from the Si waveguide, the PZT thickness can be reduced to 250 nm for this configuration, without any increase in the electrode absorption loss.

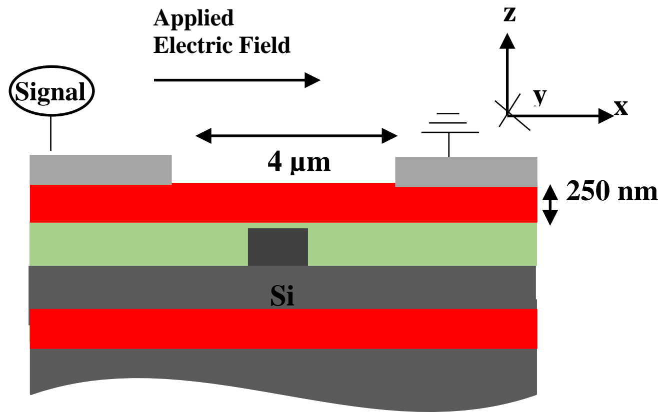

Figure A2: Si/PZT modulator with a co-planar electrode configuration

The detailed characterization results of Si/PZT structure with the co-planar electrode configuration is given in Table A2.

Table A1: Simulation results for Si/PZT structure with embedded electrode configuration

	a-axis oriented		**c-axis oriented**	
	TE	**TM**	**TE**	**TM**
Confinement factor(%)	19.6	36.4	19.6	36.4
$\mathbf{n_{eff}}$	2.429	2.13	2.429	2.137
Δn	$1*10^{-4}$	$2*10^{-4}$	$2*10^{-5}$	$2*10^{-5}$
$\mathbf{V_\pi L_\pi}$**(V.cm)**	0.77	0.387	3.87	3.87